博士論文

Synthesis, Purification and Device Application of Horizontally Aligned Single-Walled Carbon Nanotubes

（水平配向単層カーボンナノチューブの合成・精製・デバイス応用）

大塚慶吾

Doctoral Dissertation

Synthesis, Purification and Device Application of Horizontally Aligned Single-Walled Carbon Nanotubes

by

Keigo Otsuka

Presented to
GRADUATE SCHOOL OF ENGINEERING, THE UNIVERSITY OF TOKYO
in Partial Fulfillment of the Requirements for the Degree of

Doctoral of Philosophy

in the Field of Mechanical Engineering

March 2018

Abstract

After more than a half century of scaling down of silicon transistors, bulk-silicon field-effect transistors will not work reliably at ultrascaled gate lengths. One possible way to continue the scaling is to change the channel geometry and/or materials for better electrostatic control. Among a number of candidates, the extraordinary electrical properties and ultrathin bodies of semiconducting single-walled carbon nanotubes (s-SWNTs) make them attractive for use in logic transistors. A horizontal array configuration has been achieved to realize optimal use of their excellent properties. However, coexistence of metallic (m-) SWNTs from conventional growth processes causes excessive leakage in the off-state transistors. One promising mean to obtain high-purity s-SWNT arrays is direct synthesis of single-crystal substrates, which could provide high-density SWNT arrays over a large area. Chirality-controlled growth has not realized required purities of s-SWNTs (>99.9999%); therefore, on-chip purification need to performed, while s-SWNTs and the original morphology are maintained.

In this thesis, the preparation of purely s-SWNT arrays will be described mainly from two points of view; growth and purification (sorting). These aspects are developed in harmony with each other to pursue three kinds of scaling at once; namely scaling to (1) short-channel, (2) small inter-nanotube separation, and (3) large-scale integrated circuits. By proposing a digital isotope coding method for tracing the time-resolved growth profiles of a variety of individual SWNTs, the growth mechanism of SWNTs are re-investigated. The isotope labeling technique offers opportunities to analyze numerous SWNTs from one growth cycle without a need for extreme growth condition (*e.g.* ultralow pressure). Focuses is directed not only to the selectivity in chirality, but also to the nucleation and termination of SWNT growth to obtain clues to the improvement of density and its spatial uniformity.

In addition, a sorting technique of s-SWNTs is developed as a postgrowth treatment on SWNT arrays. Joule self-heating is employed as source of selective removal of m-SWNTs because of a considerable difference in electrical conductance of two types of SWNTs under gate control. The self-heating in m-SWNTs leads to their full-length burning with the assistance of polymer coating, water vapor and

electric field, leaving arrays of long s-SWNTs for a scaled-up purification. Lateral confinement of the burning within the quasi-1D bodies (~nm) suppresses the damage to neighboring s-SWNTs even in densely packed arrays.

Finally, multiple transistors with various dimensions are fabricated along the s-SWNTs as a demonstration toward high-performance integrated circuits of SWNT-based transistors. The fabrication method that utilizes the full-length burning of m-SWNTs also enables ultrashort channel lengths, as well as the other two kinds of device scaling. Further improvement of controlled growth of SWNTs, post-growth treatments, and their combination would lead to the effective use of SWNTs in logic, high-speed communication and next-generation devices.

Acknowledgement

During the course of this thesis, I have been privileged to receive a lot of advice, assistance and encouragement. I would like to thank them all, but I am afraid a space for that is not enough here. I would first like to thank my supervisor, Prof. Shigeo Maruyama for his continued advice and invaluable guidance since 2012, when I was an undergraduate student. I would like to also thank Profs. Shohei Chiashi and Taiki Inoue for their uncountable helps and discussion throughout all the six years. I would like to thank Prof. Rong Xiang for fruitful discussions on the synthesis and characterization of carbon nanotubes. Thanks also go out to Prof. Jie Liu for many advice and supports during half a year at Duke University.

I would like to thank the members in my PhD defense committee for their time and insightful discussion: Prof. Hirofumi Daiguji, Prof. Junichiro Shiomi, Prof. Kosuke Nagashio, Prof. Shohei Chiashi, Prof. Yuichiro K. Kato, as well as Prof. Shigeo Maruyama. Their comments and suggestions are indispensable to finish this thesis.

My graduate studies were made possible by generous financial support from the Japanese Society of Science Promotion (JSPS) through a Young Researcher Fellowship (DC1). Again, I am very grateful to Dr. T. Inoue, who mentored me, taught me many things about being a researcher, and supported and encouraged my researches. Last but not least I would like to thank my research collaborators whom I have learned much from, Prof. Reo Kometani, Dr. Etsuo Maeda, Dr. Takuma Hori, Dr. Takafumi Oyake, Asuka Miura, Daisuke Hasegawa, Dr. Jinghua Li, Xiao Zhang, Yuki Shimomura, Gergely Németh, Shun Yamamoto, Seungju Seo, and staffs in the lab, Mr. Makoto Watanabe and Ms. Maiko Terao. Finally, life in Tokyo would have been tougher for a person from the country without my many friends. This thesis dedicated to my family, and the memory of my grandfather.

Table of Contents

Chapter 1: Introduction 1

1.1 Introduction and overview of the thesis 1

1.2 Structural representation of SWNTs 2
1.2.1 Electronic structure of SWNTs 4

1.3 Material synthesis and characterization 6
1.3.1 Main synthetic approaches of SWNTs 6
1.3.2 Raman scattering spectroscopy 8
1.3.3 Electron microscopy 9

1.4 Applications of carbon nanotubes 10

1.5 Basic sample preparation and measurement 11
1.5.1 Transfer of SWNT arrays onto arbitrary substrates 11
1.5.2 Formation of metal contacts (makers) and etching 12
1.5.3 Electrical measurement/treatment in controlled atmosphere 12

1.6 Challenges for SWNT-based computing 13

1.7 Objective of the thesis 14

Structure of the thesis 15

Chapter 2: Synthesis and Analysis of Horizontal SWNT Arrays 17

2.1 Introduction to synthesis of SWNT arrays 17

2.2 Basic analysis on horizontally aligned SWNTs 18
2.2.1 CVD time-dependent length of aligned SWNTs 18
2.2.2 Chirality (n,m) assignment of SWNTs by Raman spectroscopy 20

2.3 Digitally coded isotope labeling for monitoring SWNT growth 25
2.3.1 Tracing the growth histories of horizontally aligned SWNTs 25
2.3.2 Growth histories of individual SWNTs 29
2.3.3 Analysis on spontaneously formed intramolecular junctions 36
2.3.4 Response to ethanol pressure change during CVD 38
2.3.5 Temperature-dependent growth along an individual SWNTs 41

2.4 Direct growth of aligned SWNTs on TEM grids 44
2.4.1 Aligned growth on NaCl-induced cristobalite substrates 44
2.4.2 In-plane TEM grids from Si with cristobalite layer 47

Chapter 3: Upscalable on-Chip Sorting of s-SWNT Arrays 49

3.1 Introduction to SWNT sorting 49
3.1.1 Liquid-phase separation methods of s-SWNTs 49
3.1.2 Growth-phase sorting methods of s-SWNTs 50
3.1.3 On-substrate purification methods 50

3.2 Long-length burning of m-SWNTs on substrates 52
3.2.1 Self-sustained burning of m-SWNTs 52
3.2.2 One-way burning from random breaking points 55

3.2.3 Evaluation of purified SWNT arrays from device performance 56
3.2.4 Discussion on the roles of water and polymer in the burning process 58
3.2.5 One-way burning from random breaking points 61
3.2.6 Simulation study on burning SWNTs 61

3.3 Secrets behind the one-way burning 66
3.3.1 Remote etching during electrical breakdown 66
3.3.2 Size determination of nanogaps produced by electrical breakdown 69
3.3.3 Effects of ambient water on the remote etching 70
3.3.4 Field emission at SWNT nanogaps 70
3.3.5 Threshold field for gap extension: gap size *versus* voltage 73
3.3.6 Remote etching among adjacent SWNTs 76
3.3.7 One-way burning from pre-formed nanogaps 78

Chapter 4: Scalable Fabrication of SWNT Transistors **81**

4.1 Three types of scaling of SWNT transistors 81
4.1.1 Ultrascaled channels and contacts 81
4.1.2 Densely packed SWNT channels 82
4.1.3 Large-scale integration of SWNT transistors 84

4.2 Purely semiconducting SWNT arrays via full-length burning 84
4.2.1 Site-controlled formation of nanogaps 84
4.2.2 One-way burning site-controlled nanogaps 86

4.3 Multiple transistors along identical array of s-SWNTs 87
4.3.1 Fabrication and characterization of multiple transistors 87
4.3.2 Potential for channel scaling 88
4.3.3 Thermal properties during electrical breakdown of short SWNTs 91
4.3.4 Suppressed damage to s-SWNTs 92
4.3.5 Applicable to high-density arrays? 94
4.3.6 On-state conductance per tube 98

Chapter 5: Conclusions **101**

5.1 Conclusions 101

5.2 Prospects 102

Bibliography **104**

Appendix **117**

List of publications **121**

International Conferences **122**

List of Abbreviations **123**

Chapter 1:

Introduction

1.1 Introduction and overview of the thesis

Single-walled carbon nanotubes are a new group of material with quasi one-dimensional (1D) structure of rolled-up graphene sheets, experimentally found in 1993.[1] In addition, owing to the unique properties of sp^2 nanocarbon and the 1D structure, there are a lot of possible applications of SWNTs in electronics, mechanics, and chemical engineering. Field-effect transistors (FET) are a one of the most promising field of this unique material because it has suitable transport properties for both electron and holes, and an extremely thin nanowire-like structure for the best gate control. In recent years, significant progresses on SWNT transistors are reported; 5-nm gate length,[2] 40-nm footprint (including gate and metal contacts),[3] both of which exceed Si transistors in terms of size and performance. On the other side of device scaling, more than one million SWNT-based inverters are implemented into three-dimensional complex nanotechnology-based systems, demonstrating large-scale compatibility of this material.[4] However, the difficulty of preparing uniform and purely semiconducting SWNT arrays over a large area has hindered simultaneous achievement of the ultrascaled devices and their integration in large-scale systems.

In the thesis, such s-SWNT arrays will be studied from the viewpoints of synthesis and analysis, post-growth purification, and device fabrication. For practical applications of SWNTs, perfect control of chirality would not always result in the best performance of devices, unless other properties, such as alignment and density, are controlled at the same time. In addition, the compatibility of synthetic processes and post-sorting processes has to be optimized to produce the SWNTs that are really required for applications. Based on a consistent strategy for preparing large-area, high-density, and purely semiconducting SWNT arrays, the thesis will deal with synthesis and characterization of aligned SWNTs, sorting of semiconducting SWNTs, and the fabrication of SWNT-based transistors.

1.2 Structural representation of SWNTs

SWNTs have a structure of a rolled-up graphene sheet. Since this geometry of the graphene sheet determines the electronic structure of SWNTs, it is important to understand the geometric of graphene at the beginning. Figure 1.1 shows a schematic of an SWNT opened-up into a graphene sheet. Structure of the sp^2 carbon network of a two-dimensional graphene sheet is presented as a hexagonal lattice in Figure 1.1.

Unit vectors of two dimensional graphene in real space $\mathbf{a}_1$, $\mathbf{a}_2$ are shown in Figure 1.1. The real space unit vectors $\mathbf{a}_1$, $\mathbf{a}_2$ are expressed as below.

$$\mathbf{a}_1 = (a, 0) \qquad (1.1)$$
$$\mathbf{a}_2 = \left(\frac{1}{2}a, -\frac{\sqrt{3}}{2}a\right)$$

where $a = |\mathbf{a}_1| = |\mathbf{a}_2| = 2.46$ Å is the lattice constant of graphene. A specific vector that connects the O atom and the A atom in Figure 1.1 is called the chiral vector $\mathbf{C}_h$, surrounding the tubular plane perpendicular to the tube axis. The structure of SWNTs is uniquely defined by this single vector, which is expressed using the unit vectors $\mathbf{a}_1$, $\mathbf{a}_2$ as below.

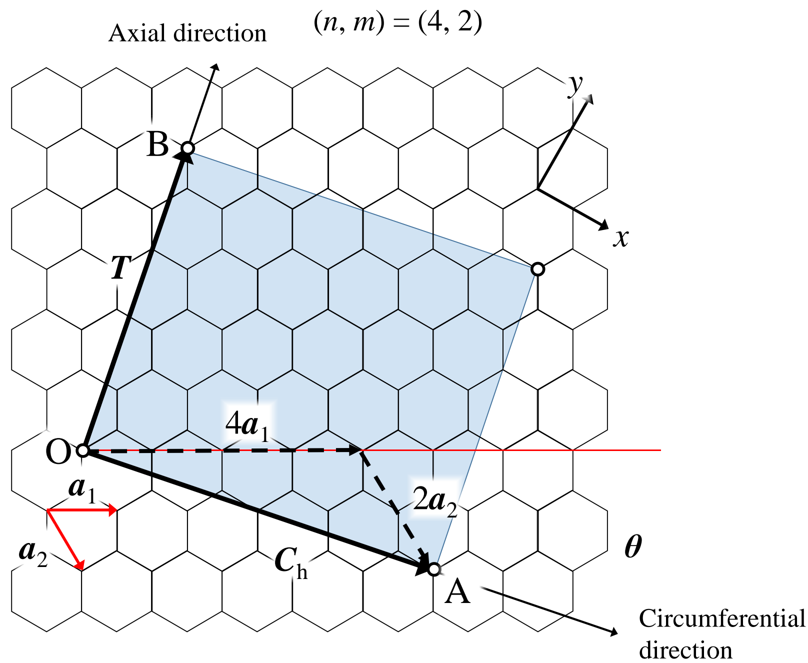

Figure 1.1 Unrolled hexagonal lattice of a SWNT. The chiral vector $\mathbf{C}_h$ and translational vector T are presented for the case of $\mathbf{C}_h = 4\mathbf{a}_1 + 2\mathbf{a}_2$ SWNT. Its unit cell is denoted as shadowed area. The angle between a_1 and $\mathbf{C}_h$ gives the chiral angle θ ($0 \leq \theta \leq 30°$).

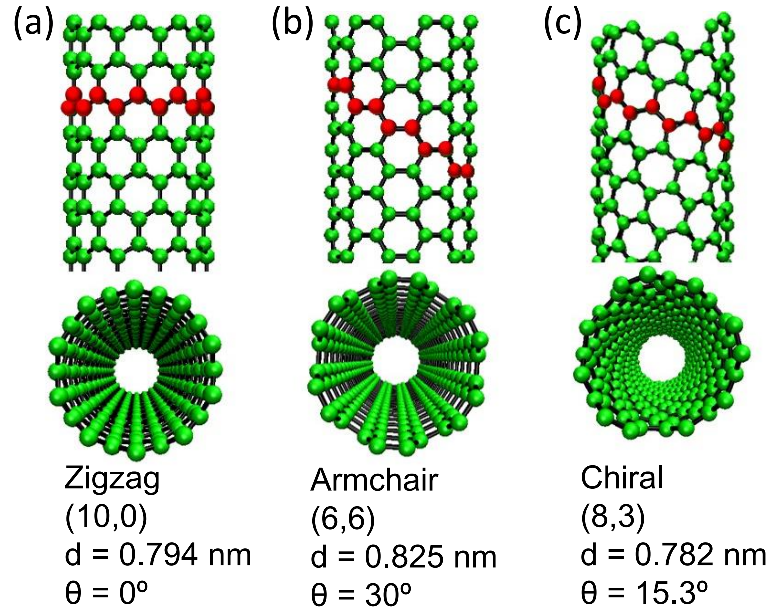

Figure 1.2 Structures of (a) zig-zag type, (b) armchair type, and (c) chiral type SWNTs.

$$\mathbf{C}_\mathrm{h} = n\mathbf{a}_1 + m\mathbf{a}_2 \equiv (n, m) \tag{1.2}$$

where *n*,*m* are integers and called chiral indices. Figure 1.1 shows an example for the chiral indices of (4,2) SWNTs.

$$\mathbf{T} = \frac{(2m+n)\mathbf{a}_1 - (2n+m)\mathbf{a}_2}{d_R} \tag{1.3}$$

$$d_t = \frac{a\sqrt{n^2+nm+m^2}}{\pi} \tag{1.4}$$

$$\theta = \cos^{-1}\left(\frac{2n+m}{2\sqrt{n^2+nm+m^2}}\right) \quad \left(|\theta| \le \frac{\pi}{6}\right) \tag{1.5}$$

$$d_R = \begin{cases} d : \text{if}\,\mathrm{mod}(n-m,3) = 1 \text{ or } 2 \\ 3d : \text{if}\,\mathrm{mod}(n-m,3) = 0 \end{cases} \tag{1.6}$$

SWNTs can be categorized into three groups according to their chiral indices (*n*,*m*). Armchair type has a chiral index of (*n*,*n*) and chiral angle of 30°. Zigzag type has a chiral index of (*n*,0) and chiral angle of 0°. These two types are also called achiral type. The other chiral indices are categorized into chiral type. Figure 1.2 shows schematic structures of typical SWNTs of each type.

1.2.1 Electronic structure of SWNTs

Electronic structure of SWNTs is explained as that of the graphene modulated in the circumferential direction according to how the graphene is rolled-up into a tubular shape. Therefore, starting from the electronic structure of normal graphene, SWNTs are described by imposing a periodic boundary condition. The energy dispersion relation of graphene $E^{\pm}_{\text{graphene}}$ is expressed by the equation below.

$$E^{\pm}_{graphene}(\boldsymbol{k}) = \frac{\varepsilon_{2p} \pm \gamma_0 \omega(\boldsymbol{k})}{1 \mp s\omega(\boldsymbol{k})}. \quad (1.7)$$

where $\omega(k)$ is written as below.

$$\omega(\boldsymbol{k}) = \sqrt{|f(\boldsymbol{k})|^2} = \sqrt{\left|\exp(ik_x a/\sqrt{3} + 2\exp(-k_x a/2\sqrt{3})\cos(k_y a/2)\right|^2}. \quad (1.8)$$

Note that symbols + and – represent antibonding and bonding orbitals. Figure 1.3 shows the energy dispersion relations of graphene.

These relations can be applied to the geometry of an SWNT by the zone-folding method. In SWNTs, only the limited wave vector in the energy dispersion relations of graphene is allowed due to the circumferential periodic boundary conditions. The allowed wave vectors all depend on the chirality of SWNTs, which determines the electronic structure. In Figure 1.3, the Brillouin zone of graphene and a (6,3) SWNT (cutting line) are overlapped in a reciprocal space.

As shown in Figure 1.4, electrons in SWNTs can have wave vectors along N cutting

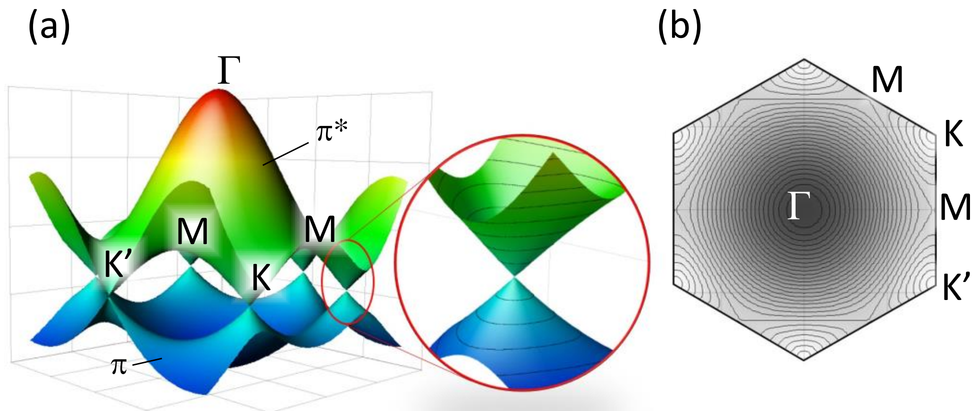

Figure 1.3 The energy dispersion relations for graphene plotted as (a) a 3D diagram and (b) a contour plot (only π^* band).

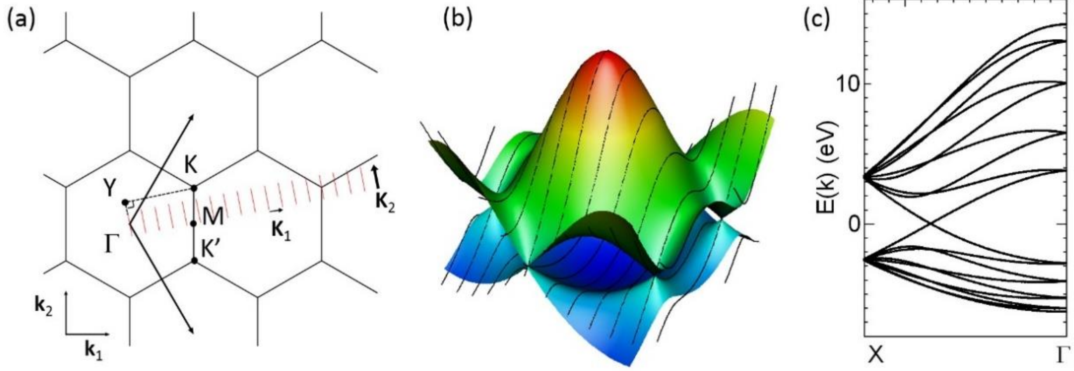

Figure 1.4 (a) Schematic of the expanded Brillouin zone of a (6,3) SWNT with cutting lines. (b) The energy dispersion relation of graphene and a (6,3) SWNT. (c) One-dimensional energy dispersion relation for a (6,3) SWNT.

lines expressed as below using two vectors $\mathbf{K}_1$ and $\mathbf{K}_2$.

$$k\frac{\mathbf{K}_2}{|\mathbf{K}_2|} + \mu\mathbf{K}_1, \text{ note that, } -\frac{\pi}{T} < k < \frac{\pi}{T}, \quad \mu = 0, \dots, N-1 \tag{1.9}$$

$$\mathbf{K}_1 = [(2n+m)\mathbf{b}_1 + (2m+n)\mathbf{b}_2]/Nd_R \tag{1.10}$$

$$\mathbf{K}_2 = (m\mathbf{b}_1 - m\mathbf{b}_2)/N$$

Note that $\mathbf{b}_1$ and $\mathbf{b}_2$ are reciprocal lattice vectors that are written as below.

$$\mathbf{b}_1 = \left(\frac{1}{\sqrt{3}}, 1\right)\frac{2\pi}{a}, \mathbf{b}_2 = \left(\frac{1}{\sqrt{3}}, -1\right)\frac{2\pi}{a} \tag{1.11}$$

$\mathbf{K}_1$ and $\mathbf{K}_2$ correspond to circumferential and axial directions of SWNTs, so only $\mathbf{K}_2$ discretizes due to the periodic boundary condition. As shown in Figure 1.4(b), only wave vectors and energies along cutting lines (black lines in the figure) on the energy dispersion relations for graphene are allowed. This can be further projected on YZ plane, giving one-dimensional energy dispersion relations as shown in Figure 1.4(c). Since the cutting lines for (6,3) SWNTs cross the K point, where the density of states of graphene is nonzero at the Fermi level, (6,3) SWNTs are categorized into “metallic” SWNTs (or zero-gap semiconductor). In general, SWNTs whose mod(*n*-−*m*,3) = 0 are metallic, while the other are semiconducting. Semiconducting (s-) SWNTs can be further divided into type I (mod(*n*−*m*,3) = 1) and type II semiconductors (mod(*n*-−*m*,3) = 2). The difference of these two types are often found in optical behaviors.

1.3 Material synthesis and characterization

1.3.1 Main synthetic approaches of SWNTs

Synthesis of CNTs can be divided into three methods; arc discharge,[5,6] laser vaporization,[7] and chemical vapor deposition (CVD) methods. Multi-walled CNTs (MWNTs) were first found by the arc discharge method, where high-voltage is applied between carbon rods.[5] Later, SWNTs were obtained by adding metals in the carbon rods,[1] and the crystallinity of the SWNTs is high because the SWNTs are grown at very high temperature. Although the productivity is not high in comparison with the CVD method mentioned later, SWNTs by this method are commercially available. The laser vaporization method produces SWNTs by the introduction of strong laser to metal-mixed carbon rods in high-temperature furnace. This method also offers poor scalability and thus low productivity compared to the CVD method.

Third method, but most commonly used today, is the CVD method, whereby CNTs grow from catalyst nanoparticles (often metals) with the introduction of carbon feedstock gases in high-temperature furnaces as shown in Figure 1.5. In a general CVD process, carbon precursors are first dissociated and adsorbed on the catalyst nanoparticles. Carbon atoms are then dissolved and diffused in/on the catalysts. After some time of incubation, carbon atoms precipitate and form caps (nucleation), followed by continuous growth of tube walls. This method is widely studied and

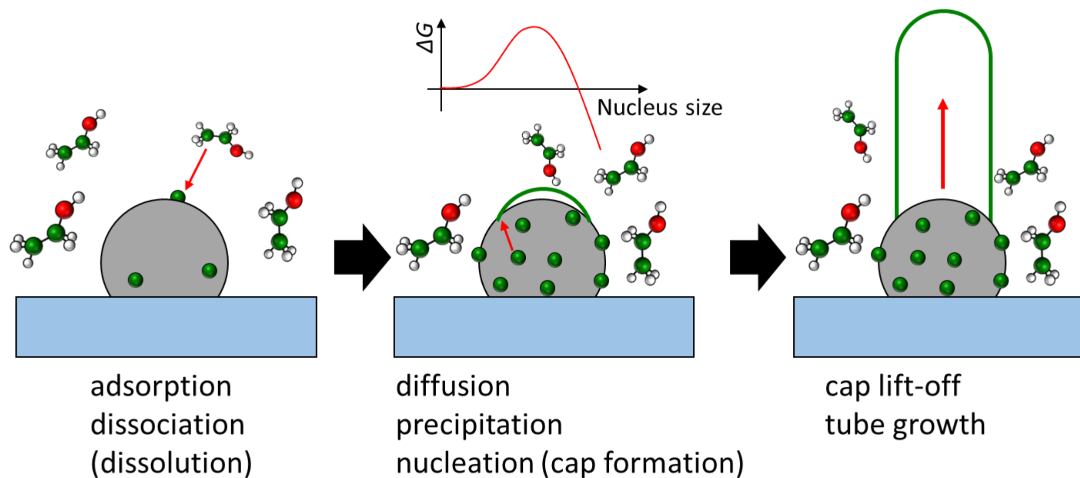

Figure 1.5 Schematics to explain the growth process of SWNTs in alcoholic catalytic CVD. Gray and green circles represent a catalyst nanoparticle and carbon atoms, respectively.

utilized for any kinds of application owing to the large productivity and structure-controllability of CNTs.

The CVD method produces various morphologies of CNTs, from powder-like bulk form, forest-like vertically aligned structures, randomly oriented network thin films, and to horizontally aligned individual (not bundled) configuration, depending on temperature, carbon feedstock gases, substrates, supports, and density of catalysts, and so on. Each type of the CNT morphologies is suitable for different kinds of applications. Therefore, the morphology, as well as tube chirality (n,m), has to be controlled according to the applications.

When a single or very sparse SWNTs grow on substrates, such as SiO_2/Si, the SWNTs have no preference in orientation and usually are winding due to the flexible body derived from the thin tubular structure. As the density of SWNTs increases, the SWNTs get electrically connected each other and form random networks. This morphology could be directly used for channels of thin-film transistors and transparent conductive films depending on density, length, and ratio of m- and s-SWNTs. On the other hand, when SWNTs are efficiently grown from high-density catalysts supported on substrates, the SWNTs are vertically aligned perpendicular to the substrates.[8] Since the length of vertically aligned SWNTs is not limited by the substrate area, millimeter-tall forests of SWNTs were obtained. Therefore, this kind of growth methods are suitable for mass production, if not the best, especially where the aligned morphology is required.

When moderately sparse SWNTs are grown on special substrates with a certain plane of crystals, the orientation of SWNTs follows certain directions of the lattice.[9,10] This yields horizontally aligned SWNTs. Growth of horizontally aligned SWNTs were realized with the guidance of atomic steps on the surface of mi-cut crystalline substrates.[11] The morphology of horizontal arrays can be used in semiconductor applications of SWNTs, such as transistors, because such applications do not require large amounts of SWNTs but high-quality and well-organized materials.

1.3.2 Raman scattering spectroscopy

Characterization techniques of nanomaterials, such as SWNTs, are usually much different from bulk materials. Since uniqueness of SWNTs lies not only in their geometric structures but also in the difference in electronic structures originated from the geometry, conventional optical imaging and scanning probe microscopy cannot fully chapter the characteristics of SWNTs. Both electrons and phonons in SWNTs behave much differently depending on atomic arrangements (*i.e.* chirality); therefore, Raman spectroscopy, which probes the behaviors of electrons and phonons in materials, can be a powerful tool for the probing physical properties of SWNTs.

When photons are scattered from a material, most photons have the exact same energy as the incident photons. A part of photons increase or decrease the energy by interacting with vibrations and rotations of materials (phonons in the case of crystalline materials like carbon nanotubes). This scattering is particular to each material and thus can be used for identification of many kinds of materials.

In SWNTs, significantly large resonant effects are observed due to the van Hove singularities in electronic density of states.[12] When the photon energy of incident light matches the optical transition energy of SWNTs, this resonance occurs and therefore Raman scattering from even a single SWNT (~1 nm in diameter) can be well detectable. SWNTs have several Raman-active phonon modes unique to each chiral indices (n,m). G-mode of SWNTs, which appears around 1590 cm^{-1}, is a fingerprint for sp^2 carbon materials, such as graphite, graphene, and carbon nanotubes, originating from an in-plane mode of hexagonal rings of graphite. This G-mode is split into two prominent peaks (G^+ and G^-) in SWNTs because of the rolled-up structures with some chiral angles. Radial breathing mode (RBM), which has a relatively low frequency originates from radial expansion-contraction of the nanotubes. Therefore the frequency is dependent on the diameter, showing little dependence on surrounding environment.

By using lasers with different wavelengths (photon energies), more detailed characterization and identification becomes possible than bulk materials. Nonetheless, optical systems for Raman spectroscopy measurement is complicated so that available wavelengths of excitation lasers area usually limited. Not all SWNTs can be fully

detected, and also the assignment of chiral indices is very difficult especially when the diameter is large (*i.e.* the possible indices within similar diameter is numerous).

1.3.3 Electron microscopy

Electron microscopy is an indispensable tool for nanoscience and nanotechnology, where the material size of interest is smaller than the wavelengths of visible light. Since wavelengths of electrons (especially with high energy) can be smaller than the size of atom (~10^{-10} m), electron microscopy offers ultrahigh spatial resolution.

Scanning electron microscopy (SEM) is one of the most frequently used tool to characterize SWNTs. When electron beams are scanned over a sample surface, most of the incident electrons lose the energy by generating heat, but some electrons in the very vicinity of the surface (~10 nm deep) are scattered off the surface as secondary electrons. By scanning electron beams and collecting those electrons with detectors, images of the sample surface are created. SEM imaging of SWNTs highly depends on the acceleration voltage of electrons, substrates, and substances in touch.[13] In particular, SWNTs on SiO_2/Si substrates (with 1 kV acceleration voltage) "look" much thicker than the true diameter due to electron beam induced current in insulator substrates, making the spatial resolution of imaging worse.[14]

Transmission electron microscopy (TEM), in which high-energy electron beams (60–200 keV) are transmitted through samples to form images, is another widely used tool in many fields. The extremely high resolution of this technique enables the observation (visualization) of atomic layers of CNTs, providing diameter and number of layers of CNTs. In addition to the direct visualization of atoms, electron diffraction is often used in a TEM to form interference patterns by utilizing the wave nature of electrons, which for example elucidates the chiral indices (n,m) of SWNTs. Electron energy loss spectroscopy (EELS) is also an effective tool to identify the electronic structure of SWNTs in which, for example, electrons with narrow range of energies lose energy via inelastic interaction with inter-band transitions. EELS can be thus used to assign the chirality of SWNTs.[15]

1.4 Applications of carbon nanotubes

Since CNTs, tubular-shaped graphite, have light weight, high aspect ratios and large electrical/thermal conductivity, they can be used as electrical/thermal filler in low-conductivity materials (such as polymer).[16,17] From their mechanical strength, CNTs are also used for load-bearing applications to enhance stiffness and toughness of polymers. For example, ~1 wt% of multi-walled CNTs (MWNTs) in epoxy resulted in the enhancement of fracture toughness by 23% without deteriorating other properties.[18] Not only as fillers in composites, self-standing sheets and strings of CNTs have a wide range of applications.[19,20]

CNTs are also intensively used in energy-related applications, such as battery and photovoltaics. For example, high mechanical/chemical stability and electrical/thermal conductivity, as well as high surface area, of CNTs can improve the performance of Li-ion batteries [21] and supercapacitors.[22] Few-walled CNTs, if outer walls are partially unzipped *via* oxidation, effectively work as electrocatalysts for oxygen reduction reaction in fuel cells, while inner walls serves as good electrical conductors.[23] For solar cells, CNTs were used in dye-sensitized solar cells as a low-cost alternative to Pt counter electrodes,[24] then followed by recent applications in perovskite solar cells.[25] The application of CNTs in perovskite solar cells makes use of high (often, hole) conductivity with relatively large transparency, if CNTs are used instead of ITO and FTO.[26] Similar properties led to high efficiency in S-CNT heterojunction solar cells.[27] Chirality-sorted semiconducting SWNTs were also used as active layers of photovoltaics, though the power conversion efficiency was still low.[28]

The application described above mainly exploit the mechanical strength, chemical stability and high electrical conductivity of CNTs. Another unique characteristic of (especially, single walled) CNTs is a tunable band gap depending on their diameter and chirality (n,m). For example, s-SWNTs are a direct band gap semiconductor, and therefore can be used for light emitters [29] with a wide range of wavelengths. For quantum information processing and communication technologies, single-photon emission of telecommunication-wavelength at room temperature was realized by fabricating exciton trapping sites in SWNTs [30] or by utilizing exciton-exciton

annihilation in SWNTs.[31] Another promising application of SWNTs as a semiconductor is channels in field-effect transistors.[32] Moderate band gap, ultrathin bodies, and high carrier mobility both for electrons and holes render SWNTs ideal materials for high-performance transistors in logic circuits. Furthermore, SWNTs are strong candidates for transparent and flexible electronic devices, such as displays and wearable/biocompatible devices, owing to the mechanical flexibility and transparency.[33,34]

1.5 Basic sample preparation and measurement

1.5.1 Transfer of SWNT arrays onto arbitrary substrates

In this thesis, aligned SWNTs are mostly grown on crystalline quartz substrates. Although electronic devices can be directly built owing to the insulating nature of quartz, the SWNTs were transferred without changing the morphologies on highly doped-Si with a thin oxide layer on the surface for a better platform of devices fabrication. Here, Si and SiO_2 serve as gate electrodes and gate dielectric layer of field effect transistors, respectively. Also, the transfer of SWNTs from quartz substrates is important for Raman measurement. Since Raman signals at low frequency (100–300 cm^{-1}) particular to SWNTs (radial breathing mode) appear close to that of crystalline quartz, the SWNTs are often transferred onto SiO_2/Si substrates to clearly obtain the Raman spectrum from SWNTs. Unfortunately, moving SWNTs from one place to another is not easy due to the extremely thin and flexible bodies. Also, once they form bundles *via* the wan der Waals interaction, it is almost impossible to separate them without dispersion by the assistance of ultrasonication and surfactants.

Powerful tools for the transfer is to use thin films of rigid materials, such as PMMA,[35] or metallic films supported by rigid tapes [36] (*e.g.* thermal release tape) for intermediation. In the thesis, SWNT arrays were transferred *via* poly(methyl methacrylate) (PMMA) films. After spin-coating of PMMA on quartz substrates, PMMA films and the substrates were scratched along the edges with diamond tipped scribe to accelerate the etching of substrates in the next. Quartz substrates with PMMA films were then immersed in a heated KOH aqueous solution (1 mol/L) for 10 min. When the substrates were quietly immersed into deionized (DI) water, the PMMA

films were spontaneously peeled off from the substrates and floated on the water. After rinsing the PMMA film with another DI water, PMMA films (and SWNTs) were picked up by target substrates, followed by natural drying, bake, and immersion in acetone to remove PMMA.

1.5.2 Formation of metal contacts (makers) and etching

To fabricate SWNT-based transistors, SWNTs have to be contacted with (usually) metal electrodes. In general, work functions of metal used here affect the band alignment and the conduction type of the transistors (n or p type). In this thesis, two different ways of the contact between SWNTs and metal electrodes were employed. When Pt is used as contacts, Pt were first patterned by photolithography and sputtering. Then, SWNTs were transferred on SiO_2/Si with pre-patterned Pt electrodes to form bottom contact. Since Pt is hard and rigid, Pt serves as probing pads which are not damaged by probes. On the other hand, Au contacts were directly patterned on SWNTs by thermal evaporation. For both types of metals, bilayer resists (polydimethylglutarimide as a sacrificial layer) were used for easiness of the lift-off process and for smooth edges of the electrodes. The patterning of metals was done in the similar ways, when markers are fabricated for the characterization of SWNTs by SEM, AFM, and Raman spectroscopy at the same position.

1.5.3 Electrical measurement/treatment in controlled atmosphere

In this thesis, most of the measurements of transfer characteristics are conducted in air. In some occasion, atmospheres, *e.g.* pressure and gas composition, for electrical measurements and treatments are controlled through measurements in the chamber (E4, Riko Boeki) connected to gas cylinders and a rotary pump and a turbo molecular pump. The pressure can be decreased to $\sim 1 \times 10^{-2}$ Pa for the annealing of SWNTs with Joule self-heating and the measurement of field emission while avoiding damages to SWNTs. Pure oxygen, nitrogen and water vapor can be independently introduced in the chamber to obtain desired partial pressures. The temperature of a sample stage is controllable from room temperature to >100°C if necessary.

1.6 Challenges for SWNT-based computing

Figure 1.6 displays the properties of SWNTs required to build SWNT-based high-performance electronics (CMOS inverter). Alignment and position of SWNTs have to be controlled to achieve large on-state current and negligible off-state current. Crossing SWNTs, which weaken the gate control due to electrostatic screening, should be avoided. [37] To this point, lattice-oriented growth of single-crystalline substrate (*e.g.* quartz, sapphire) enables perfect alignment.[38] In addition, significant progress has been made on assembly of dispersed SWNTs in liquid,[39,40] which offers opportunities to obtain high-density arrays of monodispersed SWNTs *via* wet separation techniques.[41–44]

To maximize the potential of SWNTs, the contact between SWNTs and (often metal) electrodes needs to be carefully designed. First, electrical contact resistance has been reduced by band-alignment engineering at the interface because the contact resistance dominates the performance of ultrascaled devices; Pd electrodes are frequently used to obtain the theoretically minimum value (i.e. quantum limit, $R_Q = 1/G_0 = h/4e^2 \approx 6.5\ \text{k}\Omega$).[46] However, when the device footprints are shrunk and the contact length (overlap length of SWNTs and source/drain) accordingly decreases, the contact resistance increases because transport between a metal and nanotubes occurs

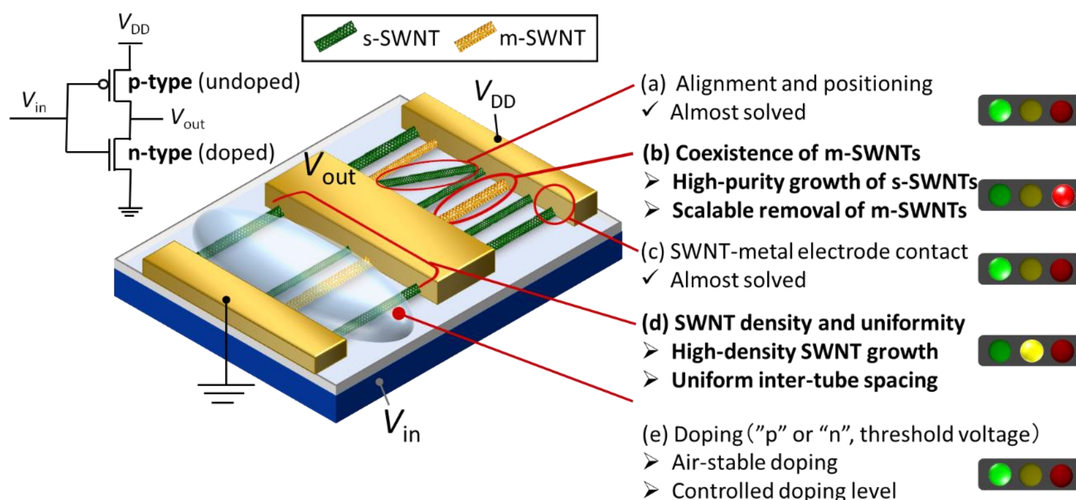

Figure 1.6 Schematic of SWNT-based inverter. (a–e) Technological issues regarding to the application of SWNTs in high-end logic devices, made by reference to ref. [45]

not only at the contact edge but also at tube walls; for example, as the contact length scaled from 100 nm to 20 nm, the contact resistance increased from $2R_c < 15$ kΩ to >35 kΩ.[47] An innovative approach of side-bonded contact schemes was formed through the reaction of Mo with SWNTs to form carbide, and realizes size-independent contact resistance.[48]

Reliable operation of logic circuits requires the control of polarity and threshold voltage of transistors, which can be tuned by doping. Instead of substituting a small portion of carbon with other elements, extra carriers are injected from outside for the use in transistor channels.[49] For example, SWNTs behave as a p-type semiconductor in air due to water/oxygen (coupling).[50] A more practical and stable means of charge transfer doping is to insert proper metal oxide between SWNTs and the gate dielectric.[51] Another way to control the threshold voltage and polarity is to choose metals with appropriate work functions (*e.g.* low work function metal is for n-type transistors),[52] and 240-nm footprint SWNT CMOS inverter was recently demonstrated using Sc-Pd contacts.[2]

Purity of semiconducting SWNTs, density, and its uniformity are still bottlenecks of high-end applications (*e.g.* replacement of Si). Regarding these two aspects, details of the development and challenges are described in Chapter 2 and 3.

1.7 Objective of the thesis

As a theoretical study predicted that SWNT-based digital systems will outperform silicon-based devices by several times in terms of both switching time and energy efficiency,[53] SWNT transistors have been fabricated with ultrascaled gate lengths (down to 5 nm)[2] or footprints including source/drain contacts (down to 40 nm),[3] demonstrating better performance than silicon devices. In addition to such excellent performances on the individual transistor level, three-dimensional digital systems that incorporated more than one million SWNT-based inverters were built for the sensing environments, and then for the storing and processing of information.[4] This proved that SWNT-based large-scale systems can work reliably and also possess unique functions.

However, it is still quite difficult to simultaneously achieve large-scale integration of ultrasmall transistors because of the difficulty in obtaining "good" SWNT starting materials suitable for device fabrication, as the challenges for SWNT application is summarized in Figure 1.6. One should start the fabrication from aligned arrays of high-density (>100 SWNTs/µm) but individual, purely semiconducting (>99.9999%) SWNTs over a large area.[54] In order to prepare such SWNT materials, the thesis deals with synthesis, purification, and fabrication/characterization of devices. Although much progress has been independently reported in s wide range of aspects (synthesis, purification, and fabrication), they are not necessary in harmony (compatible) with each other. Therefore, in this thesis, growth and sorting methods of SWNT arrays are developed in a cooperative manner for the fabrication of SWNT-based transistors that satisfies three kind of scaling; scaling to large-scale circuits, short channel lengths, and to small inter-SWNT spacing.

Structure of the thesis

The overview of the thesis is summarized in Figure 1.7. Analysis on horizontally aligned SWNTs is first described for the control of chirality, length, and density in Chapter 2. After basic studies on the aligned SWNTs, an isotope labeling technique to

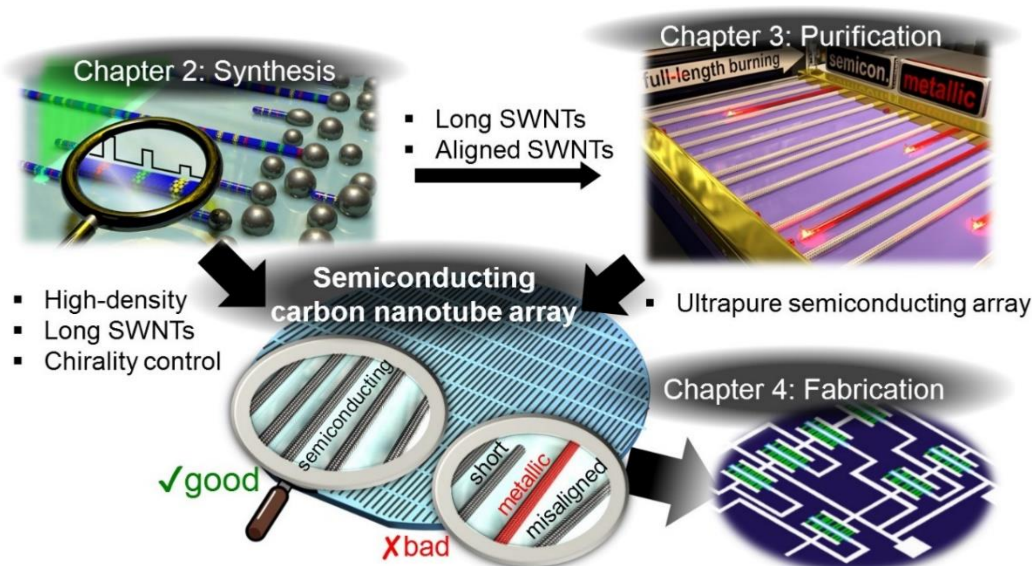

Figure 1.7 Overview of the thesis. Objective of the thesis is to prepare homogeneous, high-density, purely semiconducting SWNT arrays over a large area.

trace the growth process of long individual SWNTs *ex situ* is introduced. In addition, observation of horizontally aligned SWNTs by TEM is attempted by fabricating the thin film of poly-crystal SiO_2 that can be directly put in TEM chamber. This will offer insights into the interaction between crystalline substrates and catalysts/SWNTs, and also can be combined with the isotope labeling technique.

Chapter 3 describes the method for on-chip sorting of s-SWNT arrays for high-performance transistor application. Starting from a finding of a new phenomenon for long-length removal of m-SWNTs, thermally and chemically driven etching of SWNTs is investigated by experiments and simulations. Finally, the phenomenon is then developed into a technology that enabled a reliable sorting of s-SWNTs.

In Chapter 4, pure s-SWNT arrays are prepared by using the sorting method based on the knowledges obtain in Chapter 3. Then, multiple transistors are fabricated and characterized in comparison with other purification methods. Also, scalability of the sorting and device fabrication method is discussed in terms of large-scale circuit, short-channel transistors, and inter-SWNT spacing.

Chapter 2:

Synthesis and Analysis of Horizontal SWNT arrays

2.1 Introduction to synthesis of SWNT arrays

Growth of horizontal SWNT arrays directly on insulating substrates, such as single-crystalline quartz and sapphire, would offer the best materials for realizing high-performance SWNT transistors once chirality or electronic-type of SWNTs are perfectly controlled because of the cleanliness, high-degree of alignment, and density over a large area.[36] Since the initial reports on aligned growth on those crystalline substrates over a decade ago, significant progress has been made on length, density, and even chirality selectivity of SWNTs. In this chapter, starting from basic parts of SWNT synthesis, focuses are then directed to the SWNT configuration required for high-performance transistors and experimental investigation on the growth process of aligned SWNTs to achieve the goal. A theoretical study [53] revealed that the density of ~200 SWNTs/µm is desirable in terms of both drive current and inter-tube charge screening, and inter-tube pitch should be as uniform as possible.

For horizontally aligned SWNTs, many researchers have tried to control the density, length, and chirality of SWNTs for the application. For example, degree of alignment and density were improved at the same time by spatially patterning catalysts in stripes.[55] Multiple-cycle CVD or implanted catalyst in substrates yielded even higher-density SWNT arrays over a large area.[56,57] At the same time, chirality-controlled growth has undergone considerable progress in recent years by designing catalysts.[58,59] Nevertheless, the density and purity of s-SWNTs has not reached the levels required for the direct use in high-performance microelectronic applications.[54]

2.2 Basic analysis on horizontally aligned SWNTs

Horizontal array configuration of SWNTs obtained on single-crystal substrates is an excellent platform for the analysis on SWNT growth,[60,61] not only for the direct application of this organized structure. This chapter will deal with analysis on time-dependent length of aligned SWNTs and characterization of the SWNTs by Raman spectroscopy to build the basis for the next section.

2.2.1 CVD time-dependent length of aligned SWNTs

First, time-dependent lengths of aligned SWNTs were investigated. The SWNTs were grown by CVD with 100 sccm of Ar/H_2 and 10 sccm of ethanol. Temperature and the total pressure was 800°C and 1.5 kPa, respectively. The substrates were placed 10 cm away from the furnace edge on an upstream side. Figure 2.1(a) shows SEM images of SWNT arrays grown for different CVD times (30s, 3 min, 15 min). Histograms of the length of those SWNTs are shown in Figure 2.1(b). Density and length clearly increased with the CVD time. Figure 2.2(a) shows the average length of SWNTs as a function of CVD time. Error bars represent the standard deviation of the length. The average length can be well fitted with the equation reported before; $L(\mathrm{t}) = \gamma_0\tau(1-\exp(-t/\tau))$, where $L(\mathrm{t})$ is the average length of SWNTs, γ_0 is the initial growth rate on average, and τ is the reaction time constant. However, as revealed in next section, the growth rate of "individual" SWNTs is constant, and does not change throughout their entire lifetime (from nucleation to deactivation).

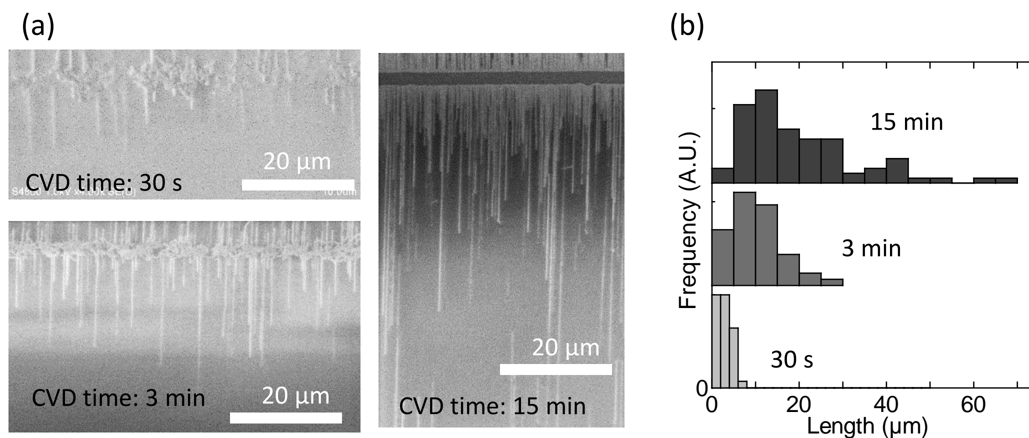

Figure 2.1 (a) SEM images of SWNT arrays grown with CVD time of 30 s, 3 min, and 15 min.(b) Histograms of the SWNT length in (a).

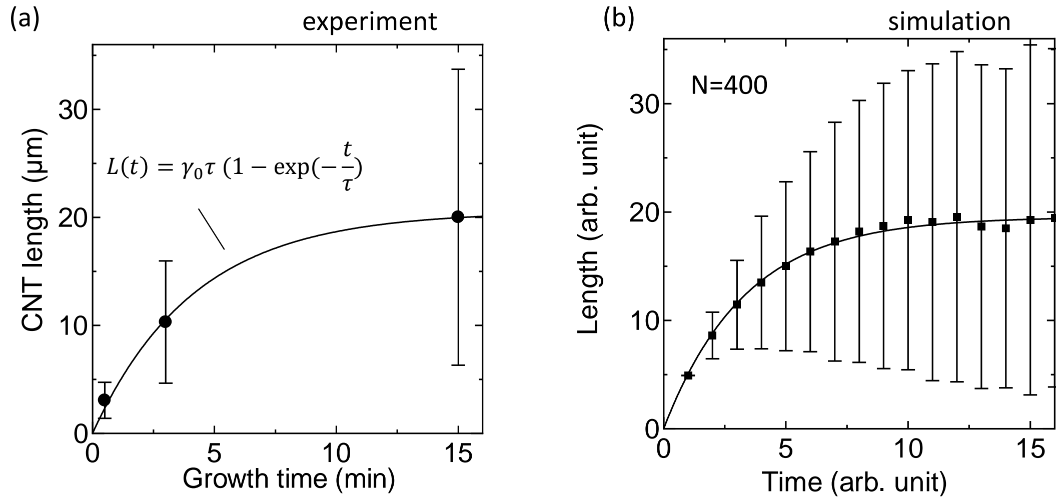

Figure 2.2 (a) Time evolution of the average length of SWNTs obtained in the experiment. (b) Simulated average length of 400 SWNTs recorded every one arbitrary unit. Error bars indicate the standard deviation.

To explain the decay of the "average" growth rate in Figure 2.2(b), a simple simulation was conducted, where the growth rate for all SWNTs is constant (= γ_c), but the growth stops randomly and suddenly with a certain probability ($p = 1/\tau_p$) every arbitrary time unit. The fitted parameters from Figure 2.2(a) (γ_0 = 4.96 µm/min, τ = 4.16 min) were used as two parameters (γ_c and τ_p) for the simulation. Time evolution of the simulated average length is plotted in Figure 2.2(b), and can be well fitted with the same equation ($L(\mathrm{t}) = \gamma_0\tau(1-\exp(-t/\tau))$). In addition, standard deviations of the length is very similar to the experiment. This result independently indicates that the growth rate of individual horizontally aligned SWNTs is constant, but the average (or summation) follows the exponential decay because the ratio of active (growing) SWNTs decreases with time.

Next, the growth rate was scaled by ethanol partial pressure p_{EtOH} and the heating length of carbon feedstocks L_{heat}. With the growth condition in Figure 2.1 defined as a standard, average length evolution of SWNT grown with different L_{heat} and p_{EtOH} is compared in Figure 2.3(a) and (b), respectively. Although the absolute length was different for both cases, if the SWNT length L_{CNT} is normalized by the gas heating time L_{heat} or the CVD time t_{CVD} is normalized by ethanol pressure p_{EtOH}, the growth

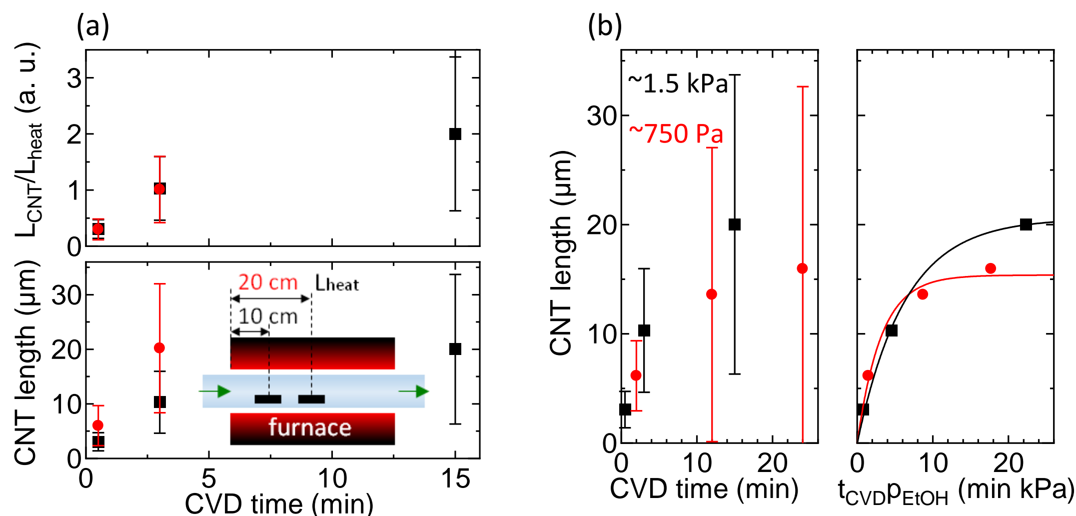

Figure 2.3 (a) Time evolution of the average length of SWNTs obtained in the experiment. (b) Simulated average length of 400 SWNTs recorded every one arbitrary unit. Error bars indicate the standard deviation.

curves well agree with each other, indicating the relationship $\gamma_0 \propto L_{heat} \cdot p_{EtOH}$, though influence on the growth time constant τ might be different for these parameters.

2.2.2 Chirality (*n*,*m*) assignment of SWNTs by Raman spectroscopy

For the analysis of chirality-dependent the growth and the nucleation (population) of SWNTs, assignment of the chirality, *i.e.* chiral indices (*n*,*m*), is necessary. Enormous efforts have been invested on the chirality assignment, using spectroscopy and microscopy. Transmission electron microscopy is a representative method for the structural identification of nanomaterials, like SWNTs. In addition to direct high resolution imaging of carbon atoms, electron diffraction is often used for the assignment of SWNT chirality,[1] which observes diffracted electrons instead of transmitted electrons. Scanning tunnel microscopy (STM) is one variety of scanning probe microscopy, like atomic force microscopy (AFM), and can directly observe the atomic arrangement in SWNTs.[62] However, those microscopy techniques require special structures of samples, such as air-suspended or support on metal substrates, and also a lot of time for the determination of chiral indices.

On the other hand, three types of spectroscopy are often used for the chirality assignment; Raman spectroscopy, photoluminescence (PL) spectroscopy,[63] and

Rayleigh spectroscopy.[64] Since PL spectrum is difficult to obtain from the SWNTs on substrates and m-SWNTs, it cannot be used in this study. Rayleigh spectroscopy was introduced as a powerful tool for probing electronic structure and the chirality of SWNTs of any kinds, including m-SWNTs, air-suspended structures, and on-substrates.[64,65] However, the technical difficulty of measurement due to the direct observation of elastic scattering makes this technique not available for every laboratory. Raman spectroscopy is therefore most frequently used for the characterization of SWNTs on substrates or suspended in a liquid, especially when the amount is small because of relatively large signals owing to the resonance effect. In spite of a number of studies on Raman spectroscopy, the chirality assignment is not easy because both the optical transition energy and RBM frequency can be shifted depending on the environment; air-suspended, dispersed in liquid (wrapped by surfactants), or supported on various substrates.[66] Therefore, Kataura plot has to be slightly modified for each type of samples.

In this study, a number of Raman spectra were obtained from individual horizontally aligned SWNTs. First, the SWNT arrays were grown on quartz substrates, and then transferred onto SiO_2/Si substrates via PMMA thin films. Excitation laser with 532 and 488 nm wavelength was used because they can detect a wide range of s-SWNTs and also has a strong laser power. Among numerous RBM peaks, those with peak frequency between 180 and 200 cm^{-1} ($2n + m = 32$ family) were studied first because the RBM peaks in this region can be assigned relatively easily.

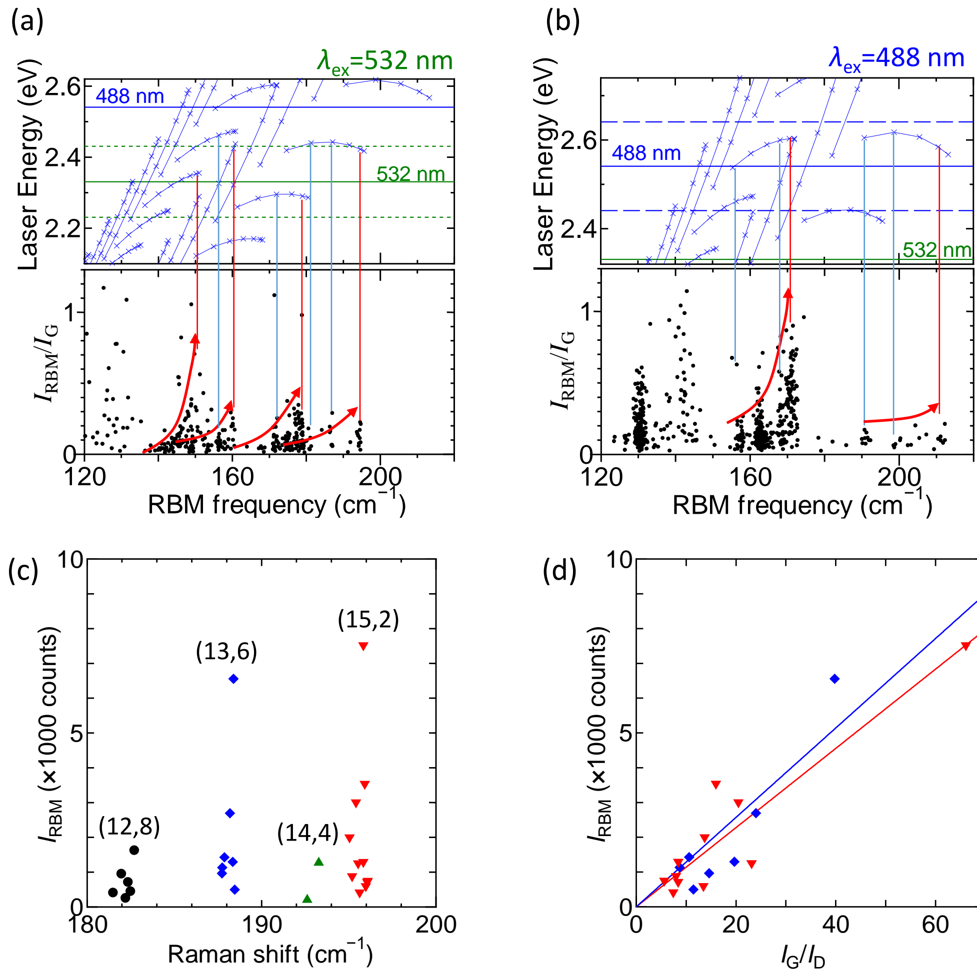

Figure 2.4 (a,b) Kataura plot (top panel) and RBM intensity normalized by G-mode intensity *versus* Raman shift (bottom panel) with excitation wavelengths of 532 nm (a) and 488 nm (b). X-axis of Kataura plot is shifted from the literature by to 6 cm^{-1} to positive value for this sample. RBM intensity is plotted (c) as a function of RBM frequency ω_{RBM} in $180 < \omega_{RBM} <$ 200cm^{-1}, (d) as a function of G/D ratio I_G/I_D for the SWNTs with (15,2) and (13,6) chiralities, indicating linear relationship.

The intensity of all the RBM peaks were normalized by G-band intensity and plotted as a function of RBM frequency in the bottom panels Figure 2.4(a) and (b) for excitation wavelengths of 532 and 488 nm, respectively. In Figure 2,4(a), two branches are roughly found in the ranges of 140–170 cm^{-1} and 170–200 cm^{-1} with different intensity. In the lower frequency range (140–170 cm^{-1}), the group with stronger intensity is likely to be assigned to the $2n + m = 43$ family, while the weaker one is to the $2n + m = 40$ family, judging from the energy match of incident photons and optical transition of SWNTs. In the lower frequency range (170–200 cm^{-1}), the groups with

strong and weak intensity probably belong to the $2n + m = 35$ and 32 families, respectively. Since it is well known that near-zigzag (smaller chiral angle) SWNTs has stronger RBM intensity than near-armchair (larger chiral angle) SWNTs,[67] each branch seems to have strong RBM intensity as Raman shift increases. Similar things can be applied to the spectra excited by 488 nm laser (Figure 2.4(b)).

Figure 2.4(c) and (d) shows RBM frequencies ω_{RBM} *versus* the intensity I_{RBM}. Although (16,0) and (15,2) SWNTs have RBM peaks at close frequencies, chirality of all the SWNTs with $\omega_{\mathrm{RBM}} \approx 196$ cm^{-1} was assigned as (15,2) because the growth rate of zigzag SWNTs is known to be very slow.[58] Interestingly, SWNTs with the apparently identical chirality have much different intensity of RBM peaks. Then, the RBM intensity of two representative chiralities (15,2) and (13,6) were plotted as a function of G/D ratio in Figure 2.4(d), showing the linear relationship.

Since it is still difficult to assign the chirality in the low frequency region (large-diameter SWNTs), another clue for chirality assignment is discussed for the horizontally aligned SWNTs on substrates. It is known that G^{-} and G^{+} modes of SWNTs, which is related to an optical in-plane phonon of the graphite, are dependent on the diameter, chiral angle, and family pattern.[68] In the previous study, intensity

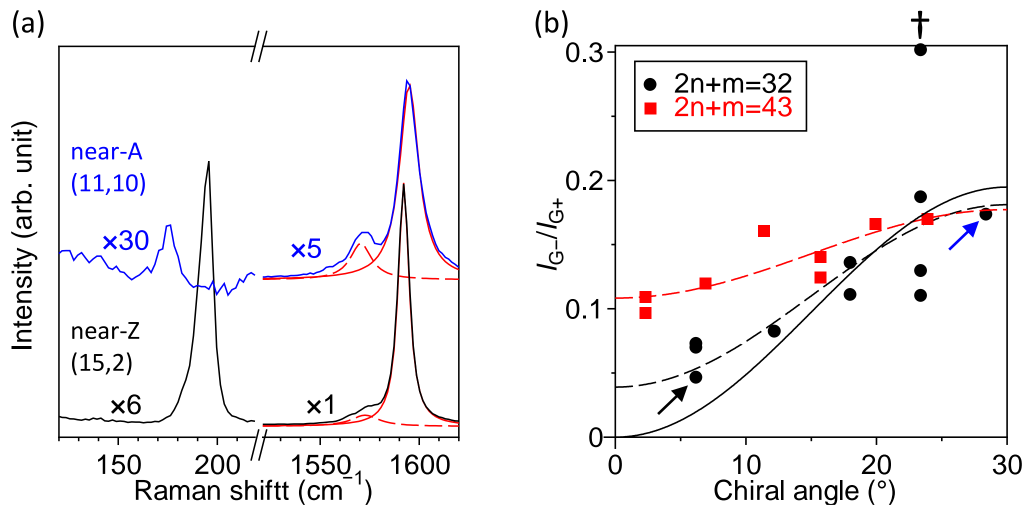

Figure 2.5 (a) G mode and RBM spectra of the SWNTs whose chiralities were assigned as (11,10) and (15,2). Both spectra are normalized by G peaks. Red dashed and solid lines are Lorentzian fitting curves for G^{+} and G^{-} modes, respectively. (b) G^{-} intensity ratio to G^{+} intensity ($I_{\mathrm{G-}}/I_{\mathrm{G+}}$) as a function of chiral angle for $2n + m = 32$ (black circles) and 43 (red rectangles) families. Blue and black arrows indicate the SWNTs shown in (a). Solid and dashed lines are obtained by the fitting of the plots with Eq. 2.1 and 2.2, respectively.

ratio $\partial I = I_{G-}/I_{G+}$ was expressed as a function of diameter and chiral angle, but the diameter dependence is small when the family is the same. Therefore, it can be simply expressed as below.

$$\partial I(d,\theta) = \frac{I_{G-}}{I_{G+}} = a_1(1 - \cos(6\theta)) \quad (2.1)$$

where a_1 is constant and θ is the chiral angle of SWNTs.

It is relatively easy to assign the chirality for the $2n + m = 32$ family because of less candidates than larger-diameter SWNTs. Even SWNTs of five different chirality ((15,2), (14,4), (13,6), (12,8), (11,10)) are selected. Figure 2.5(a) shows the normalized G-band and RBM spectra of a (11,10) SWNT and a (15,2) SWNT, where G-band is further broken down to G+ and G^- modes. $\partial I = I_{G-}/I_{G+}$ was plotted as a function of chiral angle for 11 SWNTs. The data are first fitted by Eq. 2.1 (solid line in Figure 2.5(b)), but the G^- mode does not seem to decrease to zero for the zig zag tubes. Therefore, a slightly different equation is introduced for better fitting as below.

$$\partial I(d,\theta) = \frac{I_{G-}}{I_{G+}} = a_1(1 - a_2\cos(6\theta)) \quad (2.2)$$

where a_2 is constant ($0 < a_2 < 1$). This equation well agrees to the experimental data in Figure 2.5(b), indicating G-mode of SWNTs is also affected by isotropic force of a substrate support.

2.3 Digitally coded isotope labeling for monitoring SWNT growth

For reliable device fabrication from aligned SWNT arrays, especially when a lot of transistors integrated into a system, the SWNT arrays must be spatially homogeneous over the entire area (*e.g.* wafers). This means that SWNTs need to be long enough if the SWNTs grown from stripe-patterned catalysts on substrates.[55] However, in many cases, some SWNTs grow long but some SWNTs stop growing, ending up with short segments. This is one of the reason for the ununiformity of density of SWNT arrays.

To elongate the lifetime of SWNT growth and ensure that all the SWNTs start growing from one side of catalyst stripe to the other side of the stripe, we first need to understand how and why SWNTs terminate their growth. Although there have been many studies on the lifetime of SWNTs, most of them observed bulk ensembles of CNTs (mainly forests and random networks). Since tube-tube interaction and gas diffusion can be a limit of the growth in the high-density forest form, the mechanism of growth termination might be different between horizontally/vertically aligned SWNTs. Also, each SWNT has a different lifetime, so that time evolution of the averaged length does not always give accurate information on an SWNT growth rate. In addition, the growth rate is known to depend on chiralities and catalysts properties,[69,70] making the analysis on lifetime and growth rate much difficult.

The other type of studies is *in situ* Raman/TEM/SEM measurement of individual CNTs,[70–74] where a short SWNT is generally observed in one cycle of growth. For instance, in situ TEM observation gives real-time CNT images very much in detail; however, the growth condition for this technique is much different from that for the CNTs for practical application, whose lengths are usually >1 μm (sometimes >1 mm). The nature of *in situ* experiments makes a statistical investigation difficult because the number of the CNTs observable in a single experiment is limited and the growth condition could subtly change each time.

2.3.1 Tracing the growth histories of horizontally aligned SWNTs

Isotope labeling with high-purity ^{13}C feedstock has been used for the monitoring of bulk SWNTs ensembles and graphene (such as vertically aligned structures).[75–

79] Unlike graphene synthesis, for which isotope labeling was often used to visualize the growth process, growth process of SWNTs have considerably wide varieties, such as morphologies, chiralities, and catalyst nanoparticles. This has made the use of isotope labeling on individual SWNTs very much limited;[76] one example offered information for proving the base growth mechanism of lattice-oriented SWNTs. Costs of experiments derived from expensive ^{13}C feedstocks hinder intensive studies using carbon isotopes. Hence, the isotope labeling on individual SWNTs has a plenty of room to be explored and improved.

Here, the targets of our interest is narrowed down to lifetime, growth rate, and incubation time of SWNTs with identified chiralities. Figure 2.6(a) illustrates the concept of digital isotope coding (digitally coded isotope labeling). Since our CVD system operates at low pressures (~1 kPa), switching among different species of carbon feedstocks can occur very quickly, making the fine labeling on SWNTs. Four different ratios (0, 33, 67 and 100%) of ^{13}C ethanol were introduced during the growth process to embed binary-like codes in SWNTs. Raman spectra obtained from four different

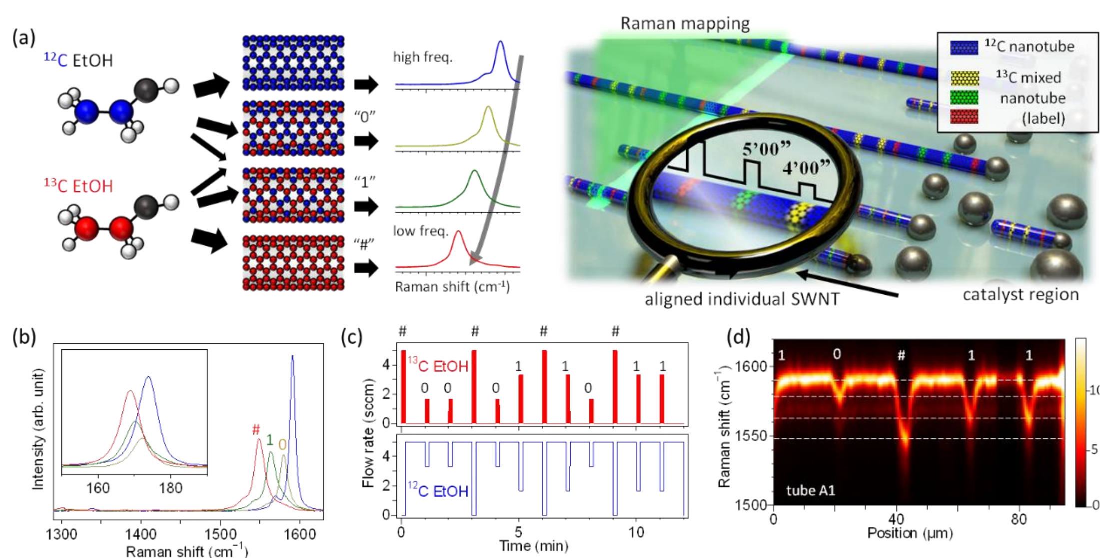

Figure 2.6 (a) Schematic of isotope labeling to trace the growth of individual SWNTs. (b) Raman spectra of SWNTs grown from ethanol with four different fractions of ^{13}C. Isotope labels with one-third and two-thirds of ^{13}C are defined as label "0" and label "1", respectively, while SWNTs grown from 100% ^{13}C is named "#", signaling a start of new binaries. Excitation wavelengths was 532 nm. (c) An example of gas flow rate of ^{12}C ethanol and ^{13}C ethanol for isotope coding. (d) Intensity of Raman spectra along the axis of a representative SWNT (tube A1).

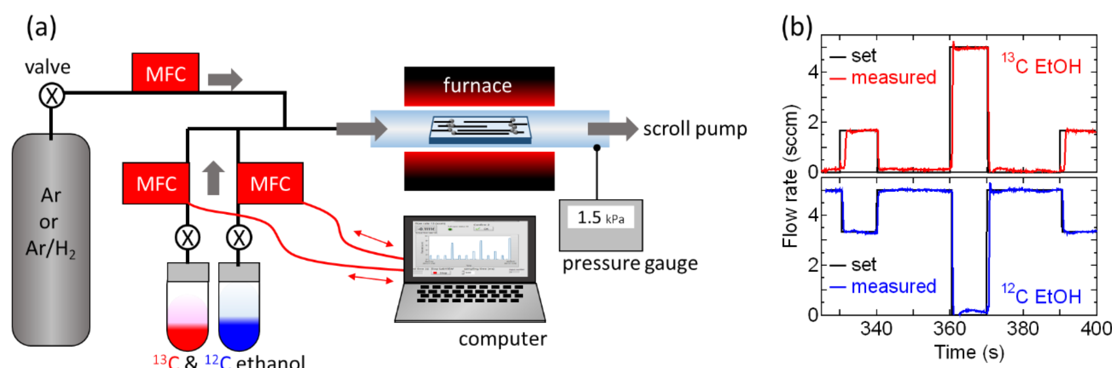

Figure 2.7 (a) Schematic of the CVD system for isotope-labeled growth. Buffer gas (Ar or Ar/H_2 mixture) and $^{12}C/^{13}C$ ethanol were introduced into a CVD reactor (quartz tube). Two types of ethanol was separately and precisely controlled *via* a computer program (LabVIEW, National Instruments). During the CVD, pressure of the reactor was reduced <2 kPa to let ethanol flow into the reactor without heating. (b) Set and measured flow rate of two types of ethanol.

Table 2.1. Example of 2-bit isotope coding.

2 bit label number	0	1	2	3	4	5	6	7	8	9	10	11
^{13}C ratio (%)	100	33	33	100	33	67	100	67	33	100	67	67
label type	#	0	0	#	0	1	#	1	0	#	1	1
group		0			1			2			3	

positions of the same SWNT are show in Figure 2.6(b). Excitation wave length of 532 nm was used in all experiments, unless otherwise mentioned. A 33% difference of ^{13}C ethanol content resulted in >10 cm^{-1} shift of the G-band, and thus each label can be easily distinguished. An example of CVD time versus ethanol flow rate is shown in Figure 2.6(c). Table 1 explains the concept of digital coding with isotope labels. The Raman intensity map along the tube axis (Figure 2.6(d)) shows a clear sequence of isotope codes.

Note that naturally evaporated ethanol at room temperature can be introduced into a reaction chamber because the total pressure in the reaction chamber was as low as 1.5–1.7 kPa. The low pressure growth was beneficial to obtain relatively a large gas velocity (~0.4 m/s) to fasten the switching of two isotope ethanol gases in the chamber. Figure 2.7(a) shows a schematic of the CVD system for digital isotope coding. Computer-controlled mass flow controllers have quick response, enabling the accurate introduction of two types of carbon isotopes (Figure 2.7 (b)).

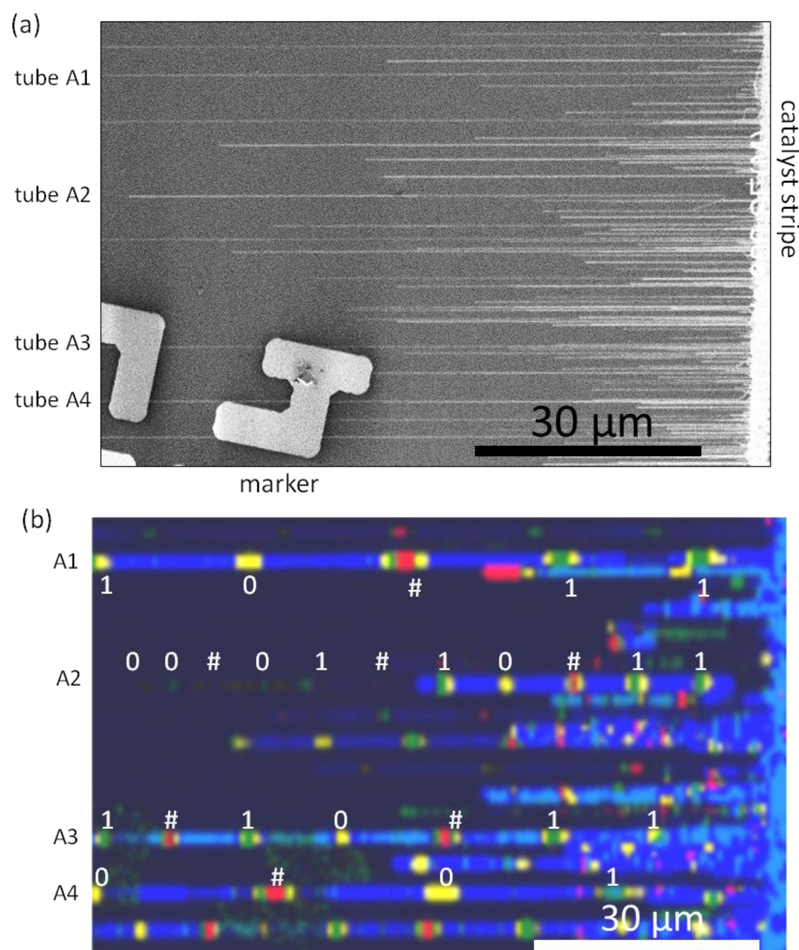

Figure 2.8 SEM image (a) and Raman mapping image (b) of the same SWNT arrays. Named SWNTs (tube A1–4) are labelled with white letters (digital codes) in (b).

SEM and Raman mapping images were obtained from the same area as shown in Figure 2.8(a) and (b), respectively. Blue, yellow, green, and red parts are corresponding to pure ^{12}C nanotubes and isotope labels (0,1 and #), respectively. In Figure 2.8(b), label type is affixed on three SWNTs (tube A1–4). The isotope labels introduced later (*e.g.* 1-0-#-1-1) appeared near the original catalyst position, clearly indicating the base-growth mode for all the SWNTs observed in this study (more than 100 tubes). The result agrees well with the study on horizontally aligned SWNTs grown on sapphire from iron catalysts,[76] but disagrees with the ones grown on ST-cut quartz from copper catalysts.[80] For an SWNT with a high growth rate (~20 μm/min), continuous transition of G-band position was observed, which provides a hint on gas flow inside the CVD chamber.

2.3.2 Growth histories of individual SWNTs

Aligned SWNTs were grown at 800° C for 12 min (t_{CVD} = 12 min) with one minute intervals (Δt = 1 min) of 2-bit isotope labeling (Figure 2.9(b)). One CVD cycle consumed only <20 μL (<15 mg) of ^{13}C ethanol but yielded more than one million SWNTs. Each SWNT needs at least two or three labels for the identification of the exact time under this condition. Time evolution of lengths and growth rates of three representative SWNTs is plotted in Figure 2.9(a). One SWNT (tube A4) started to grow in timing with the ethanol supply and kept elongating at a constant rate ($d\gamma/dt \approx 0$) until the growth termination at $t \approx 6$ min. The other SWNTs (tube B1 and B2) initiated the growth after the incubation and were still growing when the ethanol

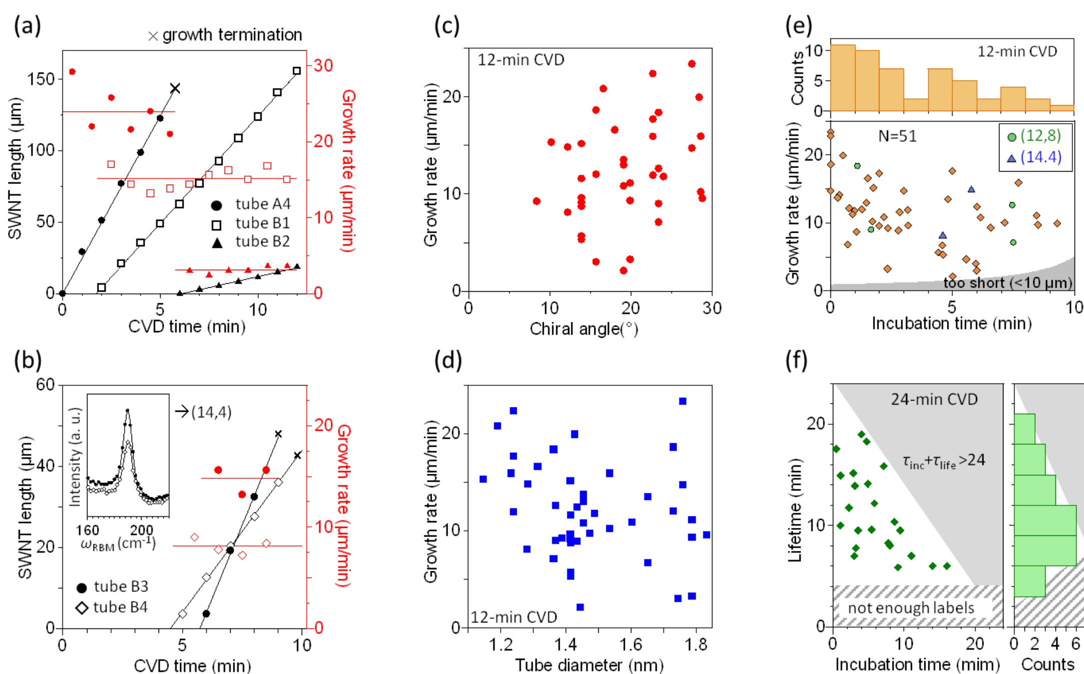

Figure 2.9 (a) Time evolution of lengths and growth rates of representative SWNTs obtained from isotope labeling. Crossed marks (x) represent termination of growth before the end of a CVD cycle at 12 min. One (black circle) stopped growing abruptly at $5 < t < 6$ min. The others (open square and triangle) were still growing when the ethanol supply was stopped. (b) Time evolution of length (black) and growth rate (red) of two SWNTs with same chirality (14,4). Inset: RBM spectra of both SWNTs had a peak at 190 cm^{-1} (c,d) Growth rate as a function of chiral angle (c), and tube diameter (d). (e) Growth rate *versus* incubation time of the growth. Green circles and blue triangles indicate the same (n,m) SWNTs. Top panel: Histogram for the incubation time. f, Incubation time *versus* growth lifetime for SWNTs with t_{CVD} = 24 min. Right panel: Histogram for the lifetime.

supply was stopped (t = 12 min). It is worth mentioning that this is the first report for time-resolved growth process of individual SWNTs with a practical form for semiconductor applications (>100-μm aligned arrays).

The abrupt termination was predicted in the previous study which analyzed the length distribution of ultralong CNTs and concluded that CNT lengths follows Schulz-Flory distribution.[81] For all the SWNTs, the growth rate did not change much with time, unlike the growth mechanisms reported in many literatures.[70,82–85], but in good agreement with other literatures that claimed the abrupt termination.[81,86] However, it was found that average length L of many SWNTs follows the exponential decay (Figure 2.2(a)), which is consistent with previous reports on bulk SWNTs.[82,83,87] This is because the number of actively grown SWNTs decreased with time. A simple simulation that assumes a constant growth rate and the random termination with a certain probability (Figure 2.2(b)) shows a clear exponential evolution ($L = \gamma_0\tau(1-\exp(-t/\tau)$[83]) of average length. The iron nanoparticles were thus likely to keep the catalytic activity at the same level right until the growth termination, which is probably caused by encapsulation with amorphous carbon.[88] This is supported by the fact that the catalyst size did not change much during the CVD process. These results indicate that the catalyst lifetime could be extended by some sort of reactivation, *e.g.* removal of amorphous carbon on catalysts.

It is still controversial whether the growth rate of SWNTs depends on their chirality.[61,69,70,89] This needs to be addressed because the difference in growth rate has been a key to achieve chirality-controlled synthesis of SWNTs, together with thermodynamic control of the nucleation. One might wonder whether the growth rate of SWNTs with the same chirality is the same under the identical CVD condition. Figure 2.9(b) shows an example of two SWNTs with radial breathing mode (RBM) frequency of ~190 cm^{-1}, which had similar lengths but much different growth rate (~8 and ~15 μm/min). This result indicates that linking growth rates to the chirality usually needs to be done in a statistical manner to take into account this kind of variation.

This difference in growth rate even for identical chiralities may originate from the variation of catalyst nanoparticles, as a recent TEM study revealed that smaller tube/particle diameter ratios led to larger growth rates due to the difference of growth modes (so-called “tangential” and “perpendicular” modes).[72,89] Our CVD

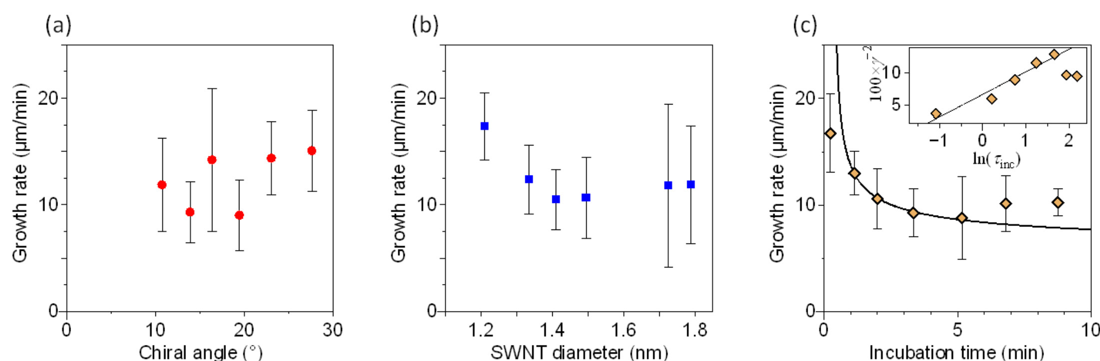

Figure 2.10 (a–c), Average growth rate of SWNTs which had different chiral angle (a), tube diameter (b), and incubation time (c). Error bars show 90% confidence interval.

conditions are likely to yield SWNTs rather by a perpendicular mode because the tube/particle height ratio widely ranged around 0.25–0.73 according to AFM measurements.

Figure 2.9(c) shows the growth rate as a function of chiral angle θ. The length of analyzed SWNTs ranged from 10 to 220 µm. There are seem to be a weak tendency that near-armchair SWNTs grew faster than other SWNTs, in accordance with previous studies.[69,70] However, the growth rate has a large variation among the SWNTs with similar chiral angle, which indicates the growth rate cannot be uniquely determined by the chiral angles. Note that the density of SWNTs was higher near catalyst stripes than the spatial resolution of Raman measurement in the present growth condition, and therefore the abundance of SWNTs cannot be accurately discussed here (see Figure 2.11 for length bias by Raman measurement).

As the chirality (chiral angle) does not uniquely determine the growth behavior, growth rate is then plotted against the tube diameter. Here, excitation wavelengths of 488 and 532 nm were used to cover a wide range of diameter. Figure 2.9(d) shows the overall tendency that smaller-diameter SWNTs grew faster. Note that this result does not necessary mean there is an intrinsic dependence of the growth rate on chirality or diameter of SWNTs because this tendency can also be explained by other factors such as the size ratio between SWNTs and catalysts.[89]

In Figure 2.9(e), the growth rate is plotted against incubation time τ_{inc} for the 12 min CVD process. Digital isotope coding revealed that each SWNT had much different incubation time from ~0 to ~10 min, though it was previously reported that incubation

time strongly depends on the pressure of carbon feedstock.[90,91] In addition, there is a trend that fast-growing nanotubes had shorter incubation time for first 5 min (see also Figure 2.10(c)). The correlation is not biased by the limitation for the lengths of analyzable SWNTs, as SWNTs too short (<10 μm) would be plotted in the gray region in Figure 2.10(e). Since the pressure of carbon precursors has a positive and negative correlation with growth rate and incubation time, respectively, this result implies each SWNT felt different driving force of the growth. The SWNTs with different chiralities are denoted with red and blue stars for (12,8) and (14,4) indices, respectively. Four SWNTs with (12,8) chirality had much different growth rate and incubation time.

Figure 2.10(c) shows the average growth rate and 90% confidence intervals (error bars) of SWNTs with similar incubation time. In the theory of bulk crystal growth, a barrier height of Gibbs free energy for nucleation ΔG^* has a relation with a growth driving force (or a difference of chemical potential between gas and solid phases) ($\Delta G^* \propto \Delta\mu^{-2}$). Nucleation rate is thus proportional to $\exp(\Delta G^*/k_B T)$ ($\propto \tau_{inc}^{-1}$). On the other hand, growth rate is simply proportional to the chemical potential difference ($\gamma \propto \Delta\mu$). The relationship between the growth rate and the incubation time is written as below.

$$\gamma = (C_1 \ln \tau_{inc} + C_2)^{-\frac{1}{2}} \qquad (2.1)$$

where C_1 and C_2 are constants. In Figure 2.11(c), the equation describes the growth well for the first 5 min. This indicates each SWNT feels different driving forces even under the same condition (pressure and temperature). The difference probably originates from the variation of catalyst nanoparticles, so microscopic observation such as TEM should be combined with the isotope labeling analysis.

Another CVD for 24 min was conducted to discuss the growth lifetime. The length of analyzed SWNTs was 50–230 μm. In Figure 2.9(f), the growth lifetime τ_{life} is plotted against the incubation time τ_{inc}. The plots are randomly scattered, and there seems to be no correlation between the incubation time and the lifetime of SWNT growth. This is reasonable if the growth termination is indeed induced by accidental encapsulation of catalyst nanoparticles with amorphous carbon, as the growth rate was constant throughout the CVD process. No data points exist in the gray area and hatched area due to shortage of CVD time ($t_{CVD} < \tau_{inc} + \tau_{life}$) and insufficient number of labels to identify the time ($\tau_{life} < (k+1)\Delta t$), respectively. Considering such biases in a histogram of the lifetime (right panel of Figure 2.9(f), the lifetime of SWNT growth was randomly determined.

Figure 2.11(a) shows the length, growth rate and incubation time of the SWNTs characterized here. It should be stressed that the all the SWNTs cannot be analyzed by this technique due to the poor spatial resolution (~1 μm) of Raman measurement. Since the SWNTs were grown from catalyst nanoparticles patterned in stripes, it was easier to distinguish the labels in long SWNTs than those in short SWNTs in crowded area. The length distribution is shown in Figure 2.11(b), in comparison with that obtained

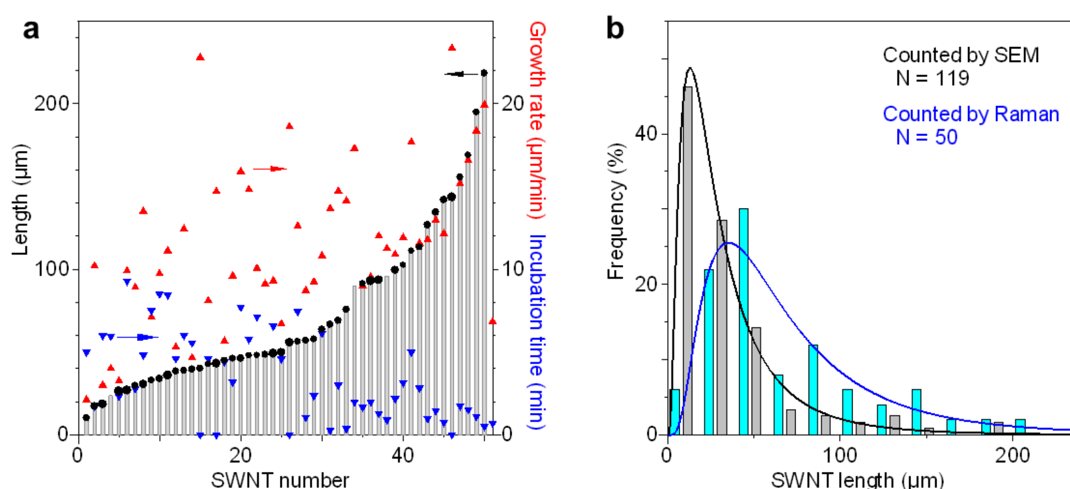

Figure 2.11 (a) Length, growth rate and incubation time of 30 SWNTs characterized by Raman. The size of black circles is proportional to the diameter of SWNTs. (b) Length distribution of SWNTs counted by SEM and Raman spectroscopy. Both SWNTs were grown on the same substrates. The difference of the length is biased by the difficulty of Raman characterization of short SWNTs when the density is high.

by SEM, though even SEM cannot distinguished all the SWNTs if they are closely lying or too short.

The D-band of CNTs is often related to structural defects. The growth rate is plotted against D/G ratio (I_D/I_G) in Figure 2.12(a). The growth rate and D/G ratio have positive correlation. This seems to be explained by, for example, less defect-healing time allowed for fast-growing SWNTs.[92] However, D/G ratio also has positive correlation with RBM frequency (inverse of diameter), which, for example, originated from the diameter-dependent sensitivity to the environment (substrates, polymer residues and so on). Also, a theoretical study reported that thinner SWNTs more easily form topological defects.[92] If D-band intensity does have intrinsic diameter dependence, Figure 2.12(a) just shows the diameter-dependence (Figure 2.12(c)) in a different way. In order to rule out such dependencies, comparison of the similar relation among the same (n,m) SWNTs was performed (Figure 2.12(c)). Correlation

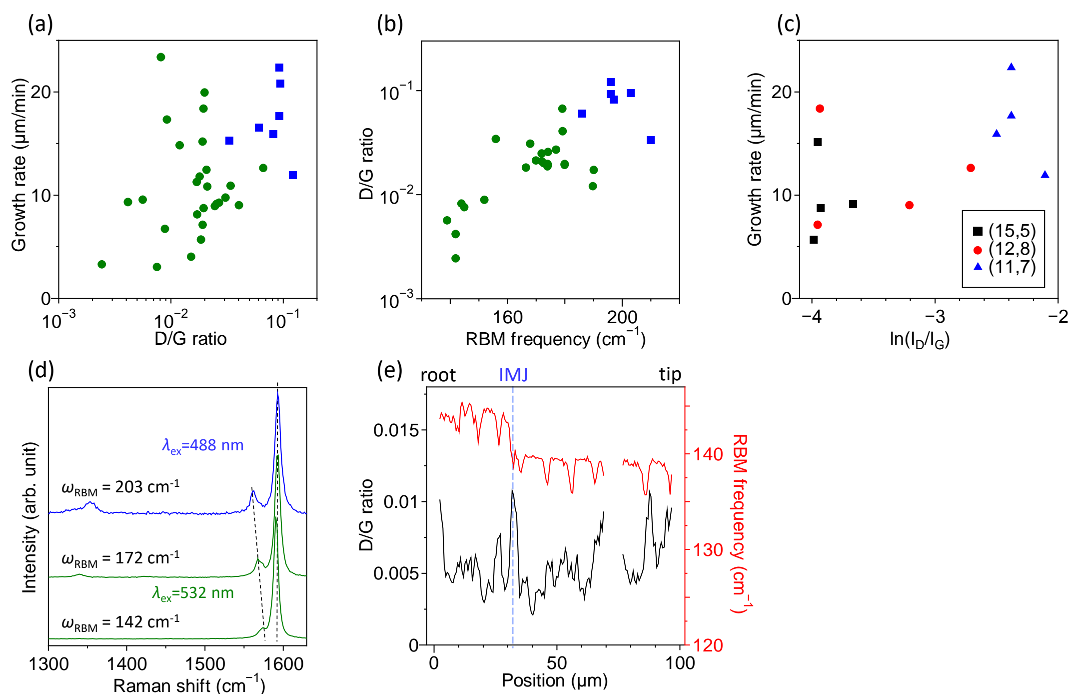

Figure 2.12 (a) Growth rate is plotted against the D/G ratio of Raman spectra, showing positive correlation. Spectra obtained with excitation wavelengths of 488 and 532 nm are plotted in blue and green, respectively. (b) Relation between RBM frequency (diameter) and D/G ratio, clearly showing positive correlation. (c) Growth rate is plotted against the D/G ratio for three different chiralities. (d) Raman spectra of three SWNTs. (e) D/G ratio along the SWNT with intramolecular junction (tube C1).

of the growth rate and D/G ratio is not prominent to claim the dependence. This leaves rooms for further investigation.

Typical Raman spectra of three different chirality (diameter) are shown in Figure 2.12(d). Figure 2.12(e) shows transitions of D/G ratio and RBM frequency along the tube C1. D/G ratio was large at the intramolecular junction. Note that for the identical SWNTs that were resonant to both blue (488 nm) and green (532 nm) lasers, Raman spectra excited by blue laser had 20–40% larger D/G ratio.

2.3.3 Analysis on spontaneously formed intramolecular junctions

Intramolecular junctions (IMJs) of SWNTs were found and analyzed optically and electrically in previous studies.[93,94] In this study, SWNT IMJs are utilized to elucidate the intrinsic chirality-dependent growth rate of SWNTs because differences in catalytic activity among different nanoparticles can be ignored. Figure 2.13(a) shows a schematic of SWNTs with IMJs. Though the chirality change along an SWNT is a rare event, isotope-labeled *ex situ* measurements enable the identification of length evolution of such SWNTs with IMJs.

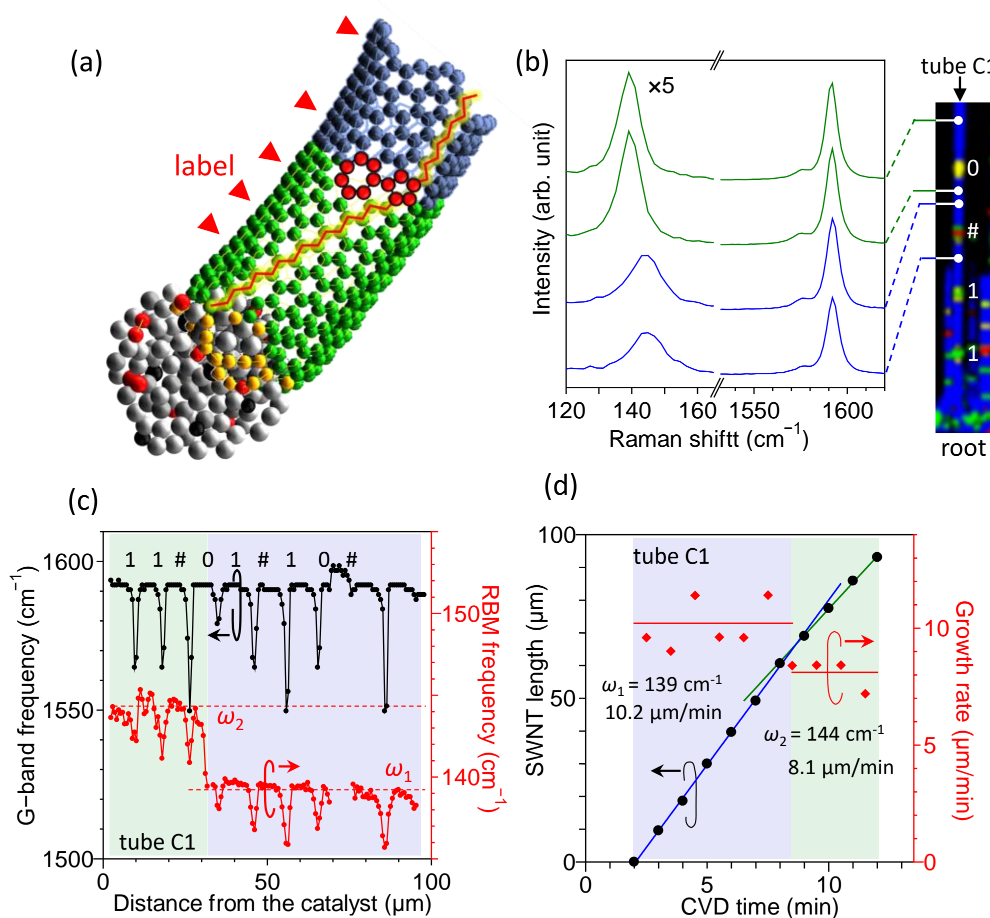

Figure 2.13 (a) Schematic of the SWNT with spontaneous intramolecular junction. (b) Raman spectra along an SWNT (tube C1) at four different points in a Raman mapping image on right. (c) Frequencies of G-mode and RBM signals of the SWNT (tube C1) *versus* distance from the catalyst. Root part ($0 < x < 30$ μm) and tip part ($30 < x < 95$ μm) have RBM frequencies around 139 cm^{-1} and 144 cm^{-1}, respectively. (d) Time evolution of length (black, left axis) and growth rate (red, right axis) of the SWNT. Chirality change occurred around t = 8.5 min, decreasing the growth rate.

Table 2.2 | Summary of the growth rate of SWNTs with IMJs.

name		γ (μm/min)	ω_{RBM} (cm^{-1})	n,m	d_t (nm)	θ (°)
tube C1	tip	10.2	139(.4)	14,13	1.83	28.8
	root	8.1	144(.4)	14,12	1.76	27.5
tube C2	tip	8.7	141(.8)	17,9	1.79	19.9
	root	15.0	145(.8)	18,7	1.75	15.7
tube C3	tip	8.1	169(.3)	14,7	1.45	19.1
	root	9.0	167(.0)	semicon.	(1.47)	—
tube C4	tip	5.0	173(.5)	15,5	1.41	13.9
	root	11.6	169(.5)	14,7	1.45	19.1
tube A2	tip	6.8	—	metallic	—	—
	root	9.1	174(.3)	15,5	1.41	13.9
tube D3 †	tip	9.0	173(.0)	11,10	1.42	28.4
	root	4.8	152(.9) ‡	18,5	1.67	16.5

† The SWNT was grown at 750°C; ‡ RBM spectrum was obtained with 633 nm excitation. The first decimal place in brackets of RBM frequency ω_{RBM} is not important features because each SWNT has some variation along its axis.

As shown in Figure 2.13b, two different RBM spectra were obtained from an SWNT at different positions, while the G-band was uniform over a whole length. Figure 2.13(c) shows peak positions of G-band and RBM signals long the axis of a representative SWNT with an IMJ. The digitally coded isotope labels are clearly observed both in G-band and RBM, indicating that the SWNT is an individual one, and not multiple SWNTs. Peak position of RBM is obviously shifted from 139 cm^{-1} to 144 cm^{-1} at x = 32 μm. The time evolution of length and growth rate is plotted in Figure 2.8(c). This clearly shows an abrupt change in growth rate from 10.2 μm/min to 8.1 μm/min at t = 8.5 min, when the RBM frequency changed from 139 to 144 cm^{-1}.

Including several more SWNTs with IMJs, chiralities and growth rate before and after the chirality change are summarized in Table 2.2. The relative change of growth rate that originated from IMJs can be a powerful tool to discuss the chirality-dependent growth rate. This cannot be easily achieved just by observing the growth of many SWNTs because the growth rate of different SWNTs grown from different catalyst nanoparticles cannot be directly compared due to the variation of catalysts (Figure 2.9).

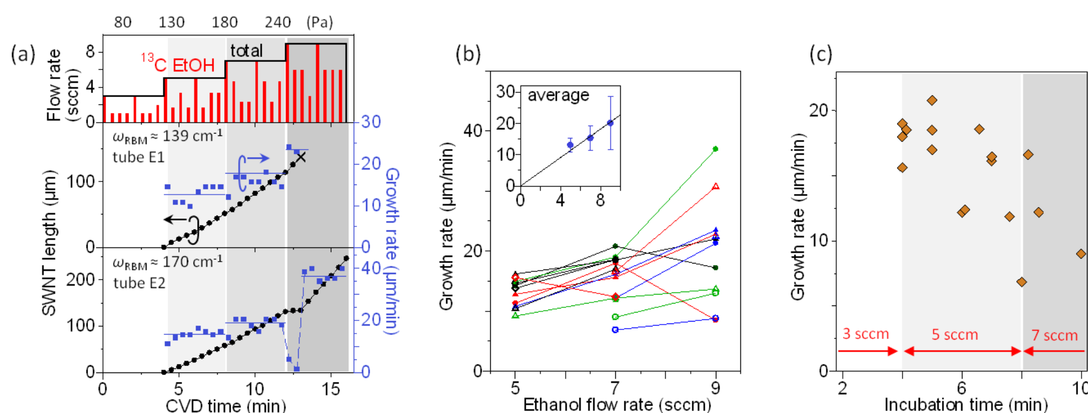

Figure 2.14 (a) ^{13}C ethanol flow rate (red bars) and total flow rate (black line) with 3-bits digital coding (top). Ethanol partial pressure was almost in proportion with the ethanol flow rate in our CVD system. Time evolution of length (black) and growth rate (blue) of two representative SWNTs. (middle panel) SWNT growth was accelerated with increase of ethanol pressure. (bottom panel) Growth was interrupted when the flow rate increased from 7 sccm to 9 sccm, and then the growth rate drastically increased. (b) Growth rate of individual SWNTs as a function of flow rate. Inset: Average growth rate versus ethanol flow rate (~pressure). Error bars represent the standard deviation. (c) Growth rate (with an ethanol flow rate of 7 sccm) as a function of incubation time. SWNTs initiated the growth only after the ethanol flow rate was increased from 3 to 5 sccm.

2.3.4 Response to ethanol pressure change during CVD

As already demonstrated, the digital-coded isotope labeling can elucidate the time evolution of the single SWNT growth, not only the growth rate revealed by isotope labeling with a certain time-interval. To maximize this advantage, responses to the changes in growth conditions, such as pressure and temperature, were studied. Pressure of carbon feedstocks is another important parameter for the growth of SWNTs, and therefore has been chosen carefully to improve the quality and selectivity.[95] Some studies changed the pressure of carbon feedstocks during the CVD for probing SWNT growth dynamics.[88,96] Also, it is well known that the growth rate of CNTs has positive correlation (*e.g.* proportional relation) with the pressure of carbon feedstocks.[82,87,97] However, such investigations were usually done in a statistical manner for bulk samples.

In this experiment, ethanol flow rate was elevated step-by-step from 3 to 9 sccm during CVD, while keeping other conditions constant, such as temperature, the flow rate of Ar/H_2 buffer gas (50 sccm), and the extent of vacuum pumping (top panel of Figure 2.14(a)). Thus the ethanol partial pressure is proportional to the flow rate.

Thirty-two ^{13}C isotope labels were incorporated in SWNTs with 30 s interval. Figure 2.14(a) shows growth curves for a typical SWNT (tube E1, middle panel) and an SWNT (tube E2, bottom panel) with unusual behavior. The growth was accelerated in tune with the increased ethanol pressure. This kind of response to the pressure change was observed for many SWNTs, in good accordance with other studies on bulk SWNTs.[82,87]

Figure 2.14(b) shows the growth rate of 18 individual SWNTs at each growth stage. Trend of the growth rate with 5 sccm and 7 sccm ethanol was similar, but the growth rate of each SWNT is not always proportional to the flow rate. Interestingly, the growth rate of some SWNTs had a negative relation between the pressure of carbon feedstocks and growth rate. Similar relation was slightly found in bulk SWNT samples.[82,87] This result suggests that each SWNT has a different sweet spot of growth conditions. Nevertheless, the average of all SWNTs was proportional to the ethanol flow rate (inset of Figure 2.14(b)).

In Figure 2.14(c), the growth rate with 7 sccm ethanol supply is plotted against the incubation time. No SWNT was nucleated with the supply of 3 sccm ethanol

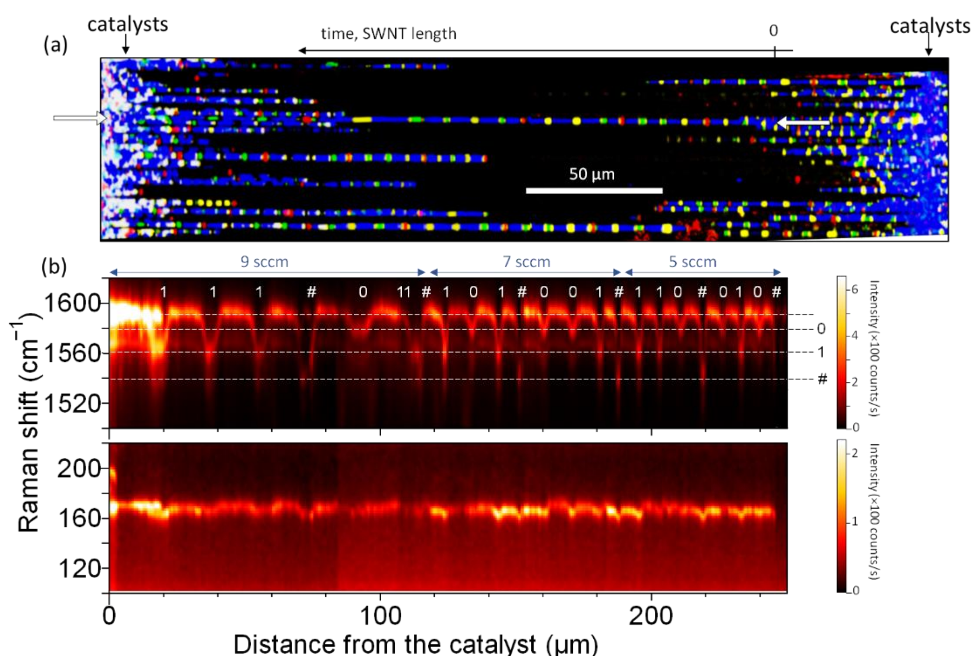

Figure 2.15 (a) Raman mapping image of SWNT arrays grown from elevated ethanol flow (Figure 2.14). (b) Raman spectra along the SWNT between white arrows in (a). This SWNT is referred to as "tube E2" in Figure 2.14.

among 18 SWNTs studied here, and some SWNTs initiated the growth when the ethanol flow rate was increased to 5 sccm. In contrast, when the initial flow rate of ethanol was 5 sccm (Figure 2.8), many SWNTs started the growth within a few minutes. This suggests the presence of threshold pressure for the nucleation of SWNTs.[96] Similarly to the result in Figure 2.8, a trend of slower growth rate was observed for the SWNTs with longer incubation time.

Interestingly, some SWNTs temporally stopped the elongation for 1–2 min in timing with the flow rate increment, but then restarted the growth and changed the growth rate drastically as shown in the bottom panel of Figure 2.14(a) (tube E2). Raman mapping image (Figure 2.15(b)) and Raman intensity map along the SWNT clearly shows that the SWNT is very likely a single nanotube. The significantly increased growth rate after 12 min (from 19 to 37 μm/min) suggests a change in a growth mode, though the chirality kept the same all along the tube. Further experiments and discussion are needed to understand the suspension and restart of the SWNT growth that is induced by a sudden pressure change.

2.3.5 Temperature-dependent growth along an individual SWNTs

In addition to the pressure of carbon feedstocks, the temperature of a reaction chamber is another important parameter for the growth of SWNTs. Many experiments changed the growth temperature and compared the obtained SWNTs, and some studied the effect of temperature change on individual SWNTs during CVD.[98] Since this technique has relatively high time-resolution and can monitor the growth evolution of long SWNTs individually, temperature dependence of the growth of variety of SWNTs can be investigated in details by varying the temperature during a CVD process.

In this experiment, the ethanol flow rate was kept constant (5 sccm, corresponding to partial pressure of ~130 Pa)). CVD synthesis of SWNTs started at 750°C, and then the set temperature was changed to 800, 850, and 800°C at t = 6, 12, and 18 min. Response of the temperature was not so quick as shown in the top of Figure 2.16(a) due to the large heat capacitance of the electronic furnaces. Representative growth evolutions are plotted in Figure 2.16(a). This clearly shows that the growth rate γ

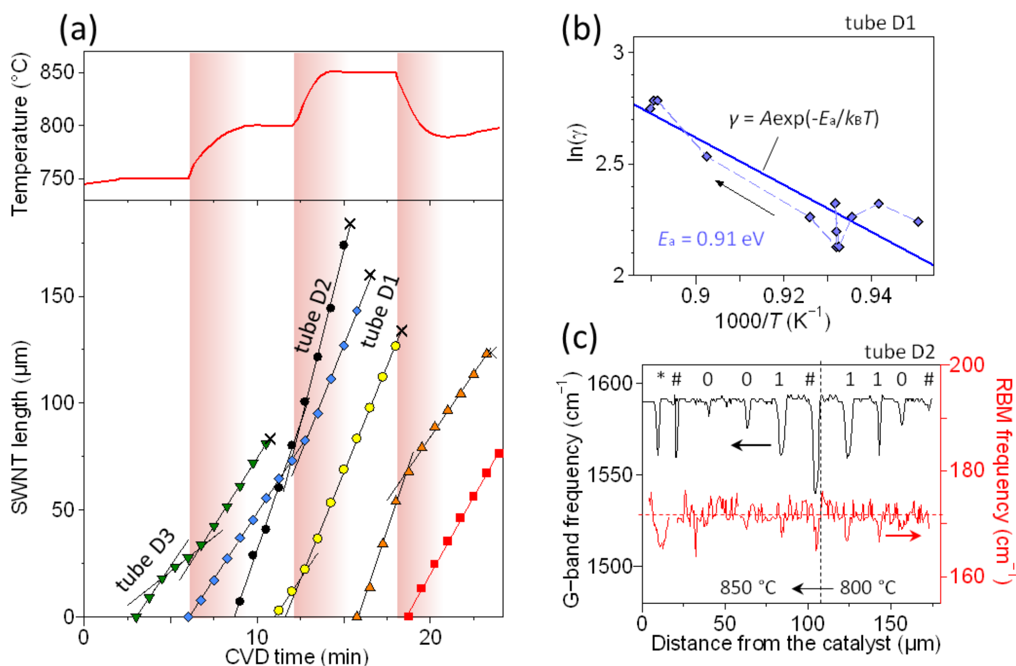

Figure 2.16 (a) Evolution of SWNT lengths grown at varied temperature (red line, right axis) with t_{CVD} = 24 min.(b) Arrhenius plots of the temperature-dependent growth rate generated from an individual SWNT (tube D1: blue diamonds) in (a). Activation energy of the growth of these particular SWNTs were 0.91 eV. Each plot corresponds to a growth rate recorded every 45 s. (c) G-band and RBM frequency along the SWNT (tube D2) plotted in black circles in (a). No change of chirality was observed. The peak position especially of RBM was noisy due to weak resonance. G-band down shift marked by a star near the catalyst originates from another short SWNT.

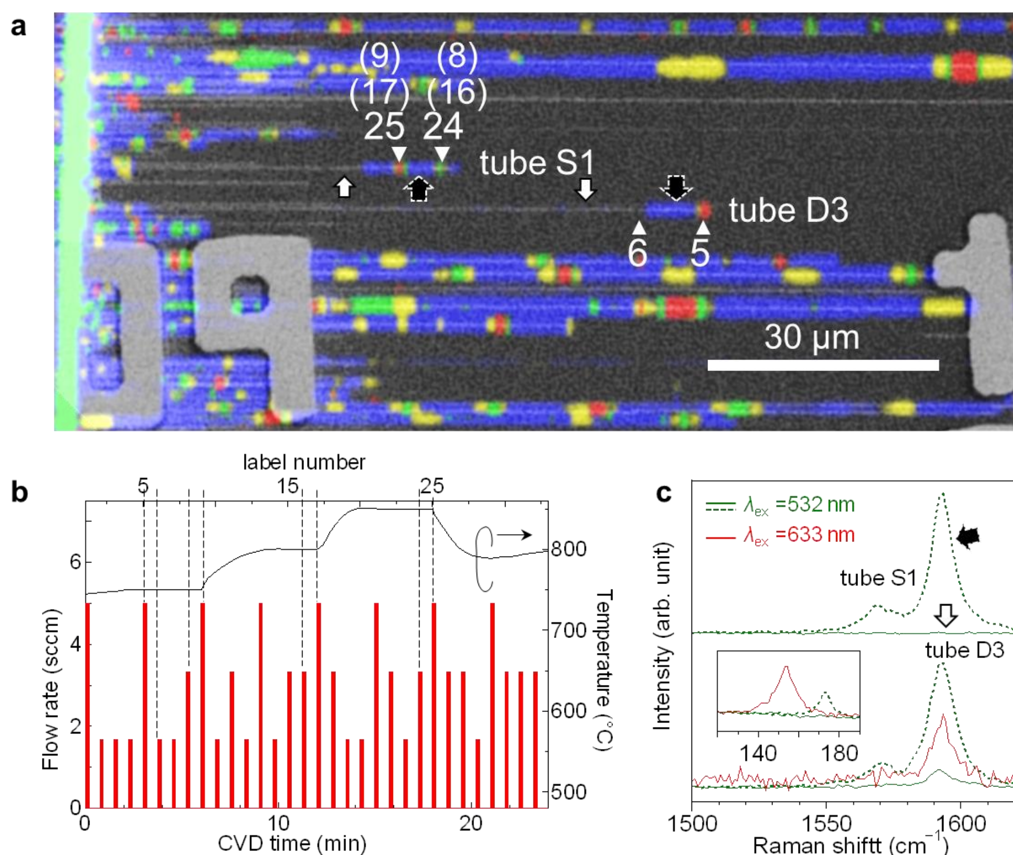

Figure 2.17 (a) Overlapped image of SEM and Raman mapping for the growth with modulated temperature (shown in Figure *). White numbers represent the label number, and those in brackets are other candidates. (b) Transition of the flow rate of ^{13}C ethanol and CVD temperature. (c) Raman spectra of two SWNTs that seem to have intramolecular junctions. Excitation energy is 2.33 eV (532 nm).

increased/decreased as the temperature increased/decreased for all the SWNTs. This agrees well with the experiments for bulk SWNTs. By labeling on individual SWNTs, temperature dependence can be traced along an SWNT without considering the difference in catalyst size/composition. For example, Figure 2.16(b) shows an Arrhenius plot of growth rate γ obtained from a single SWNT marked by blue diamonds in Figure 2.16(a). Each plot corresponds to the growth rate recorded every 45 s at different temperature. The Arrhenius plot yields the activation energy (= 0.91 eV) of the rate-limiting process for the growth of this particular SWNT. This value and the activation energy calculated from another SWNT (1.23 eV, orange triangle in Figure 2.16(a)) is close to that of carbon bulk diffusion in a Fe catalyst.[99]

This method of isotope labeling on individual SWNTs offers a chance to see differences among numerous SWNTs that grew under the exact same condition but in a different way. By identifying the rate-limiting process of each SWNT, the keys that determine growth rates, lifetime, and even chirality might be investigated in detail.

2.4 Direct growth of aligned SWNTs on TEM grids

In this section, a new approache for the observation of aligned SWNTs by TEM is described. Normally, the aligned SWNT arrays are grown on single-crystalline substrates, such as quartz or sapphire, and thus the TEM observation of the SWNTs requires transfer onto TEM grid. During the transfer process, the alignment, the catalysts, and the interaction between SWNTs and the crystalline surface tend to be lost. Therefore, it is difficult to directly investigate the origin of SWNT alignment in an atomic scale. Also, the SWNT grown from same type of catalysts on amorphous and crystalline substrates shows different behaviors, not only about the alignment. Interaction between catalysts and crystalline substrates needs to be explored; otherwise controlled growth on amorphous substrates (*e.g.* SiO_2/Si) does not always work on quartz or sapphire.

2.4.1 Aligned growth on NaCl-induced cristobalite substrates

In most case, single-crystalline substrates, such as quartz or sapphire, were used to get lattice-oriented aligned SWNTs because such substrates are easy to prepare and the SWNT orientation can be restricted to one or a few in a whole area. Although mechanisms of the alignment on those substrates were discussed from several aspects; alignment of SWNTs along atomic steps, van der Waals interactions between SWNTs and the surface of crystalline substrates, no experimental evidence from crystal structures was presented. Furthermore, the effect of crystallinity of the substrates on catalyst formation has not been discussed, especially of an atomic scale.

A recently proposed in-plane TEM technique, where ultrathin SiO_2 membrane serves as a support for SWNT growth and a TEM grid at the same time, enables direct observation of SWNTs and catalysts without any transfer processes. As the SiO_2 membrane is chemically the same as frequently used Si/SiO_2 substrates, which is much different from conventional carbon membrane in TEM grids, the growth on normal substrates can be directly reproduced on TEM grids. Here, Si substrates with thin oxide layers are used to make in-plane TEM grids. The grids are fabricated by partially removing the Si on the back side with wet/dry etching and leaving thin SiO_2 suspended. Since morphology and population of SWNTs remains unchanged, this technique is highly suitable for the observation of horizontally aligned SWNTs grown on quartz or

sapphire substrates. However, it has been difficult to prepare a crystalline membrane thin enough for a high resolution TEM observation, so the morphology and even catalysts were lost when the SWNT arrays were transferred onto in-plane TEM girds. One approach for the direct observation of crystalline substrates, SWNTs, and catalysts with TEM is start the fabrication of in-plane TEM grids from thin crystalline SiO_2 layers on top of Si substrates. This can be made possible by crystallizing the oxide layer with some sort of annealing methods.

Alkali impurities, such as sodium and potassium, in SiO_2 are known to catalyze the formation of cristobalite and significantly reduce the temperature for the crystallization. Alkali ions weaken the Si-O network and lower the viscosity through the formation of bonds to the network. In a previous study in 2009, cristobalites formed on SiO_2/Si substrates by the introduction of NaCl were used for the growth of radially aligned SWNTs.[100] Although it was not suitable for device application because the

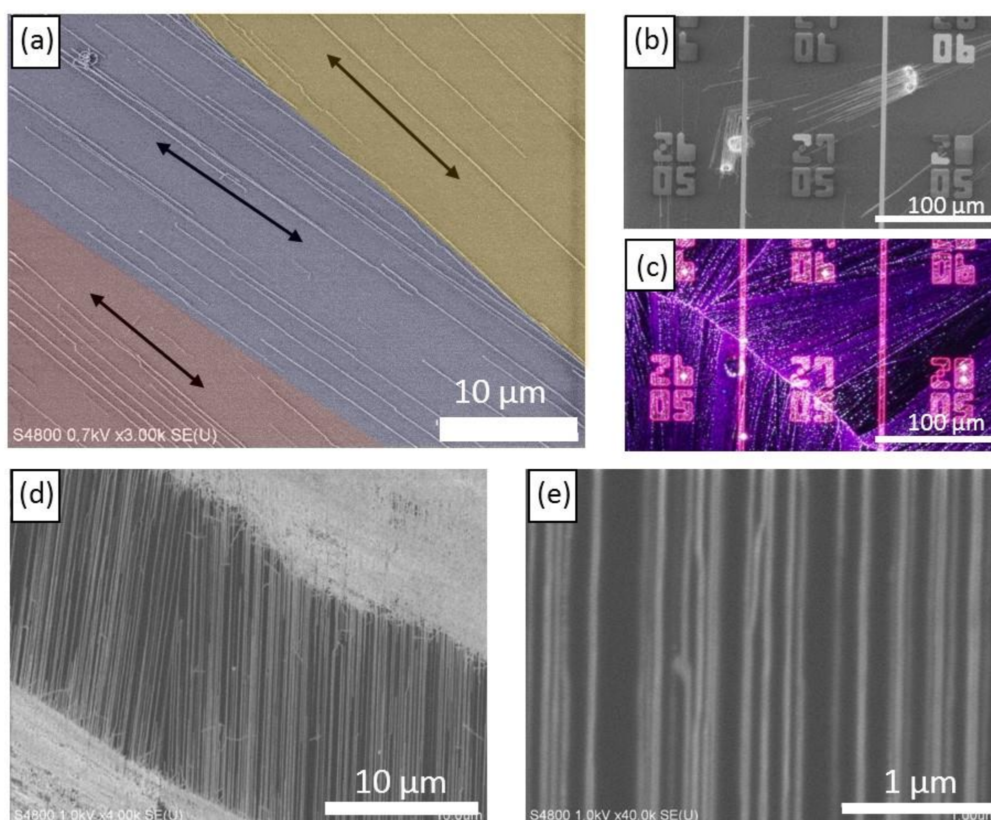

Figure 2.18 (a) Horizontally aligned SWNTs grown on multi-domain cristobalite. (b,c) SEM and dark-field optical images of cristobalite substrates with metallic markers. (d) High-density SWTN arrays on cristobalite with slightly different orientations grown from isolated catalyst region (white parts). (e) High-magnification SEM image in (d).

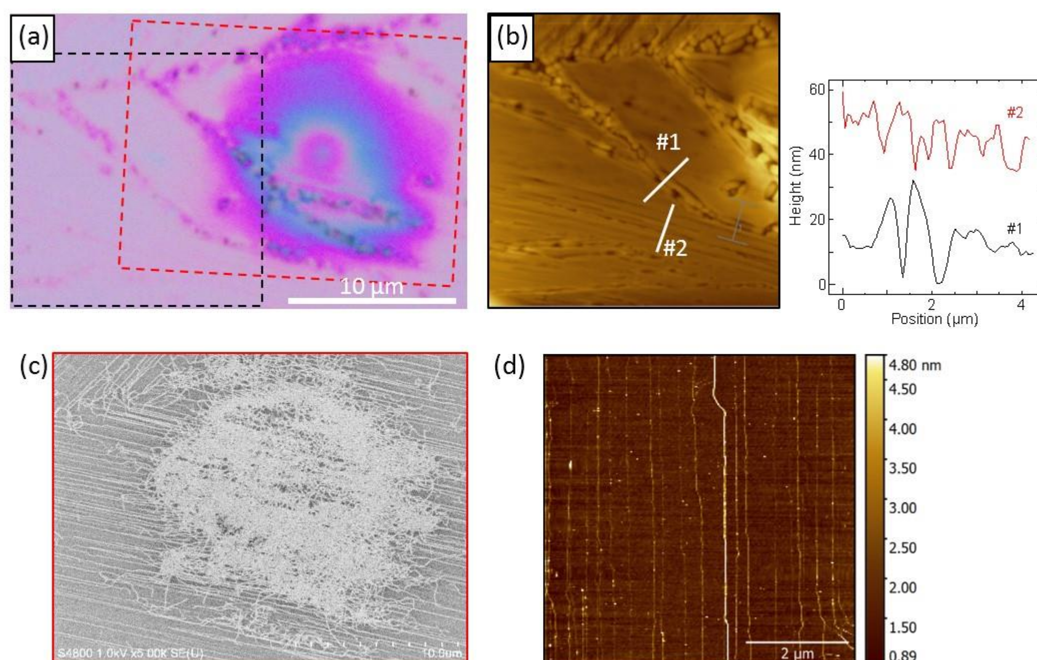

Figure 2.19 (a) Bright-field optical of the cristobalite surface. (b) AFM image measured in the black square in (a) and cross-section profiles. (c) SEM image and (d) AFM image of the SWNTs transferred on normal SiO_2/Si substrates.

orientation cannot be narrowed down to one, it can be used for the fabrication of thin layers of (poly)crystal for TEM observation as mentioned above.

In this study, NaCl aqueous (0.15 mol/L) was used for crystallization of amorphous SiO2 and Si substrates. Small amount of NaCl was loaded on SiO2/Si substrates the dip-coating method. After drying in air, the substrates were annealed at 900°C for 12 h in air, followed by spin-coating $FeCl_3$ solution (0.05 mmol/L in ethanol) as a catalyst precursor. The substrates were baked at 750°C for 5 min in air to oxidize the catalysts. Figure 2.12 shows horizontally aligned SWNTs grown on cristobalite. Since the obtained cristobalite was poly-crystalline, orientation of the SWNTs in Figure 2.18(a) can be categorized into three directions as colored by red, blue, and yellow. The cristobalite grown in air had a large surface roughness which can be easily observed by dark-field optical microscopy as shown in Figure 2.18(c). Numbers and vertical lines are photolithographically patterned Au markers. SWNTs in Figure 2.18(b) have a similar orientation to the surface tranches, which may be the interfaces of cristobalite domains.

When isolated catalysts were pattered on the cristobalite, for instance from the scratches with iron tweezers, the density and the degree of alignment were increased to the similar level to that on single-crystal quartz substrates (Figure 2.18(d)), and the density was as high as >12 SWNTs/μm (locally >20 SWNTs/μm) in Figure 2.18(e). The length of long and aligned SWNTs found on cristobalite was 160 μm, indicating that the cristobalite can be a proper platform for the growth of isotope-labeled SWNTs.

Although the formed cristobalite had a large roughness observable by optical microscopy (Figure 2.19(a)), it does not mean that is the origin of alignment. Figure 2.19(b) shows an AFM image of the cristobalite measured in the area outlined with a dashed black box in Figure 2.19(a). Some trenches were as deep as ~15 nm and optically observable; however the SWNTs grew aligned on most of the region (Figure 2.19(c)) even where no surface trenches were found. Another AFM image was taken after the SWNT arrays were transferred onto very flat SiO_2/Si substrates (as-purchased) as shown in Figure 2.19(d). The degree of alignment is comparable to the SWNTs grown on single-crystal quartz substrates, though the alignment is always degraded during the transfer process.

2.4.2 In-plane TEM grids from Si with cristobalite layer

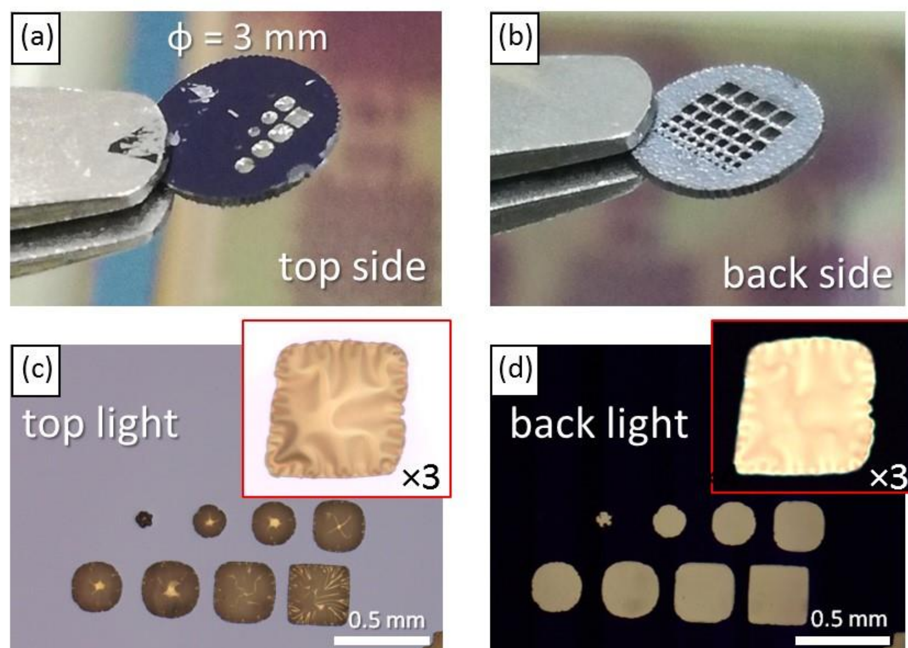

Figure 2.20 (a,b) Photograph of a fabricated TEM grid from (a) top side and (b) back side. (c,d) Bright/dark-field microscope images the TEM grid.

TEM grids with ultrathin SiO_2 layers for in-plane observation are commercially available. Those grids are fabricated by normal dry/wet etching of SiO_2/Si substrates. This process is compatible with the cristobalite substrates described above. As a first step, the fabrication of normal TEM grids with amorphous SiO_2 were tested as shown in Figure 2.20. Photoresists were patterned on the back side of Si waters with 100 nm oxide layers, and then dry etching was performed on the back side. An example of the fabricated TEM grid is shown in Figure 2.20 (a) and (b). Since the etching rate depends on the hole size and position in the etching chamber, the full-depth of Si was etched through only near the wafer edge and for large holes.

Chapter 3:

Upscalable on-Chip Sorting of s-SWNT Arrays

3.1 Introduction to SWNT sorting

3.1.1 Liquid-phase separation methods of s-SWNTs

Since SWNTs can be dispersed in water once wrapped by surfactants, liquid-phase separation is a promising and scalable approach for the preparation of s-SWNT films for semiconductor applications. First liquid-phase separation of semiconducting and metallic SWNTs was reported in 2003,[101] taking advantage of the difference of the relative dielectric constants. A number of further developments followed this, such as sorting SWNTs by diameter, bandgap and electronic type using density gradient ultracentrifugation (DGU),[41] DNA-[42] or polymer-wrapping,[43] gel-chromatography,[44] and aqueous two-phase separation.[102] All those separation methods are based on the differences of chemical/physical adsorption of wrapping materials and SWNTs. Since assembly into aligned arrays is done after the sorting, the purity can be improved by multiple-cycle of separation, though the total amount of target-type of SWNTs (*e.g.* s-SWNTs) is sacrificed. Recent studies that purified s-SWNTs with the purity up to 99.99% demonstrated high-performance transistors that outperformed silicon-based metal-oxide-semiconductor technologies by assembling s-SWNTs into high-density arrays.[103] Despite the scalability and controllability of density and chirality, one challenge for this approach is the lower degree of alignment of post-sorting assembly techniques[39,40,104–106] than lattice-oriented growth.[55] Crossed s-SWNTs have smaller charge density due to the inter-SWNT screening, leading to weaker gate-channel coupling especially for scaled devices.[37]

3.1.2 Growth-phase sorting methods of s-SWNTs

The growth-phase sorting, in other words, selective growth of s-SWNTs or even chirality-specific growth has been intensively studied for long. This approaches would be preferable in terms of cleanliness of SWNTs because no additional treatment is necessary. Also, the selective growth can be directly combined with lattice-oriented aligned growth on crystalline substrates. Origin of selective growth is divided roughly into two categories. One approach is to selectively etch m-SWNTs based on the difference of electronic structures, while growing s-SWNTs more efficiently than the etching process.[107] The other approaches is to match the atomic arrangements of SWNT edges with atomic lattice structures of catalysts by using solid (alloy or carbide) catalysts.[59,108]

However, due to a relatively subtle difference of geometries and formation energy at nanotube/catalyst interfaces among a number of possible chiralities, the purity of s-SWNTs realized by those selective growth methods is not sufficient for logic applications (>99.9999%).[54] Therefore, post-growth purification processes are necessary to push it up to the required level.

3.1.3 On-substrate purification methods

To exploit the excellent morphologies of the lattice oriented growth and the selective growth of semiconducting or specific-chirality SWNTs, on-substrate purification is one of the best approaches to obtain s-SWNT arrays over a large area.

One straightforward strategy is to chemically etch m-SWNTs by exploiting the difference of chemical reactivity, while keeping s-SWNTs relatively intact.[109,110] Since those chemical etching can be uniformly applied over a large-area, the purification process can be easily scaled up. Chemical reactivity of SWNTs, however, highly depends on diameter (curvature of walls) , not only on the metallicity (metallic or semiconducting).[111] Also, s-SWNTs are damaged due to the subtle difference of the reactivity, and small segments of m-SWNTs often remain after the etching process, making it difficult to fabricate short-channel devices.

The difference of electronic structures between m- and s-SWNTs appears in interaction with light (photons), *i.e.* light absorption.[112] Since optical transition energies are uniquely determined by chirality, choice of appropriate wavelengths

enables diameter- or metallicity-selective oxidation without physical contact to SWNTs. It requires a quite strong light source, but the selectivity appears only when the diameter of SWNTs are narrow. Similar to this, metallicity of SWNTs can be recognized by the difference of dielectric constant, and thus m- and s-SWNTs possess different response to microwave. This enables preferential heating of m-SWNTs,[113] though the selectivity of the heating is not sufficient. Other simple and upscalabe approaches are to peel-off or wash-off either type of SWNTs *via* scotch tapes or surfactants by exploiting the difference of chemical/physical adhesion [114,115]. Similar to other approaches described above, the selectivity needs to be much improved to achieve the required purity of s-SWNTs (99.9999%). Although multiple sorting processes might increase the purity, it will also significantly deteriorate the density of SWNTs of interest (*e.g.* s-SWNTs).

As is clear from the large on-off current ratio (~10^6) of s-SWNT transistors, the off-state current, which is proportional to Joule self-heating, of s-SWNTs and m-SWNTs is different by several orders of magnitudes for parallel channel configurations. Therefore, applying a large bias across SWNTs while s-SWNTs are turned-off by gate leads to highly selective heat-induced oxidation of m-SWNTs (electrical breakdown).[116] Compatibility with high-density arrays (>100 SWNTs/µm) makes this method a suitable tool for the fabrication of high-performance transistors [117,118]. One of the drawbacks is the difficulty in large-scale fabrication because only local portions (~100 nm) of m-SWNTs are removed and therefore one-by-one voltage application is required for a number of electrode pairs. To overcome this problem, electrical breakdown using comb-shaped temporal electrodes has been successfully demonstrated for chip-scale circuit fabrication [119,120]. However, electrical breakdown of ultrascaled devices faces degradation of the on-current retention because an extremely strong field is required to cut the m-SWNTs due to strong heat-sinking to the metal contacts [121,122].

Another type of m-SWNT removal based on Joule self-heating is reported, in which SWNT arrays embedded in organic resists are subjected to bias voltage along the axis.[123,124] Selective Joule heating in m-SWNTs opens up the organic films in the vicinity, followed by reactive ion etching of the exposed m-SWNTs over a long-length. It is further extended from direct current injection to microwave absorption

amplified by microstrip dipole antennas [125] and mid-infrared light absorption [126] towards larger-area and simpler purification processes. However, relatively large widths of trenches formed through thermocapillary flows in the organic resists (hundreds of nanometers) limits the scaling to ultrasmall inter-SWNT spacing (<10 nm) for the array density of >100 SWNTs/μm.

The objective of this chapter is to develop a new approach for the sorting of the s-SWNT arrays. As described in Chapter 2, horizontal SWNT arrays on quartz substrates are an ideal structure to start with for high-performance transistors and their integration into large-scale circuits. Such applications require ultra-selective removal of m-SWNTs while preserving all s-SWNTs during post-growth purification on substrates. One target of the purity of s-SWNTs for logic application is >99.9999%. Also, this selectivity has to hold when the SWNTs are densely packed and the inter-tube distance is small (compatibility to high-density SWNT arrays). As the target density is ~125 SWNTs/μm [54] or even ~250 SWNTs/μm,[53] the SWNTs that are placed ~8 nm away from the m-SWNTs destroyed have to be intact. Furthermore, the wafer-scale purification is desired.

3.2 Long-length burning of m-SWNTs on substrates

3.2.1 Self-sustained burning of m-SWNTs

Joule self-heating of SWNTs can be a promising tool to achieve ultrahigh selectivity for purification processes because the difference of off-state conductance between s- and m-SWNTs is what makes them desirable and undesirable in transistor channels, respectively. Since the electrical breakdown method has demonstrated excellent selectivity [118] even when the density of SWNT arrays reached ~100 SWNTs/μm,[117] full-length removal of m-SWNTs based on electrical breakdown could provide us with one of the best solutions for this goal.

Previously we showed that the film coating of polymer or other organic molecules on SWNT arrays occasionally induced the burning over more than several micron,[128] in contrast to conventional electrical breakdown, whereby only ~100 nm gaps are created. That opened a new, but primitive way for the large-area purification of s-SWNT arrays; however the organic film-assisted burning was not so reproducible

and sometimes did not give any difference from the conventional method in spite of the same parameters. Also, even when the burning was successfully enhanced, the length of removed parts of SWNTs (removed length) varies from sub-micron to more than 10 µm. Roughness of substrate surface, chemical functionalization of SWNT walls, temperature of substrates, and partial pressure of oxygen were previously tuned to achieve reproducible and improved burning of SWNTs. However, no significant improvement was obtained.

To go straight to the bottom line, the dependence of SWNT burning on the ambient gas conditions, especially on water vapor, was investigated. Here, the Joule heating-induced burning was initiated by application of a ramp voltage along the tube axis. Two types of gas conditions were used for the burning of SWNTs embedded in PMMA thin films. 1) dry oxygen gas, and 2) oxygen gas saturated with water vapor at room temperature (wet oxygen). The former and latter are referred to as dry polymer-assisted (DPA), and water- and polymer-assisted (WPA) conditions, respectively. For both conditions, the total pressure was ~90 kPa.

Figures 3.1(a) and (b) show SEM images before and after voltage application (up to 60 V) to the array of 10-µm-long SWNTs under the DPA condition, respectively. Lengths of the removed parts of the SWNTs remained very small (~160 nm on average), even with the assistance of PMMA coating, as shown in Figure 3.1(c). This

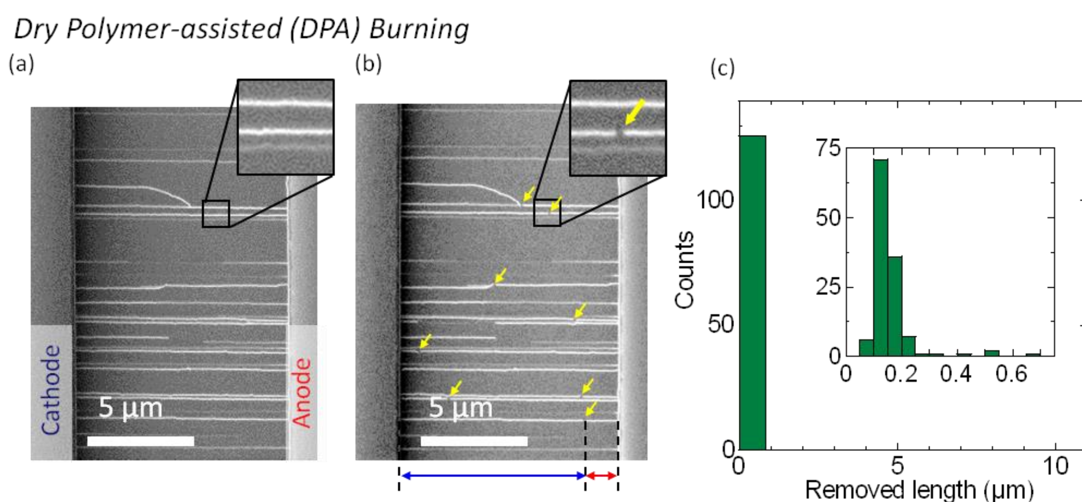

Figure 3.1 (a,b) Typical SEM images of SWNT arrays before (a) and after (b) breakdown under the DPA condition. Arrows denote the breakdown position. (c) Distributions of the removed length. Adapted with permission from ref. [127].Copyright 2017 Springer.

value is almost the same as that obtained by conventional electrical breakdown [116] without organic film coating, This clearly indicates that the self-sustained burning of SWNTs cannot be realized only under pure oxygen environment with PMMA coating. Note that the location of breakdown was widely distributed in the 10-μm channels in these experiments, while in a previous study on in-air breakdown of shorter-channel transistors, the majority of SWNTs were cut near the middle due to thermal dissipation to the metal contacts.[129] The breakdown position in the present study was probably influenced by randomly occurring defects or buckling of SWNTs [130] which were frequently derived from the synthesis and transfer processes.

Figures 3.2(a–c) show typical SEM images before and after the voltage application to the array of 10-μm-long SWNTs under the WPA condition, and the distribution of the burning length. The average burning length was significantly increased to ~5.5 μm just *via* the introduction of saturated water vapor, which accounts for 53.7% of the total original length (10.3 μm). This indicates that water vapor plays a significant role in propagating the burning of SWNTs. The limited reproducibility of the burning length in the previous study, which was [128] conducted in air with PMMA coating, can be explained by a strong dependence on the ambient humidity. Moreover, the removed length of SWNTs was decreased when the substrates were heated during voltage application treatment.[131] This suggests that water molecules

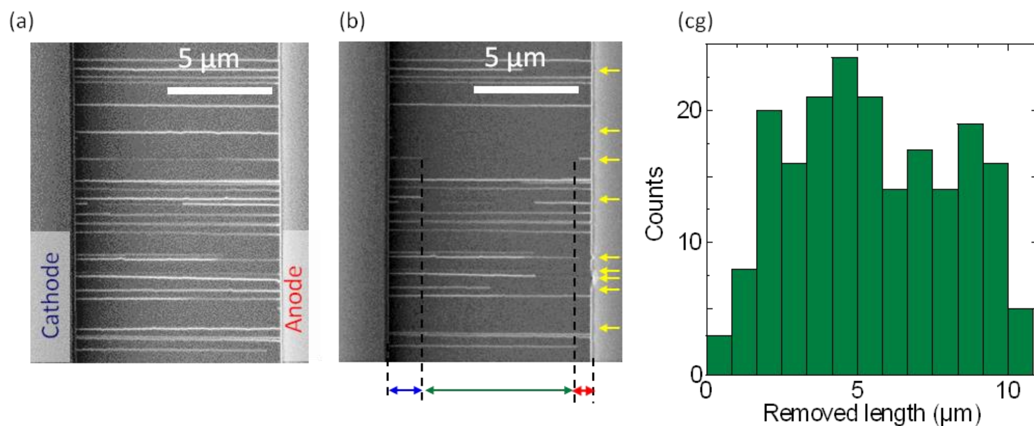

Figure 3.2 (a,b) Typical SEM images of SWNT arrays (a) before and (b) after burning. Arrows denote the burned SWNTs. (c) Distributions of the removed length of SWNTs treated under the WPA condition. Adapted with permission from ref. [127].Copyright 2017 Springer.

adsorbed on the SWNT surfaces,[132] rather than those in gas phase, are critical for the self-sustained burning of SWNTs.

Note that the long-length removal of m-SWNTs benefits a single FET, as well as large-scale fabrication of microelectronic devices, from two points of view. For example, if the m-SWNTs are fully eliminated from the channels, total gate-to-channel capacitance and thus the switching delay of circuits will be reduced.[133] Also, the formation of m-SWNT nanogaps will localize and amplify the electric field in the vicinity, and should be avoided because it could lead to unintentional tunneling or

3.2.2 One-way burning from random breaking points

Although the burning length was considerably increased with the combination of water vapor exposure and PMMA coating, it still had a wide distribution from sub-micron to their full-length (~10 μm). To understand the origin of the large variation, focus was then directed on the length of the remaining m-SWNTs on both the cathode (left in the SEM images) and anode (right) sides. Figures 3.3(a) and (b) show histograms of the remaining SWNT lengths after DPA breakdown and WPA burning, respectively. Interestingly, the remaining SWNTs on the cathode side (top panel) had similar length distributions for both conditions, while the other side (bottom panel) possessed totally different features. The remaining SWNT length on the anode side after the DPA breakdown was as widely distributed as that on the other side. In contrast,

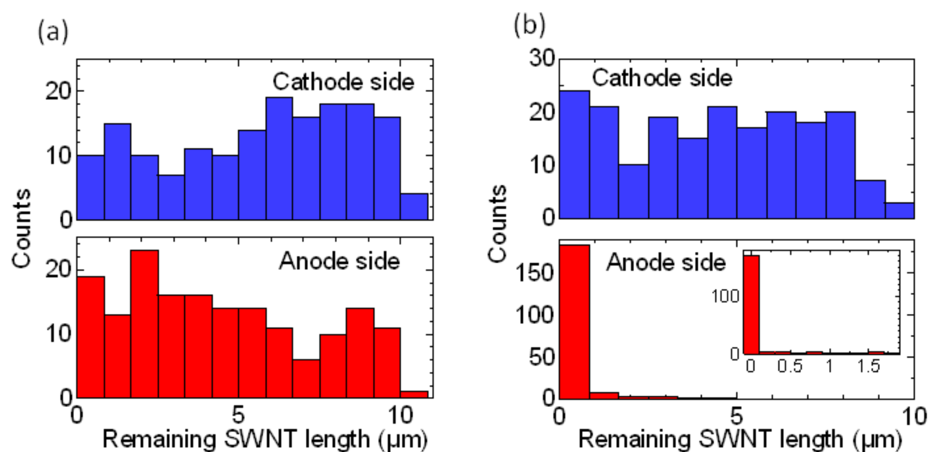

Figure 3.3 Distributions of the length of SWNTs remaining at both the cathode and anode sides (top and bottom, respectively) for (a) the DPA burning and (b) WPA burning. Adapted with permission from ref. [127]. Copyright 2017 Springer.

most of the remaining SWNTs on the anode side after WPA burning were <100 nm, and the majority of the SWNTs on the anode side (>80%) were completely burned. These facts imply that SWNTs were very likely to burn only on the anode side (one-way burning) from the breakdown position, where oxidation of the SWNTs first took place.

3.2.3 Evaluation of purified SWNT arrays from device performance

Before going further to the mechanism of the SWNT burning, the effectiveness of the WPA burning over the conventional electrical breakdown was simply evaluated through the fabrication of two FETs after the purification process; a very first step to upscaling of the purification. The original FETs are defined according to the first electrodes used, *i.e*. those with SWNTs before and after burning, are denoted as FETs A (Figure 3.1(a) and Figure 3.2(a)), and A' (Figure 3.1(b) and Figure 3.2(b)), respectively. After WPA burning or DPA breakdown of the m-SWNTs, second electrodes were placed between the original source and drain (initial anode and cathode), as illustrated in Figure 3.3. The two newly defined FETs on the cathode and anode sides are denoted as FETs B and C, respectively.

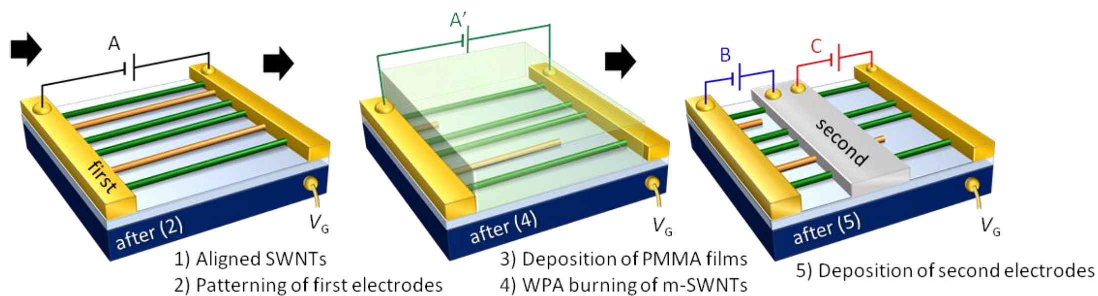

Figure 3.4 (a) Schematics of the fabrication of multiple FETs after a WPA burning process. Two FETs were newly defined by the deposition of an extra gold electrode between the original source and drain contacts, after WPA burning of the m-SWNTs. Adapted with permission from ref. [127]. Copyright 2017 Springer.

Figure 3.4(a) shows an SEM image of FETs B (left) and C (right) fabricated from the identical SWNT array shown in Figure 3.2(b). The on/off current ratios of the FETs A, A', B and C are plotted for both WPA burning and DPA breakdown in Figure 3.5(d). The FETs A always showed on/off ratios of <10, which indicates the coexistence of both m- and s- SWNTs in the original channels (typically contain of ~30 SWNTs). The FETs A' after both WPA burning and DPA breakdown showed on/off current ratios in the range of 10^3–10^6. This in turn indicates that all the m-SWNTs were broken down. Importantly, the FETs C at the anode side after WPA burning had on/off ratios almost as high as the FETs A' because the m-SWNTs that remained at the anode side were very short. In contrast, the FETs B on the cathode side showed low on/off ratios due to the short circuit caused by the m-SWNT impurities that remained on the cathode side. This result is agree well with the SEM observation shown in Figure 3.2. The

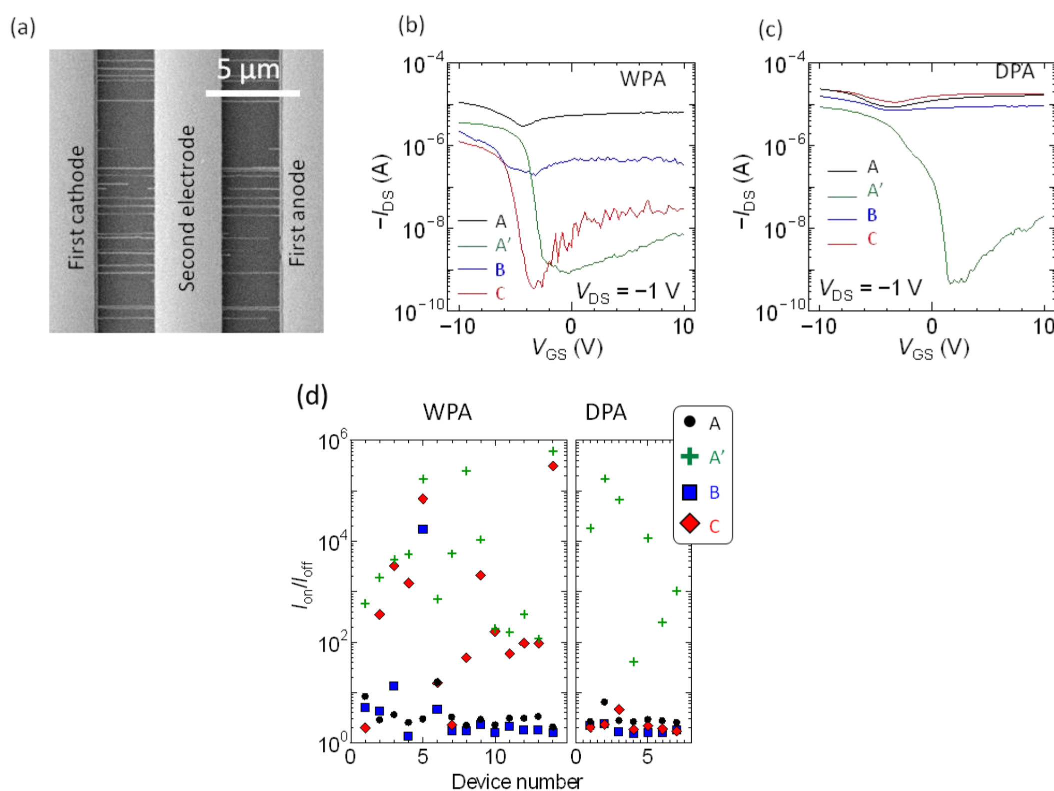

Figure 3.5 (a) SEM image of redefined FETs. Left (cathode side) and right (anode side) FETs are denoted as B and C, respectively (b,c) Typical transfer characteristics for the four types of FETs subjected to (b) WPA burning and (c) DPA breakdown. $V_{DS} = -1$ V. (d) On/off ratios of FETs A, A', B, and C for WPA burning (left). Similar data for DPA breakdown are plotted on the right for comparison. Adapted with permission from ref. [127]. Copyright 2017 Springer.

device performance confirmed that the long length of the m-SWNTs was indeed removed by the WPA burning process. In addition, Raman spectroscopy, optical microscopy with crossed polarizers,[135] and atomic force microscopy (AFM) measurements supported the selective and long-length removal of m-SWNTs by the WPA burning process. In contrast, for DPA breakdown, whereby the remaining SWNT length on both the cathode and anode sides was quite long, the FETs B and C had on/off ratios of less than 10. Conventional electrical breakdown is thus not suitable for the fabrication of multiple transistors, unless shapes of electrodes for breakdown is optimized.

Figures 3.5(b) and (c) show transfer characteristics of the FETs A (black), A' (green), B (blue), and C (red) after the WPA burning and DPA breakdown processes, respectively. The on-state current was decreased by 75 ± 19% after WPA burning, while that after DPA breakdown was 79 ± 23%. This indicates that additional water vapor did not deteriorate the selectivity in the electrical breakdown of m-SWNTs. It should be stressed that the reduction of on-state current after WPA burning is rougly comparable to that after Joule heating-induced thermocapillary flows and reactive ion etching,[123] where all s-SWNTs were considered to be preserved with the assumption of a typical ratio of population and conductance of s- and m-SWNTs. Under the similar assumption, the population-based purity of s-SWNTs was calculated to be ~99.8% for the WPA burning based on the performance of transistors. Further discussion on the damage to s-SWNTs will be discussed in Chapter 4

The fabrication of multiple FETs thus demonstrated the potential of WPA burning as a large-scale purification process; however, the burning length should be further improved to be employed in microelectronic applications, where the purity of s-SWNTs must be as high as 99.9999%. Uniformity of SWNT density and m-SWNT impurities is also required. The way to overcome the problem that originates from imperfect removal of m-SWNTs will be discussed in Chapter 4.

3.2.4 Discussion on the roles of water and polymer in the burning process

Here, a focus is directed back to the mechanism of WPA burning. A possible role of water molecules in the burning process is substantial enhancement of the oxidation

rate of both SWNTs and PMMA films through adsorption on the SWNTs. The addition of water vapor to the feed gases (typically oxygen) is generally increase the oxidation rate of carbon materials, such as graphite.[136] Water itself can also be used in hydrogen production through coal gasification.[137]

The interval time of oxygen collision with carbon atoms in SWNTs under the experimental conditions employed in this study (~90 kPa oxygen) is typically ~10^{-9} s. This is much larger than the thermal relaxation time (~10^{-10} s) [138] of an SWNT directly on a SiO_2 substrate. Furthermore, the reaction rate is even much smaller than the collision rate due to the activation barrier of reactions. Therefore, the oxidation induced by gas molecule collision is unlikely to result in a chain reaction of SWNT oxidation.

Instead, one proposal is that the adsorbed water acts as an oxidizer which significantly increases the oxidation rate of both SWNTs and PMMA because water molecules can be adsorbed on SWNT surfaces and readily involved in the reaction with SWNTs. Three is still unclear point about an energy balance before and after the reaction. Since the oxidation of SWNTs by water ($C(s) + H_2O(l) \rightarrow CO(g) + H_2(g)$) is an endothermic reaction, this reaction cannot be self-propagated. Chemical reaction products, such as CO and H_2, might generate heat by reaction with oxygen in the vicinity of the SWNTs. Water may thus contribute to the burning of SWNTs rather catalytically through multiple complicated reactions. Further studies are needed to elucidate the mechanism of water-assisted burning of SWNTs.

Dynamic changes of SWNT temperature and water molecules need to be also considered. When the SWNTs are broken down, and nanogaps are formed and quickly cooled down to room temperature, water molecules can be adsorbed/encapsulated [139] on/in the SWNTs. The bias voltage is still continuously applied after nanogap formation, so the amplified field at the nanogaps can induce the burning of SWNTs on the anode side. Although the temperature of the burning SWNT edge is very high, the hot region is localized near the reaction front. In addition, the velocity of SWNT burning should be greater than ~1000 m/s for the chain reaction to be self-sustained, according to the simulation (shown later in this chapter). Therefore, it is quite possible

that the adsorbed water molecules are involved in the reaction with SWNTs before they desorb from the SWNTs during the WPA burning.

The burning length of SWNTs was also measured in wet oxygen gas but without PMMA coating to evaluate the importance of the PMMA film.[127] The length of removed part of SWNTs was increased to 1.3 μm (from 0.3 μm) on average by the addition of water vapor, but this was still much smaller than that under the WPA condition. In addition, when polymer-assisted burning was performed in air with a relative humidity of <20%, the PMMA coating slightly increased the average removed length from 0.3 to 0.8 μm. Therefore, the combination of PMMA coating and high-pressure water vapor is inevitable for the full-length removal of m-SWNTs. It should be stressed that PMMA coating has another role to avoid the lateral etching, which is caused by the interconnection of SWNTs *via* the occasional formation of water droplets on the substrates under high humidity. Therefore, PMMA coating facilitates the high selectivity of electrical breakdown between s- and m-SWNTs in the presence of water vapor.

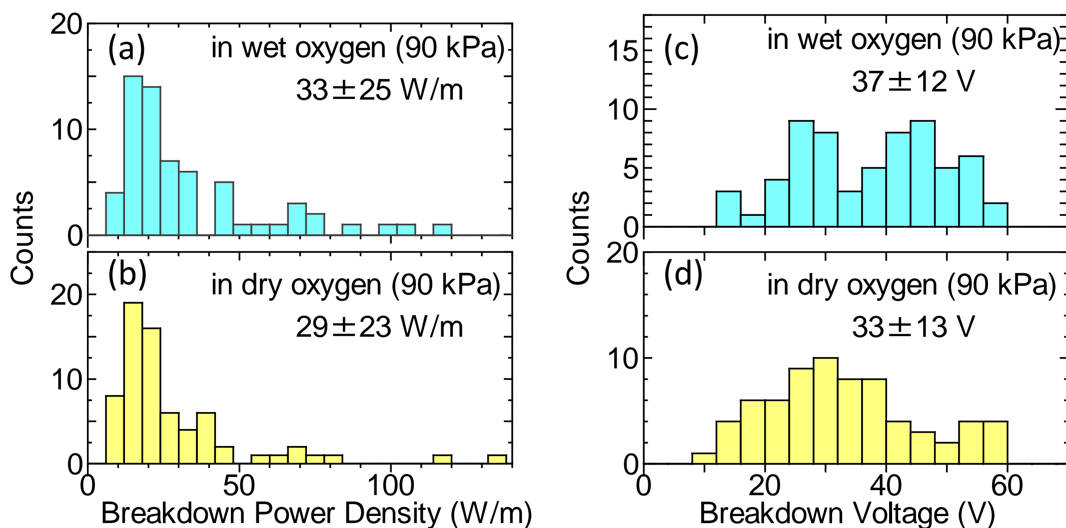

Figure 3.6 Distribution of breakdown power density (a, b) and breakdown voltage (c. d) in wet oxygen (a, c) or dry oxygen (b, d). Total pressure for both conditions is 90 kPa, and all the set up was kept at room temperature. SWNTs were embedded in PMMA films. Channel length was ~10 μm.

PMMA thin films (~26 nm thick) are unlikely to suppress the supply of oxygen to SWNTs. The power needed to break SWNTs was strongly dependent on the collision frequency of oxygen, which is proportional to the oxygen partial pressure.[127] On the other hand, the coating of SWNTs with PMMA did not significantly change the breakdown power (Figure 3.6), while thicker PMMA films (~500 nm) increased the breakdown power by >10%. This indicates that the thinner coating has less influence on gas diffusion in the vicinity of the SWNTs, and is likely to be beneficial to the self-sustainable burning of SWNTs.

In addition, PMMA coating on SWNTs was previously used as a passivation layer to reduce hysteresis in the transfer characteristics of FETs by the removal of water from the vicinity of the SWNTs.[140] In contrast, the PMMA-coated FETs in the present experiments were p-doped by exposure to the wet oxygen and exhibited a reduction of ambipolar features compared to that measured in a vacuum. Therefore, oxygen and water molecules are likely to easily penetrate through the PMMA thin films employed in this study.

3.2.5 One-way burning from random breaking points

3.2.6 Simulation study on burning SWNTs

To discuss the role of the polymer coating in the enhancement of SWNT burning in detail, numerical simulations of m-SWNT burning were modeled and then performed with a device configuration that represents the SWNT samples used in this study. Here, the theory of conventional combustion waves is adopted in a similar way to that in a previous study on the combustion of CNT-polymer composites.[141] For simplicity, only one-dimensional distribution of temperature (based on equation of heat conduction) and oxidation reaction (based on Arrhenius equation) was considered for both (1) an SWNT and (2) a 2-nm-thick polymer layer in the vicinity of the SWNT (hereafter referred to as the "inner PMMA"). Figures 3.7(a–c) show schematics of the SiO_2 substrate and the PMMA film other than the inner PMMA (denoted as "outer PMMA). The substrate and outer PMMA are kept at room temperature (T_0) because the temperature will not be increased significantly due to a large thermal boundary

resistance with SWNTs compared to its size. The total system can be described by the following equations:

$$\rho_1 c_1 A_1 \frac{\partial}{\partial t} T_1(x,t) = \kappa_1 A_1 \frac{\partial^2 T_1}{\partial x^2} + \frac{\rho_1 A_1 Q_1}{M_{\mathrm{W}1}} \frac{\partial \eta_1}{\partial t} - g_{\mathrm{sub}}(T_1 - T_0) - g_{\mathrm{poly}}(T_1 - T_2), \quad (3.1)$$

$$\frac{\partial}{\partial t} \eta_1(x,t) = k_1 (1 - \eta_1) \exp\left(-\frac{E_{\mathrm{a}1}}{R T_1}\right), \quad (3.2)$$

$$\rho_2 c_2 A_2 \frac{\partial}{\partial t} T_2(x,t) = \kappa_2 A_2 \frac{\partial^2 T_2}{\partial x^2} + \frac{\rho_2 A_2 Q_2}{M_{\mathrm{W}2}} \frac{\partial \eta_2}{\partial t} - g_{\mathrm{out}}(T_2 - T_0) - g_{\mathrm{poly}}(T_2 - T_1), \quad (3.3)$$

$$\frac{\partial}{\partial t} \eta_2(x,t) = k_2 (1 - \eta_2) \exp\left(-\frac{E_{\mathrm{a}2}}{R T_2}\right), \quad (3.4)$$

where subscripts 1 and 2 indicate an SWNT and the inner PMMA layer, respectively, ρ is the mass density, c is the specific heat capacity, T is the temperature as a function of axial position x and time t, κ is the thermal conductivity, A is the cross-section, Q is the heat of combustion, M_{w} is the molecular weight, g_{sub} is the thermal boundary conductance (TBC) at the SWNT/SiO_2 interface per unit length, g_{poly} is the TBC at the SWNT/PMMA interface, and g_{out} is the TBC at a virtual interface of the inner/outer PMMA. η is the extent of oxidation ($0 \leq \eta \leq 1$), E_{a} is the activation energy of the oxidation reaction, k is the Arrhenius prefactor (collision rate), and R is the gas constant. Parameters used in the simulation are listed in Table 3.1.[142–145] g_{sub} and $E_{\mathrm{a}1}$ were estimated from preliminary experiments.[127] g_{out} is assumed to be 30 MW/mK, based on a two-dimensional temperature simulation.[127] Note that an appropriate value of the Arrhenius prefactor k for the oxidation of SWNTs and PMMA, especially when water molecules are involved in the oxidation reaction, has not been reported. Therefore, after determining the other parameters, the Arrhenius prefactor was adjusted to be 1×10^{14} s^{-1}, so that oxidation of PMMA-coated SWNTs was self-propagated. This extremely large value roughly corresponds to the frequency of molecular vibration and can be interpreted as the direct supply of water molecules as an oxidant from the adsorbed layers.

In order to simulate the burning initiated by voltage-driven etching (described later in Figure 3.8), the temperature of the SWNT edge (20 nm in length) and the surrounding inner PMMA was given at 573 K as an initial condition. The burning of the SWNTs coated with PMMA was self-propagated along the axis, as clear from the temperature-time profiles of the SWNT (bottom) and inner PMMA (top) in Figure 3.7(d). Figure 3.7(e) shows the 1D temperature distribution along the SWNT and inner PMMA at three different times (t = 10, 500, and 1000 ps) after ignition. Since the thermal conductivity of SWNTs is much higher than that of PMMA, the SWNT conducted more heat along the axis and had a less steep temperature gradient than PMMA.

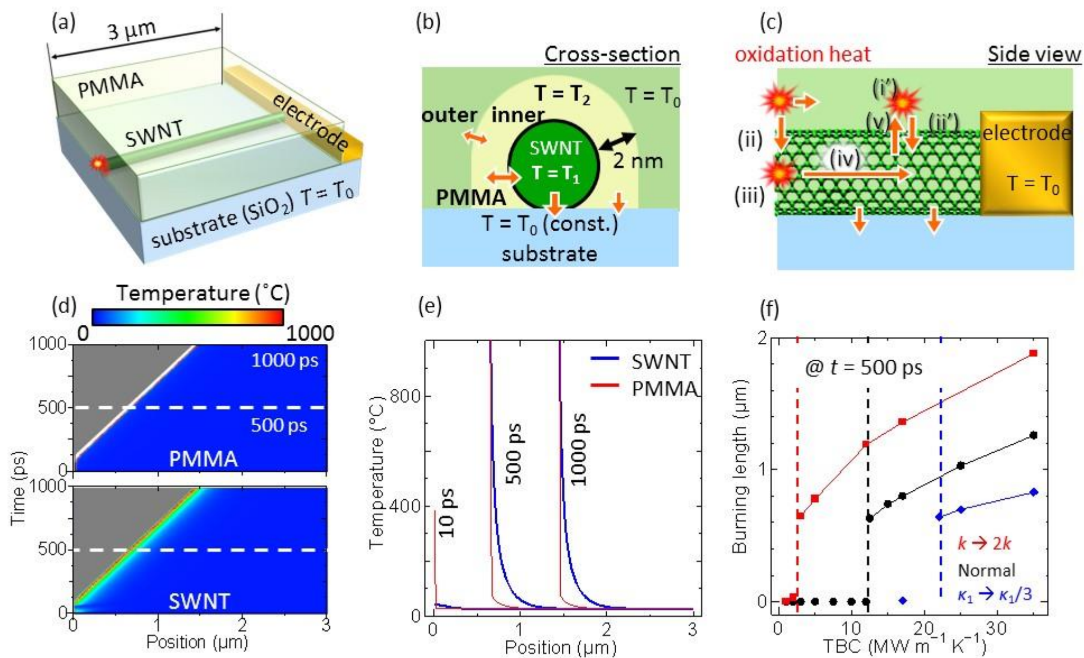

Figure 3.7 (a) Schematic of the simulation setup. One side of an SWNT on SiO_2 (= T_0) is connected to metal contacts (= T_0). (b) Cross-section and (c) side views of the heat flow model. For simplicity, the 2-nm-thick PMMA layer has variable temperature and is further surrounded by the outer PMMA film, which is kept at room temperature (= T_0). (d) Simulated time-profile of temperature distribution along a PMMA-coated SWNT. The burned regions of the SWNT and PMMA are shown in gray. (e) 1D temperature profiles of the SWNT (blue) and the inner PMMA (red) at various times. (f) Dependence of the simulated burning length at t = 500 ps on TBC at the SWNT/PMMA interface. Results for high Arrhenius prefactor $k_{1,2}$ and low SWNT thermal conductivity κ_1 are also shown in red and blue, respectively. Adapted with permission from ref. [127]. Copyright 2017 Springer.

Table 3.1 Parameters used in the simulation of SWNT-PMMA burning. All the simulation results were obtained using these parameters, unless otherwise mentioned.

Chirality (n,m)	L_{ch} [μm]	κ_1 (@ 300 K) [W m^{-1} K^{-1}]	κ_2 [W m^{-1} K^{-1}]	$k_{1,2}$ [s^{-1}]	g_{sub}/d_t [W m^{-1} K^{-1}]	g_{poly}/A_{wall} [W m^{-1} K^{-1}]	E_{a1} [eV]	E_{a2} [eV]
10,10	3	1×10^{3}†	0.2	1×10^{14}	2.0×10^{7}‡	1.3×10^{7}	1.4	0.6§

† The same temperature dependence [142] as that in the literature was given for the thermal conductivity κ_1. An intermediate value between theoretical [145] and experimental [142] studies was employed as the absolute value of κ_1 in this study.
‡ The TBC at the SWNT/polyethylene interface based on molecular dynamics [143] was used instead of that at the SWNT/PMMA interface.
§ Among the various levels of PMMA oxidation, the lowest activation energy based on thermogravimetry [144] was used here.

Figure 3.7(f) shows the burning length at t = 500 ps plot against the TBC of the SWNT/PMMA boundary with various Arrhenius prefactors k, or thermal conductivity of SWNTs, κ_1. When the TBC g_{poly} was lower than the threshold, burning did not propagate at all. Efficient heat flow between SWNTs and PMMA films is thus required for the self-sustained burning. On the other hand, SWNT burning without the PMMA coating can be simulated by setting the TBC at the SWNT/PMMA interface to zero, which results in no propagation of burning, even when the temperature of the edge is set much higher than 573 K. Simulation for low thermal conductivity of SWNTs, as shown in Figure 3.7(f) (blue), indicates that thermal conductivity is also an important factor to achieve self-propagation of SWNT-PMMA burning. SWNTs are one-dimensional materials that have high thermal conductivity only in the axial direction; therefore, lateral propagation of the burning via the PMMA thin films, which could result in the removal of s-SWNTs, is unlikely to occur. It should be stressed that when the Arrhenius prefactor is set at 1×10^{9} s^{-1}, which is similar to the collision frequency of oxygen to carbon atoms of SWNTs in ambient air, the oxidation reaction was very quickly terminated.

The self-sustained burning mechanism of SWNTs and PMMA is summarized as follows. First, the inner PMMA begins to oxidize (step i in Figure 3.7(c)) prior to SWNT due to its lower activation energy, and then heats the SWNT from the outside (step ii). This in turn induces SWNT oxidation (step iii). Heat at the reaction front is transferred along the tube axis (step iv). The transferred heat then induces subsequent

oxidation of the PMMA in the vicinity (step v). This cycle (steps i–v) takes place repeatedly, and results in self-propagation of oxidation reaction of SWNTs and PMMA.

It was previously considered that uniform Joule self-heating along SWNTs is necessary to achieve full-length burning, by assuming that oxidation should propagate before the electrically heated SWNTs are cooled down.[128] However, the assumption is contradicted by the simulation without Joule self-heating (when TBC is zero in Figure 3.7(d)). The importance of uniform Joule self-heating is also excluded by the experimental results for re-burning from nanogaps (explained later in Figure 3.14). The burning of SWNTs is self-sustained, despite the ultrafast cooling, so it would propagate over any length until contacts with the metal electrodes, unless non-uniformities are present along the axis.[127] Ideally, an arbitrary length of SWNTs can be therefore removed by WPA burning, as experimentally demonstrated by the full-length burning of 29-μm-long SWNTs.[127]

3.3 Secrets behind the one-way burning

3.3.1 Remote etching during electrical breakdown

The burning-based purification method basically utilizes Joule-self-heating in m-SWNTs to obtain the selectivity in a similar manner to the electrical breakdown method, which successfully worked for the SWNT arrays with the density of >100 SWNTs/μm.[117] However, the voltage needed to break m-SWNTs (breakdown voltage, V_{BD}) proportionally increases as the SWNT (or channel) length becomes longer. In general, discharge or electric arc starts under high bias voltage, making things complicated and much different from a low voltage regime. Therefore, such phenomena particular to a high voltage regime has to be taken into account to explore the possibility of the burning-based purification method toward the high-performance transistor application.

In this section, SWNT array especially after a breakdown are carefully observed before/after a high voltage application along the axis. Electrical breakdown of SWNT arrays was performed in air to form nanogaps in m-SWNTs. This process was done at ~100°C to make the initial gas smaller (the reason will be described later) than 100 nm. A positive gate voltage (V_G = 10 V) was applied to selectively break m-SWNTs. Left panel of Figure 3.8 shows SEM images of a typical SWNT nanogap. After gap

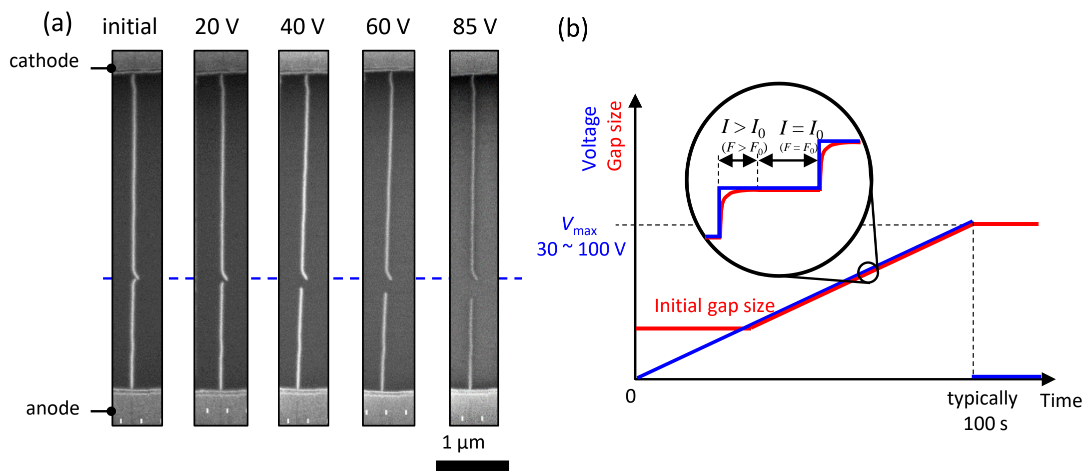

Figure 3.8 (a) SEM images of an SWNT after gap formation and gap extension in air. The initial gap was formed with a ramp voltage up to V_{max} = 25 V on a heated substrate, followed by subsequent application of V_{max} = 20, 40, 60 and 85 V at room temperature. (b) Schematic for time evolution of gap size and applied voltage. Inset shows the gap size change that follows the stepwise increase of voltage. Adapted from ref. [131]. Published by The Royal Society of Chemistry.

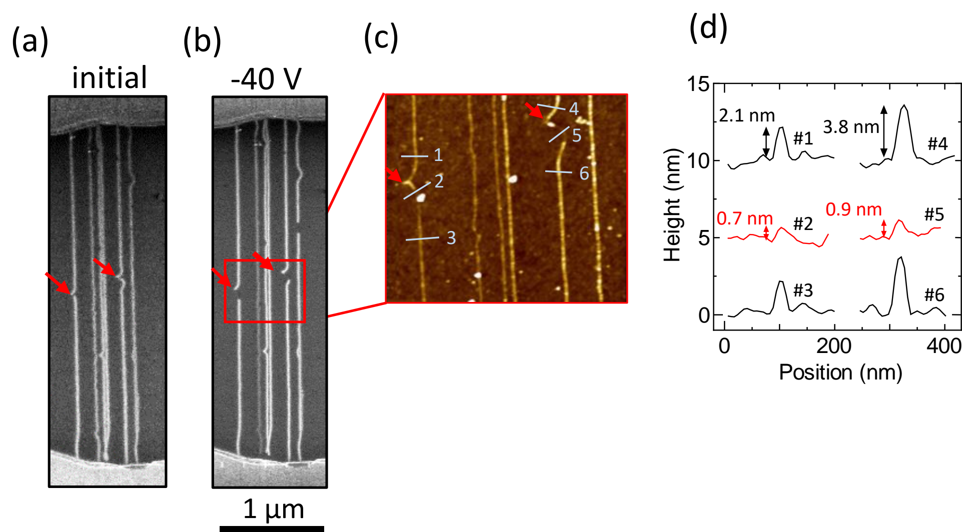

Figure 3.9 (a,b) SEM images of SWNTs just after nanogap formation and (b) after gap extension with ramp voltage up to 40 V. (c) AFM image of the region outlined in red in (b). Initial gap location is denoted by arrows. (d) Cross-section profiles of two SWNTs. Red lines indicates the profiles at the nanogaps, showing non-existence of SWNTs. Adapted from ref. [131]. Published by The Royal Society of Chemistry.

formation, ramp voltages from 0 to V_{max} = 20, 40, 60, and 85 V were applied to the same SWNT array in air at room temperature.

Figure 3.8(a) shows SEM images of an identical SWNT after the several voltage ramps. This clearly shows that the gap was extended only in the anode direction (one-way gap extension). The initial and final gap sizes were 63 and 337 nm, respectively. AFM was also used to observe the etched SWNTs, confirming the removal of the SWNT. It should be noted that the etching of SWNTs on the anode side self-terminated in a very short time, as is clear from time-independence of gap size. Therefore, the etching length is simply determined by applied voltage, rather than by the product of etching rate and etching time. In this experiment, the voltage was increased stepwise due to instrument machine constraints, so that the gap size changes immediately after the voltage goes up (when $F > F_0$) and keeps the same size until the next voltage increment (when $F = F_0$) as schematically explained in Figure 3.8(b).

Figures 3.9(a–c) show SEM images of SWNT nanogaps before and after gap extension up to V_{max} = 40 V, and an AFM image of the extended gaps in the region outlined in the SEM image. The AFM image also shows that the SWNTs on the anode

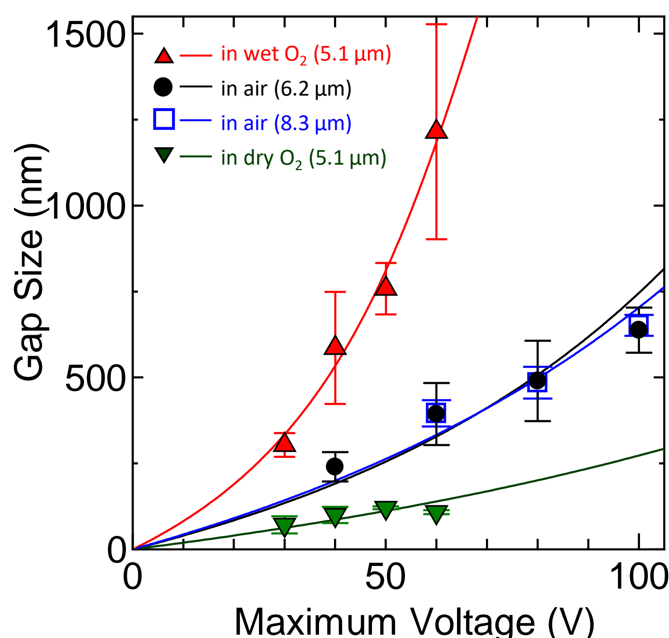

Figure 3.10 Gap size as a function of maximum applied voltages under various gas conditions (in air, dry O_2, and wet O_2). Circles (black) and open rectangles (blue) indicate the size of SWNT gaps extended in air with L_{ch} = 6.2 and 8.3 µm, respectively. Inversed triangles (green) represent the size of the gaps formed by electrical breakdown in dry oxygen. Red triangles correspond to identical gap arrays further extended in wet oxygen with the same maximum voltages. L_{ch} = 5.1 µm. Solid lines represent the best-fit of the data for each condition with Equation (3.7). Adapted from ref. [131]. Published by The Royal Society of Chemistry.

side were etched from the initial gap location denoted by arrows. Only residues thinner than the SWNTs remained on the substrate, as cross section profiles from two SWNTs exhibit (Figure 3.9(d)).

Experiments similar to that in air were performed for SWNT arrays with channel lengths of L_{ch} = 6.2 and 8.3 µm, by changing the maximum voltage from V_{max} = 40 to 100 V in 20 V steps. Ten SWNTs were typically broken down for the following gap extension experiment under each condition, while most s-SWNTs were preserved by gate control. Each maximum voltage was applied to different SWNT arrays for the same length of time, though the size of gaps extended with a constant voltage applied for 1 s did not further change even after 1000 s in a control experiment. The sizes of the extended SWNT gaps with L_{ch} = 6.2 and 8.3 µm are plotted as a function of V_{max} in Figure 3.10. Here, error bars indicate the standard deviation of the extended gap

size. Similar gap sizes and voltage-dependence were obtained for SWNT arrays of both lengths.

3.3.2 Size determination of nanogaps produced by electrical breakdown

A possible mechanism for the SWNT gap size obtained by electrical breakdown on substrates is proposed as follows. The gaps initially have a gap size of sub-10 nm immediately after the breakdown of SWNTs, as such small gaps were obtained in a previous study,[127] and they are readily extended by continuous application of the voltage. One might wonder if chain-reaction burning of SWNTs results in large gap formation, as already discussed in Chapter 3.2 and or in a previous publication on organic film-assisted burning of SWNTs.[128] However, the oxygen-induced chain reaction is not expected as long as the SWNTs are directly exposed to dry air and are in contact with the substrates. This is because the collision frequency of oxygen molecules with SWNTs in air (~10^9 s^{-1}) is relatively small compared to the thermal relaxation time of SWNTs on substrates (<100 ps).[138] Furthermore, if chain-reaction burning dominates the gap formation process, then heating of the substrates during electrical breakdown should lead to larger gap formation. In contrast, the experimental results indicated the opposite.[131] The electrical breakdown of SWNTs on substrates did not indicate a clear dependence of the gap size on oxygen partial pressure,[131] which also excludes the chain-reaction burning as a reason for the gap extension.

It should be emphasized that the dependence of gap size on the applied voltage can be used to explain the previous finding that electrical breakdown of longer SWNTs resulted in larger gap formation.[146,147] It is approximated here that the extended gap size is proportional to the maximum voltage for small gaps ($L_{gap} = k_1 V_{max}$, where k_1 is a constant). The breakdown voltage, the voltage required to heat up the SWNTs to oxidation temperature (typically ~600°C), is proportional to the SWNT length ($V_{BD} = k_2 L_{ch}$, where k_2 was determined as 4.48 V/μm in the previous studies) for long SWNTs ($L_{ch} > 1$ μm).[122,148] If the voltage is ramped until an SWNT is broken, then the extended gap size will also be proportional to the SWNT length ($L_{gap} = k_1 V_{BD} = k_1 k_2 L_{ch}$). Therefore, the use of shorter SWNTs (small L_{ch}) is preferable for nanogap applications in energy-efficient and highly-integrated devices.

3.3.3 Effects of ambient water on the remote etching

The dependence of the extent of gap extension on the ambient gas conditions was then examined. Figure 3.10 (green inverted triangles) shows the size of gaps formed in SWNTs with L_{ch} = 5.1 μm by electrical breakdown up to four different V_{max} in the flow of dry oxygen. The gap size here represents the extended gap size due to voltage application after cutting of the SWNTs, though gap formation and gap extension processes were not separated. The gaps formed in dry oxygen were smaller than those in ambient air (Figure 3.10), which suggests that oxygen molecules are not critical for the SWNT gap extension phenomenon. Some other gas species in air play a key role.

The gaps were further extended in wet oxygen with the same maximum voltages as those in dry oxygen. Figure 3.10 (red triangles) shows that the extended gap size achieved in the presence of water is much larger than that under other conditions with lower relative humidity (RH) (wet oxygen ~100%RH, dry oxygen ~0%RH, and laboratory ambient air 30–60%RH). Gap extension experiments conducted in wet nitrogen (data not shown) revealed similar results to those in wet oxygen, which also denys the importance of oxygen in the gap extension process. Since higher humidity resulted in larger gap sizes, water vapor plays a key role in the voltage-driven extension of SWNT gaps. Based on this knowledge, the smaller gap formation by breakdown in Ar gas flow (L_{gap} = 30–100 nm) than in air (L_{gap} = 30–200 nm), as reported previously,[147] can be explained by the low humidity in the Ar gas flow, rather than by low oxygen partial pressure. Therefore, to further decrease the SWNT gap size, electrical breakdown should be performed in high-pressure dry oxygen. This is not only because dry gas prevents gap extension, but also because high-pressure oxygen lowers the breakdown voltage of SWNTs.[131]

3.3.4 Field emission at SWNT nanogaps

The SWNT gap extension process must involve charge transfer and an etching reaction; therefore, the current-voltage (*I*-*V*) characteristics during gap extension in air were carefully observed.[131] Although no conductive materials should be left at the gaps after breakdown of all SWNTs, a small and unstable current was still observed through the SWNT gaps. Recently, field emission (Fowler-Nordheim tunneling) at SWNT gaps on substrates with L_{gap} = 23–125 nm were examined using an electrostatic

force microscopy technique.[149] For gaps of m-SWNTs with any gap size or s-SWNTs with L_{gap} > 60 nm, field emission was revealed to be the dominant charge transfer mechanism. In addition, field emission during electrical breakdown has been briefly discussed in the literature; however, there has been no detailed investigation.[150]

To elucidate the charge transfer mechanism at the SWNT gaps in the present work, field emission properties at m-SWNT nanogaps were measured in a vacuum (~0.02 Pa) to avoid damage to the anode SWNTs (gap extension). An experimental device was fabricated that contains a single SWNT, as shown in Figures 3.11(a) and (b). *I*-*V* characteristics were measured for SWNT gaps with L_{gap} of ~80 and ~300 nm (L_{ch} = 8.2 and 14.1 μm, respectively) by ramping the bias voltage from 0 V, while the gate voltage was kept equal to the cathode voltage. Figure 3.11(c) shows *I*-*V* characteristics for these gaps, where steep current increases in the sub-nA range were observed at

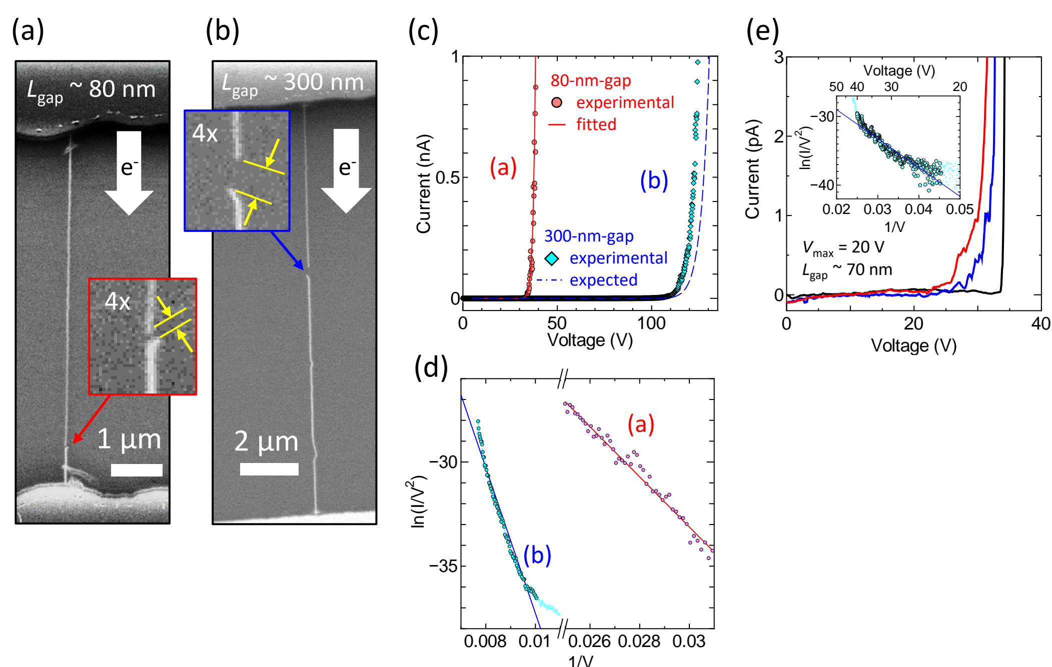

Figure 3.11 (a,b) SEM images of single SWNT gaps with L_{gap} = 80 and 300 nm, respectively. Insets show enlarged images of the gaps. (c) *I*-*V* characteristics in vacuum and (d) FN plots of the SWNT gaps shown in (a,b). Red solid and blue dashed lines represent the fitted field emission properties with the data for the 80 nm gap and the expected field emission properties of geometrical features of the 300 nm gap, respectively. (e) *I*-*V* characteristics of three SWNT gaps formed with voltage application up to V_{max} = 20 V. Inset: The current at 20 V (=V_{max}) is estimated by extrapolation of the FN plot. Adapted from ref. [131]. Published by The Royal Society of Chemistry.

35 V (line (a) in Figure 3.11(c)) and 110 V (line (b) in Figure 3.11(c)). Fowler-Nordheim (FN) plots for the measurement (Figure 3.11(d)) yield straight lines (solid lines show the best-fits). When it is assumed that the electrons were emitted into vacuum from SWNTs with work function of 4.8 eV,[151] the field enhancement factors γ for the gaps shown in Figures 3.11(a) and (b) are calculated from the slopes [152] to be 460 and 273, respectively. Note that $\gamma = F/E$, where F and E are a local field at the emitter surface and the macroscopic field (applied voltage V divided by the inter-electrode distance L_{ch}), respectively. Despite the large difference in a sample configuration, the field enhancement factors roughly comparable to a previous report for free-standing SWNT field emitters ($\gamma = 515$).[152]

The field emission characteristics for three similar SWNT gaps were also compared. Following gap formation by electrical breakdown on heated substrates (~100°C), the gaps were extended with $V_{max} = 20$ V in air at room temperature. The sizes of all the extended gaps were around 70 nm. As shown in Figure 3.11(e), the I-V characteristics of these gaps in vacuum show onset voltages around 25–35 V, which were slightly larger than the maximum voltage ($V_{max} = 20$ V) for gap extension. These gaps were extended with $V_{max} = 20$ V; therefore, the minimum current required for in-air gap extension (threshold current) can be estimated from the emission current at $V = 20$ V in vacuum. Extrapolation of the FN plot for the gap drawn in blue yielded a threshold current of 0.1–1 fA at $V = 20$ V (inset of Figure 3.11(e) and Figure 3.12), which was beyond the range of measurement due to noise in the present setup. The field emission properties of SWNTs can be affected by the adsorption of oxygen and water molecules in air.[153,154] Note that the linear current component obtained from the device without SWNTs ($I/V = 14.9$ [fA/V]) was deducted in Figure 3.11(e) to exclude leakages that did not originate from the SWNTs.

Although the field emission current was measured in vacuum, the surface leakage current *via* water adsorbed on the substrates must be considered as another conduction mechanism in the presence of water vapor. Charge transfer between SWNTs and water electrolyte (electrochemical reaction) requires an electric field with a specific strength at the interface. Therefore, a higher voltage is required to maintain the constant field strength for larger SWNT gaps, which may appear as the observed relation between the applied voltage and gap size (Figure 3.10). Even in that case, the field emission

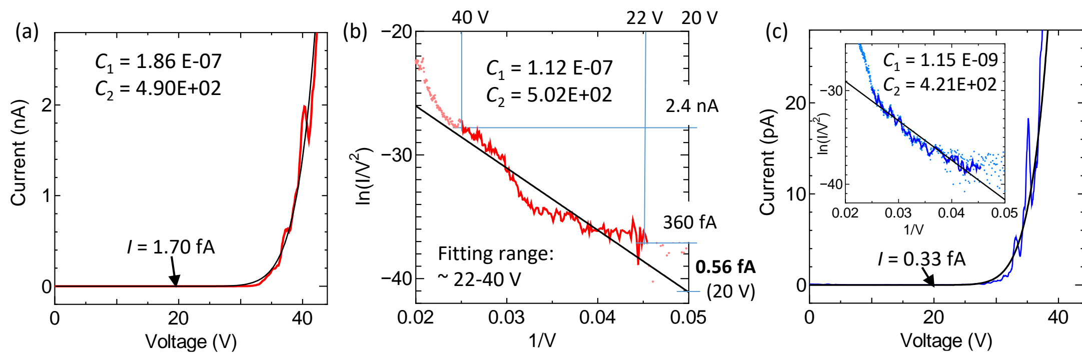

Figure 3.12 (a) Fitting line for the experimental *I*-*V* characteristic [in red in Figure 3.11(c)] with the FN law [$I = C_1V_2\exp(-C_2/V)$]. (b) Similar fitting for the FN plots for the same gap. Since the gap was extended by bias voltage of V = 20 V, these fittings yield the threshold current for gap extension in air of I = 0.56–1.70 fA. (c) The same fitting was applied to the gap drawn in blue in Figure 3.11(e). This gap yields the threshold current of I = 0.33 fA.

measurement in a vacuum is useful for quantification of the field enhancement at SWNT tips.

3.3.5 Threshold field for gap extension: gap size *versus* voltage

Here, the validity of the field emission electron as one of the driving forces of SWNT etching is evaluated. The emission current is assumed to keep the same (threshold current, I_0) during the gap extension process because the gap size changes according to the ramp voltage. The FN law gives the relation between the emission current I [A], and the local field at the emitter surface F [V/m], as:[155]

$$I = A\frac{1.5\times10^{-6}}{\phi}F^2\exp\left(\frac{10.4}{\sqrt{\phi}}\right)\times\exp\left(-\frac{6.44\times10^9\phi^{\frac{3}{2}}}{F}\right), \tag{3.5}$$

where A [m²] is the emission area and φ [eV] is the work function of the SWNT emitters. The local field F is obtained from the macroscopic field E and the field enhancement factor γ at the emitter surface. The FN law indicates that the local field F (= γE) is a constant value of F_0 during the gap extension under this premise, though F_0 differs according to the ambient gas conditions. Even when the water-mediated leakage current is the main charge transfer mechanism, the local field F at the nanotube tips also dominates the electrochemical oxidation (*i.e.* gap extension). Previous studies have reported models to estimate the field enhancement factor γ from geometric features, such as the length of the CNT emitter h, the distance between the flat anode and CNT tips D, and the radius r, for free-standing CNT emitters.[152,156,157] When

the inter-electrode distance is large compared to the height of CNT, the field enhancement factor γ is simply estimated by the CNT height and the nanotube radius ($\gamma_0 \propto 1+\sqrt{h/2r}$).[157] For the case of small D, $\gamma = \gamma_0\times\{1+a\times[D/(D+h)]^{-1}-b\times[D/(D+h)]\}$ is often used as the modified relation,[152] where a and b are constants. The relation can be further rewritten to match the configuration of the present samples:

$$\gamma = c\left(1+\sqrt{\frac{L_{\mathrm{ch}}-L_{\mathrm{gap}}}{4r}}\right)\left(1+a\frac{L_{\mathrm{ch}}}{L_{\mathrm{gap}}}-b\frac{L_{\mathrm{gap}}}{L_{\mathrm{ch}}}\right), \tag{3.6}$$

where c and L_{ch} are a constant and the channel length (original SWNT length) of the device, respectively. From the relation $F = \gamma V_{max}/L_{ch}$, the maximum voltage V_{max} that gives the constant local field F_0 at the SWNT tips for any gap size L_{gap} is expressed as:

$$V_{\mathrm{max}}(L_{\mathrm{gap}}) = \frac{F_0 L_{\mathrm{ch}}}{\gamma}. \tag{3.7}$$

Equation 3.7 was fitted to the experimental data in Figure 3.10 with a and F_0/c as fitting parameters. The diameter of all the SWNTs was assumed to be 1.5 nm.[97] When $a = 0.11$, the fitting lines corresponded well with the trend of the experimental data under all the conditions, as shown in Figure 310. The b constant has little effect on the fitting results; therefore, b was set at zero. Compared to the threshold field $F_{0,air}$ obtained from the data in air ($L_{ch} = 6.2$ μm), the other threshold field strengths for the gap extension in wet oxygen ($L_{ch} = 5.1$ μm), in air ($L_{ch} = 8.3$ μm), and in dry oxygen ($L_{ch} = 5.1$ μm) were $0.47F_{0,air}$, $1.04F_{0,air}$, and $1.80F_{0,air}$, respectively. Enhancement of the emission current at a given field by water adsorption on SWNTs [154,158] can account for the lower threshold field under higher humidity conditions. Also, switching of the major charge transfer mechanisms from field emission to water-mediated surface leakage current is another possible explanation for the low threshold field in the presence of water vapor.

This relation was applied again to the calculation of *I-V* characteristics for field emission using the FN law (Equation 3.5). Here, an SWNT diameter d_t of 1.5 nm and $\varphi = 4.8$ eV are supposed for simplicity. The emission area A is estimated from the y-intercept of the FN plot to be 7.0×10^{-12} m^2. First, $c = 0.66$ was obtained by fitting with the field emission characteristics of the 80 nm gap shown in Figure 3.11(c) (red line). The *I-V* characteristics for the 300 nm gap were then predicted from the gap

configuration using Equations 3.5 and 3.6. As shown in Figure 3.11(c), the predicted *I-V* characteristics (blue dashed line) are in good accordance with the experimental results. This indicates that the relationship between the geometric features and the field enhancement factor γ (Equation 3.6) can be used to predict the field emission characteristics at SWNT gaps on substrates, and also that the gap extension is dominated by the geometrically-derived field enhancement at the SWNT tips. Note that L_{ch} of 12.5 and 11.5 μm were substituted into Equation 3.6 for 80 and 300 nm gaps, respectively, because the length of the SWNTs on the cathode side rather than the distance between two metal (Pd) contacts influence the field enhancement. The threshold field strength in air $F_{0,air} = 1.7\times10^9$ V/m was obtained from the threshold current $I_0 = 0.1–1$ fA. Field emission into vacuum was assumed here, though a similar comparison of the 80 nm and 300 nm gaps is possible for field emission (FN tunneling) into SiO_2 with slight modification of the parameters.

Taking field-emission electrons and water molecules into account, two mechanisms for SWNT etching are proposed as follows. In ambient air, the SWNT surface is covered with a few layers of water molecules.[66,132] The first possible mechanism is electrochemical etching of anode SWNTs,[159] where charge transfer occurs *via* field emission or water-mediated surface current. Electrochemical oxidation first occurs on surfaces, which forms covalently functionalized groups on SWNTs. The locally functionalized SWNTs are then removed through further oxidation. The total reactions can be expressed as $C(SWNT) + 3OH^- \rightarrow CO_3^{2-} + 3H^+ + 4e^-$. In contrast to the electrochemical etching of SWNTs in bulk electrolytes, physisorbed water from the air is unlikely to form an electric double layer under the conditions of the present experiments, which typically strengthens the field at the SWNT-electrolyte interfaces. Instead, field enhancement at the SWNT tips due to the ultrahigh aspect ratio may play an important role in the oxidation process. SWNT etching may continue either until the gaps are extended to a sufficient extent for the emission current to be negligible or until the local field at the tips become weak enough to not cause the electrochemical reaction.

A second possible explanation for the gap extension is as follows. Electrons emitted from cathode tips are accelerated by an electric field while flowing in the SWNT gaps. Physisorbed water molecules on the SWNT tips are ionized by

accelerated electrons and turn into highly reactive species, such as OH·, H·, and HO_2· radicals. These species then etch neighboring carbon atoms of the SWNTs to form CO, CO_2, and various hydrocarbons. A similar etching phenomenon was reported in studies on CNT cutting [160] and the machining of CNT forests,[161] where CNTs were cut with a low-energy focused electron beam (inside an SEM chamber) in the presence of water vapor.

As already discussed, electrical breakdown on heated substrates resulted in smaller gap formation because water molecules on the SWNT surfaces desorb at high temperature, even under the same water vapor pressure.[131] This indicated the importance of adsorbed water molecules rather than water molecules in the gas phase, which supports both mechanisms proposed here. Even when the emission current is sufficiently large, the gaps are not extended in the absence of water molecules on anode side SWNTs (*e.g.*, in vacuum).

3.3.6 Remote etching among adjacent SWNTs

The remote etching phenomenon of anode SWNTs parallel to cathode SWNTs with small inter-SWNT spacing is found, as shown in Figure 3.13(a). Here, the SWNTs that connect only with metal anodes or cathodes are referred to as A-SWNTs or C-SWNTs, respectively. Gaps were first formed at a red arrow position and then extended to an L_{gap} of a few microns, whereas the other two gaps were only extended to an L_{gap} of a few hundreds nanometers. This can be explained by field enhancement between side walls of A- and C-SWNTs,[162] which induces the etching of adjacent A-SWNTs, as schematically explained in Figure 3.13(b). Red and blue in the schematic indicate high and low electric potentials, respectively. A-SWNTs (red) within a certain distance from C-SWNTs (inside the gray region) can be etched away. Although this etching mechanism is intrinsically the same as the gap extension discussed so far, the extent to which the SWNTs are etched away is determined by the distance between the two gaps of A- and C-SWNTs.

In addition, whether etching occur or not is dependent both on the inter-SWNT spacing of parallel SWNTs and the applied voltage. If uniformly dense SWNT arrays can be grown and also m- and s-SWNTs are intentionally cut near cathodes and anodes,

respectively, then this etching in parallel SWNTs could be used to eliminate only m-SWNTs by utilizing selective field emission from the side wall of s-SWNTs.

On the other hand, this type of etching might deteriorate the removal selectivity during electrical breakdown through the cutting or damage of the adjacent s-SWNTs. For example, the SWNT that did not bridge two metallic contacts due to electrical breakdown was cut again around the neighboring nanogap, as indicated by a blue arrow in Figure 3.14(c). This indicates that SWNTs can be broken down without Joule self-heating if nanogaps are present in the vicinity. The SWNT segment between the red and blue arrows had a low contrast to the substrate in the SEM image, which also indicates the physical isolation of the SWNT segment from other SWNTs and metal electrodes.[163]

If ionization of water molecules by accelerated electrons induces the cutting of unbridged SWNTs, then processing with voltages smaller than the ionization energy of water (~12.7 eV) would be helpful to avoid deterioration of the removal selectivity.

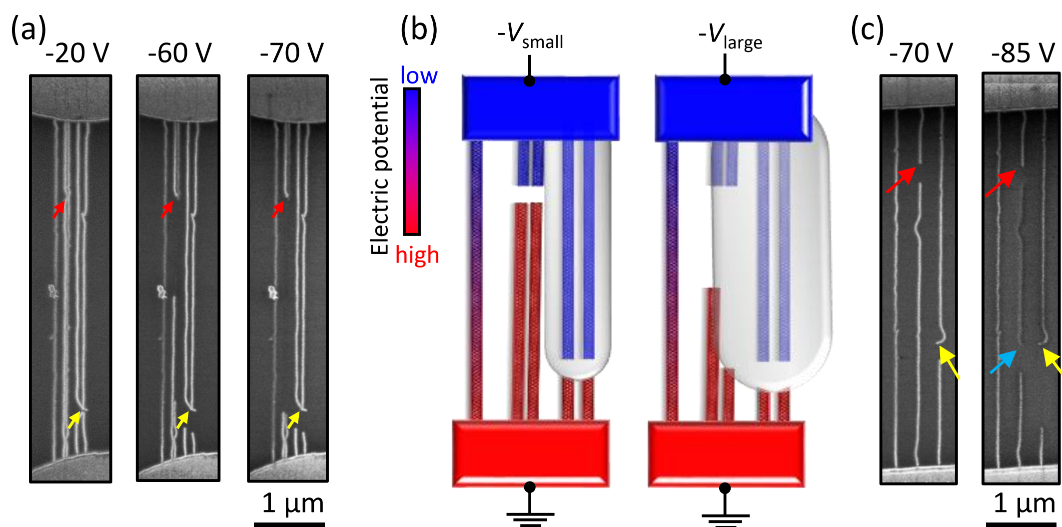

Figure 3.13 (a) SEM images of five parallel SWNTs. Each image was taken after voltage application up to V_{max} as indicated. The red and yellow arrows indicate the initial gap location on the anode and cathode SWNTs (A- and C-SWNTs), respectively. Two A-SWNTs in the middle were etched from over a few microns because of right C-SWNTs. (b) Schematics of the electric potential at two stages of the SWNT array in (a). Left: after the gap formation at the red arrow position, corresponding to 20 V < V_{max} < 60 V. Right: after the remote etching of A-SWNTs, corresponding to V_{max} = 60 V. Field emission from C-SWNTs can affect A-SWNTs inside the gray area. (c) SEM images for the double cutting of a single SWNT. Secondary cutting of the middle SWNT occurred at the position marked by blue arrow. Adapted from ref. [131]. Published by The Royal Society of Chemistry.

The electrical breakdown of SWNT arrays (~20 SWNTs/μm, L_{ch} = 2 μm), where a bias voltage of 20 V was applied, resulted in the correlated breakdown of neighboring SWNTs,[164] though this was previously explained in a different way.[134] In contrast, the electrical breakdown of higher-density but shorter SWNT arrays (>100 SWNTs/μm, L_{ch} = 400 nm), where the breakdown voltage is always <8 V, successfully cut only m-SWNTs (current retention >20%).[117] Note that a relatively thick gate dielectric (Al_2O_x, 25 nm equivalent oxide thickness) compared to the inter-SWNT spacing (<10 nm) was used, and high electric field (>10 V/μm) was applied.[117] The results of adjacent SWNT etching will thus provide a guide to the design of appropriate device structures and the processing conditions required for successful breakdown of m-SWNTs.

3.3.7 One-way burning from pre-formed nanogaps

Keeping the voltage-induced etching in mind, the focus is then directed back to the water- and polymer-assisted burning of SWNTs. Burning of the SWNTs from the nanogaps formed by electrical breakdown was performed to confirm whether one-way burning could occur during voltage application treatment under the WPA condition. Observations of nanogaps similar to the last section were conducted after electrical breakdown under the WPA condition.

Electrical breakdown of uncoated SWNTs was conducted in air while the substrate was heated at 100C to produce small gaps (~100 nm). Three different ramp

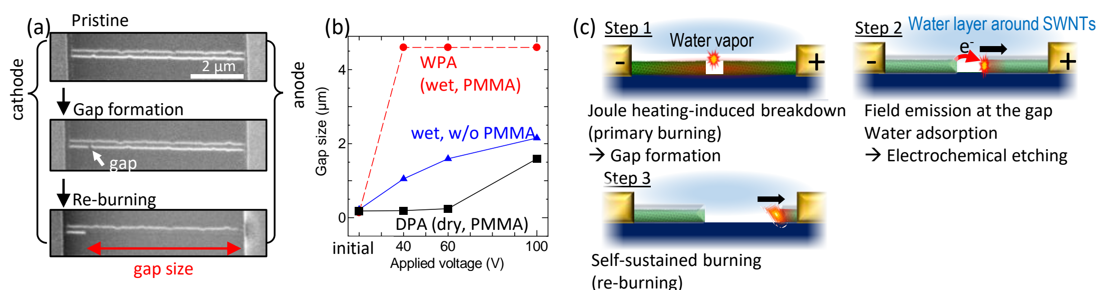

Figure 3.14 (a) SEM images of two parallel SWNTs (upper one is semiconducting, the lower one is metallic). Pristine SWNTs before electrical breakdown (top), after nanogap formation (middle), and after the burning from pre-formed nanogaps (bottom). (b) Gap size *versus* the voltage applied across the SWNTs for three different conditions. (c) Schematics showing how the one-way burning occurs and determine the removed length of SWNTs. Adapted with permission from ref. [127]. Copyright 2017 Springer.

voltages (up to 40, 60, and 100 V) were sequentially applied to the broken SWNTs with gaps under the WPA and DPA conditions, and in wet oxygen without the PMMA coating. The top panel of Figure 3.14(a) shows an SEM image of two parallel SWNTs, one of which was electrically broken down in air (middle). After spin-coating of PMMA and second voltage application under the WPA condition, only the anode side of the lower SWNT was completely eliminated, while the upper s-SWNT was not burned or damaged (bottom). Figure 3.14(b) shows the average size of extended gaps as a function of the applied voltage for the three conditions examined. The gaps treated under the DPA condition and under wet oxygen without the PMMA coating were enlarged as the applied voltage was increased, similar to the experiments in Chapter 3.3.[131] In contrast, all the SWNTs on the anode side from the nanogaps were completely removed after the first voltage application (40 V) under the WPA condition, and no voltage dependence was observed.

The full-length removal on the anode side under the WPA condition can be attributed to self-sustained burning triggered by voltage-driven etching [131], as schematically presented by steps 2 and 3 in Figure 3.14(c). Broken SWNTs with nanogaps, which do not generate Joule heating, will be surrounded by water molecules. Due to the high field localized and amplified in the nanogaps, the SWNT edges on the anode side begin to be etched (step 2). This continuously leads to self-sustained

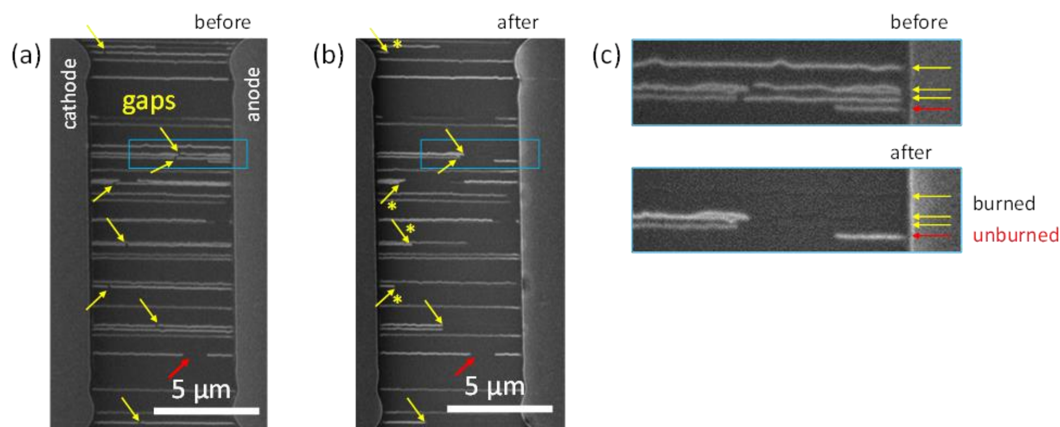

Figure 3.15 SEM images of an SWNT array before (a) and after (b) re-burning under WPA condition. Arrows indicate the SWNT gaps formed by electrical breakdown. 40 V bias was applied to re-burn broken SWNTs. A relatively large gap indicated by a red arrow was not extended, even after voltage application up to 100 V. (c) Close-up images of outlined region in (a) and (b). Yellow arrows indicate (re-) burned SWNTs, while red does an unburned SWNT.

burning of the SWNTs at the anode side in the presence of polymer thin films, which can propagate along the tube axis without further application of an external voltage (step 3).

It should be emphasized that the full-length removal shown in Figure 3.14(a) was not caused by voltage-driven etching,[131] where the gap size increases according to the applied voltage. Small gaps (~100 nm) were always fully extended, but a relatively large gap (~1 μm) was not extended at all after the voltage application even up to 100 V, as shown in Figure 3.15. This is likely because the gap was too large for voltage-driven anode etching to trigger burning of the SWNT. Importantly, this result excluded voltage-driven etching as the mechanism for the full length removal of SWNTs at the anode side. Therefore, WPA burning can be applied to high-density SWNT arrays without damage to adjacent s-SWNTs *via* voltage-driven etching. This will be discussed in detail as an important aspect of the scaling of SWNT-based transistors.

Chapter 4:

Scalable Fabrication of SWNT Transistors

4.1 Three types of scaling of SWNT transistors

4.1.1 Ultrascaled channels and contacts

There are three scaling requirements for high-performance and energy-efficient electronics. One is the scaling to short channel lengths. In logic transistors, speed, power-efficiency, and costs have been exponentially improved by scaling down the dimension of transistors for nearly half a century, and the size is almost approaching 10 nm nowadays in the commercial products. However, planar bulk-Si transistors do not work reliably at the ultrascaled gate length below 10 nm due to so-called short-channel effects [165]. For the better gate control on channels, new structures of gate/channels that incorporate more than one gate per device have been developed. One strategy for further scaling is to make the channel thinner using silicon on insulator (SOI) substrates. Another approach to break the scaling limit is three-dimensional channel configuration, such as FinFET (dual gate), tri gate, and gate-all-around. Ultimate restructuring of 3D transistors is nanowire channels that are all wrapped by gate for the best electrostatic control.

Carbon nanotubes, which have extremely thin nanowire-like bodies by nature, can serve as the best channel material in terms of electrostatic control by gate. Furthermore, SWNTs have the high carrier mobility much exceeding Si (same for both electron and holes) and perfectly seamless structure even at ~1 nm diameter regime. Aggressive scaling of SWNT transistors less than 10-nm channel lengths was first reported in 2012. The ultrascaled transistor ($L_{CH} \approx 9$ nm) exhibit excellent switching with subthreshold swing (SS) of <100 mV/dec despite a single bottom gate because of the quasi 1D structure. More recently, carbon nanotube transistors with 5-nm gate lengths was

fabricated and showed a superb switching behavior (SS≈73 mV/dec), which is much better than Si MOS FETs with planar gate or multigate of the same dimensions. Although graphene contacts were used to reduce contact resistance, a footprint of transistors, which determines the degree of integration, were not discussed in the report.

For the real application, the scaling of contact lengths, as well as channel lengths or gate lengths, becomes equally important. First systematic study on the contact scaling showed that the contact resistance between the ideal metal (Pd) increased by several times as the contact length was scaled to similar dimensions to the channel lengths (<20 nm). A new concept of end-bonded contacts was presented as size-independent contact resistance for ultrascaled high-performance transistors, which exhibit advantages over conventional side-contacts in a sub-20 nm regime[48]. Upon such recent progress, ultrascaled carbon nanotube transistors with a 40-nm footprint was fabricated[3]. In terms of a footprint size, where the lengths of channels and both sides of contacts are included, even 7-nm-node Si and SiGe have footprints of ~60 nm. Though no data on the performance of 7-nm-node devices is available, the carbon nanotube transistor outperformed Si transistors with 10-nm-node FinFET and nanowire. These recent developments reinforce our conviction that carbon nanotubes can replace Si in high-performance computation and accelerate the further scaling.

4.1.2 Densely packed SWNT channels

Early demonstrations of SWNT-based transistors started from single SWNT channels.[49,166] However, for SWNTs to compete with and outperform silicon-based transistors, their density needs to be highly controlled. Theoretical study predicted that SWNT density as high as 250 SWNTs/μm is desirable to obtain performance gains over silicon devices in terms of .[53] Since synthesized SWNTs are usually a mixture of s- and m-SWNTs, it was difficult to use multiple SWNTs as a channel. First breakthrough for incorporating multiple SWNT channels was based electrical breakdown of unwanted SWNTs, where only m-SWNTs were oxidized with Joule-self heating in three-terminal devices (source, drain and gate).[116] Another approach was to use the low-density random networks composed of both types of SWNTs, so that the density of m-SWNTs does not exceeds the percolation threshold.[167]

Aligned growth of SWNTs on single-crystalline substrates, such as quartz[9,168] and sapphire[10,11], brought in a considerable improvement of the density and the compatibility with the electrical breakdown method. By patterning the catalysts in an isolated region, average density was increased around SWNTs/μm.[38] In addition, multiple loading of catalysts,[169] multiple-cycle growth,[170] and multiple transfer of aligned SWNTs [171] drove the density improvement forward up to ~45, 20–40, and ~100 SWNTs/μm, respectively. Recently, ultrahigh density (>130 SWNTs/μm) was achieved by a single step of synthesis using the catalyst-dissolving and -releasing processes during CVD.[57] This value reaches one of the targets for the SWNT density.[54] Remaining challenges are to improve the uniformity of inter-nanotube separation over a large area, and elimination of m-SWNTs from as-grown arrays.

For the high-performance application of SWNTs, selective removal of m-SWNTs has to keep its selectivity even when the SWNTs are densely packed. In this sense, sorting methods which sacrifice the s-SWNTs near m-SWNTs cannot be an ideal option, though some approaches achieved the ultrahigh selectivity of full-length removal between s- and m-SWNTs.[123,125,172] In contrast, a previous study showed that electrical breakdown reliably worked at the ultrahigh density arrays (~100 SWNTs/μm). However, it is also predicted that electrical breakdown will fail in ultrascaled channel lengths.[117] Very recently, a new concept for shrinking the lateral spacing of as-grown SWNT arrays was proposed to increase the density with a less risk of crossing and bundling of SWNTs, which deteriorates the electrostatic control of SWNT channels.[173]

Another ways to obtain high-density s-SWNTs is briefly described. Liquid-phase sorting of SWNTs [41] also opened the pathway to the use of high density random networks. Progresses in the preparation of aligned arrays from solution significantly increase the degree of alignment and the controllability of nanotube density.[39,40,106,174] By starting from high-purity s-SWNT solution (>99.99%), SWNT-based transistors whose current density exceeds Si and GaAs was fabricated at ~100-nm node.[31] Remaining challenges for this sort of approach are to further improve the alignment to avoid failure at ultrascaled channels,[37] to realize global alignment of bun-monolayer films, and to obtain higher purity of s-SWNT (99.9999%).

4.1.3 Large-scale integration of SWNT transistors

The third scaling requirement is the scaling to large circuits. To put this new material in practical use, billions of nanotube-based transistors have to be produced and integrated in a complex circuit. This requires ultrahigh yields and small variability among transistors. Medium-scale integrated digital circuits were successfully fabricated on flexible plastic substrates using sub-monolayer SWNT networks.[33,175] Despite the high yield over a large area, these studies employed as-grown low-density network nanotubes as channels, and therefore other approaches are necessary for high-performance (*e.g.* large current density) electronics. The use of high-purity s-SWNT solution improved the performance through the densification of SWNTs while keeping the high on/off current ratio and spatial uniformity over a large area.[176,177]

Techniques for large-scale compatible removal of m-SWNTs and the design of imperfection-immune systems drove forward the use of horizontally aligned SWNTs in large-scale.[120] Started by a first nanotube computer which was composed of 178 transistors in 2013,[119] more than one million SWNT-based inverters (logic and sensors) were integrated into three-dimensional systems together with silicon logic circuits and RRAM.[4] Since the current fabrication had to employ the electrical breakdown methods, which will fail in ultrascaled channels (<20 nm), other ways of m-SWNT removal with high reliability and the three types of scalability need to be developed to realize SWNT-based performance large-scale circuits.

4.2 Purely semiconducting SWNT arrays via full-length burning

4.2.1 Site-controlled formation of nanogaps

Horizontally aligned SWNTs were grown on r-cut quartz substrates by the alcohol CVD method [178] as described in detail elsewhere.[97] The SWNTs were transferred via polymer thin films [35] onto Si/SiO_2 substrates (100 nm thick oxide) with pre-patterned metal probing pads (Ti/Pt: 1/24 nm). Unwanted SWNTs outside the active region were etched away by oxygen plasma, followed by patterning of Au contacts (25 nm thick) directly onto the SWNT arrays. All transistors were modulated by a Si back-gate with SiO_2 as a dielectric.

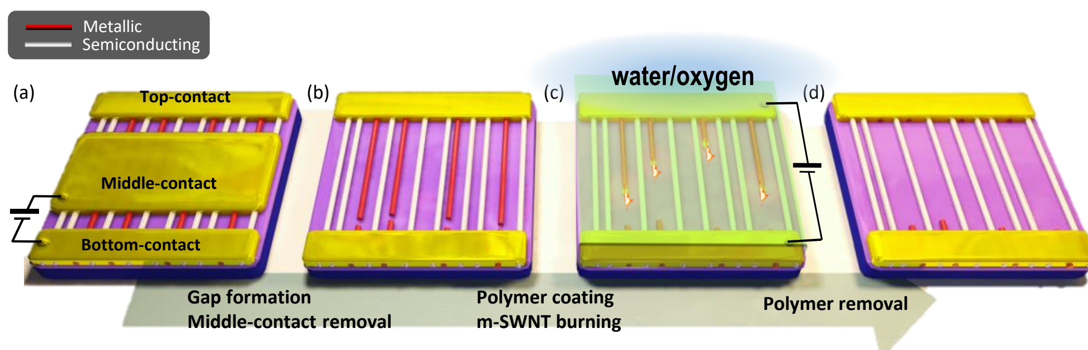

Figure 4.1 Schematics for procedures of-chip sorting of s-SWNTs from the as-grown aligned arrays. (a) SWNTs were first embedded in three Au contacts. Electrical breakdown was performed between the two (middle and bottom) contacts to form nanogaps in m-SWNTs. (b) After the gap formation, the middle contacts were selectively etched away, leaving the nanogaps near the bottom contacts (cathode). (c) Spin-coating of PMMA thin films, followed by WPA burning of m-SWNT from the pre-formed nanogaps. (d) Purely s-SWNTs remained after PMMA removal with acetone. Adapted with permission from ref.[179]. Copyright 2017 American Chemical Society.

Observations of the SWNTs were conducted using SEM (0.7–1.0 kV) and AFM. Electrical measurements of transistors were performed in air at room temperature, and all other voltage treatments were conducted in a chamber filled with pure oxygen (O_2: 90 kPa) or wet oxygen (O_2/H_2O: 90/2.4 kPa) as described elsewhere in detail.[127]

Figures 4.1(a−d) show the purification procedures for the full-length burning of m-SWNTs. Third (middle) Au contacts, as well as other two (top and bottom) contacts, were patterned on the SWNT arrays (Figures 4.1(a)) to form nanogaps in the vicinity of the bottom metal contacts, to which a lower potential was applied (cathode). A corresponding SEM image is shown in Figures 4.2(a). Electrical breakdown of the SWNTs was performed in dry oxygen environment to create as small nanogaps as possible between the middle and bottom contacts. The reason for this will be described later. Etching of the middle metal contacts with an iodine-based gold etchant left eight nanogaps in the m-SWNTs beside the bottom contacts, at the position indicated by the red circles in Figure 4.2(b). The transfer characteristics of the transistor defined by the middle and bottom contacts indicate that all the m-SWNTs were successfully broken down, as shown by the red curve in Figure 1h. The reduction of the on-state current after the removal of middle contacts (Figure 4.2(d), blue curve) is simply attributed to the change in the channel length L_{CH}, from ~2 to ~10 μm.

4.2.2 One-way burning site-controlled nanogaps

Once the nanogaps were formed, WPA burning from nanogaps, which was studied in Chapter 3, was utilized to remove any remaining m-SWNTs. The SWNT arrays (Figure 4.2(b)) were embedded in PMMA thin films by spin-coating of 1 wt% PMMA ($M_W \approx$ 996,000) solution in anisole. A ramp voltage (up to 35 V) was then applied to the SWNT arrays in a wet oxygen environment. Figure 4.2(c) shows an SEM image of the SWNT arrays after m-SWNT burning from site-controlled nanogaps and removal of the PMMA with acetone. Since burning from nanogaps occurs in the SWNTs connected to the metal contact to which a higher potential is applied (anode), SWNT fragments at the anode side of the nanogaps were eliminated. Thus, almost full lengths of the m-SWNTs were removed, except for very short fragments in the designated area

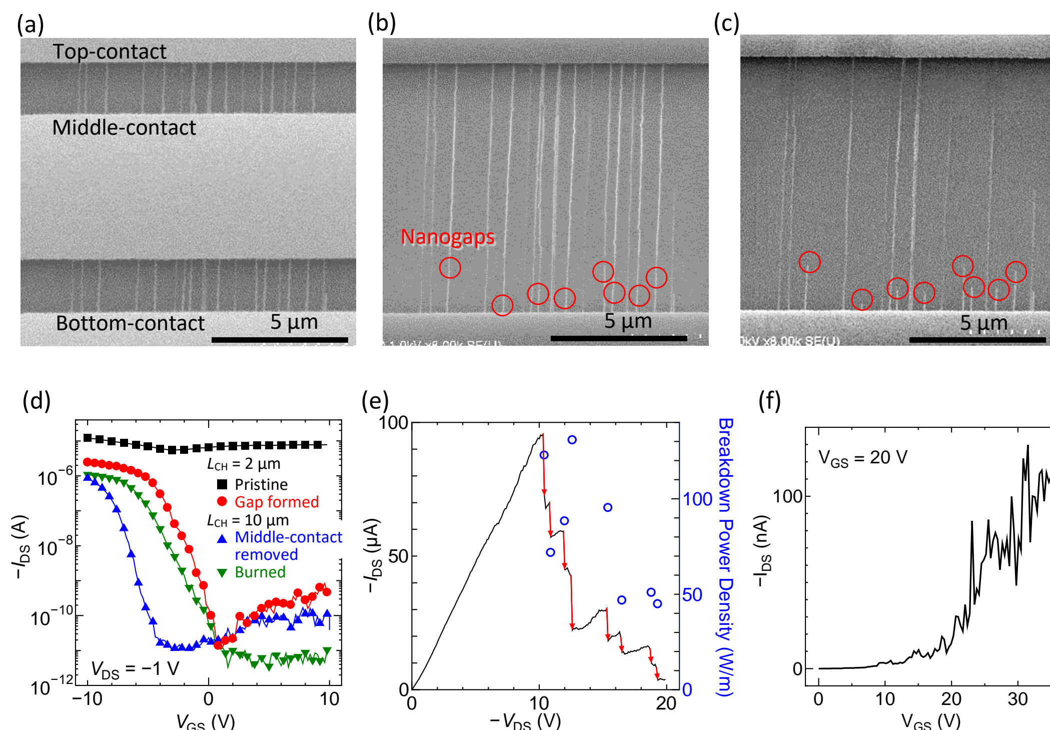

Figure 4.2 SEM images of SWNT arrays during the of-chip sorting of s-SWNTs. (a) SWNTs were first embedded in three Au contacts. Electrical breakdown was performed between the two (middle and bottom) contacts to form nanogaps in m-SWNTs. (b) After the gap formation, the middle contacts were selectively etched away, leaving the nanogaps near the bottom contacts (cathode). (c) Purely s-SWNTs remained after WPA burning of m-SWNTs and PMMA removal with acetone. (d) Transfer characteristics of transistors before and after the gap formation (black and red curves), after the burning from pre-formed nanogaps (green). (e,f) Current transition during (e) gap formation and (f) burning from the nanogaps. Adapted with permission from ref.[179]. Copyright 2017 American Chemical Society.

close to the bottom contact. Therefore a purely semiconducting SWNT array was obtained in the selected area. Note that during this purification process, SWNTs can be kept very clean because only PMMA, Au, and photoresists, which can be easily removed,[47,117] are in direct contact with the SWNTs.

The residues thinner than the original SWNTs were observed in an AFM image (not shown) after the SWNTs were burned from the nanogaps. For example, a 1-nm-thick residue remained after the burning of an SWNT with the diameter of 2 nm. To rule out the unintentional conduction through the residue, metal contacts were placed on the burned m-SWNT area. Measurement of current-voltage characteristics confirmed that this type of thin residue from the m-SWNT was not conductive.

4.3 Multiple transistors along identical array of s-SWNTs

4.3.1 Fabrication and characterization of multiple transistors

Since m-SWNTs were selectively removed in almost full length, multiple transistors are then fabricated along the s-SWNTs to discuss their performance. After dissolving the entire Au layers used for the purification process (Figure 4.3(b)), a row of metal contacts was patterned by electron beam lithography, thermal evaporation of Ti/Au (0.2/35 nm), and a lift-off process (Figure 4.3(c)). Finally, the devices were annealed at 230°C in air for 1 h to improve the contact between the SWNTs and the metal. Figure 4.3(d) shows a false-colored SEM image of fabricated transistors with various channel lengths (200–960 nm).

Figure 4.3(e) shows the transfer characteristics of five transistors on the same SWNT array. All the transfer characteristics of SWNT transistors show excellent switching behavior, which confirms again that no m-SWNTs remained in the region where the transistors were fabricated. Figure 4.3(f) shows that the on-state current I_{ON} increased linearly with a reduction in the channel length, while the on/off ratio I_{ON}/I_{OFF} remained almost constant (~10^5). This indicates that the s-SWNT array was uniform along the axis, as the long SWNT arrays were originally used after the removal of m-SWNTs.

There are nine s-SWNTs in the channel, so that the averaged conductance of each s-SWNT was calculated to be 4.6 μS, which is the same order as that of previously reported devices with a single as-grown s-SWNT and similar dimensions [180] (see also Figure 4.9). The conductance can be improved by further vaporizing the polymer (PMMA and resists) residue before patterning of the metal contacts. It should be stressed that although only five transistors were fabricated in this experiment due to the constraint of measurement setup and device structure, the number of transistors fabricated on the s-SWNT array could be increased much by reducing the device dimensions. This method will therefore enable device integration with ultrasmall channel/contact length and freedom of circuit design in contrast to the electrical breakdown method.[120]

4.3.2 Potential for channel scaling

Half-lengths of m-SWNTs were intentionally removed, for the preparation of both purified and unpurified SWNT arrays from the identical set of long SWNTs, as shown

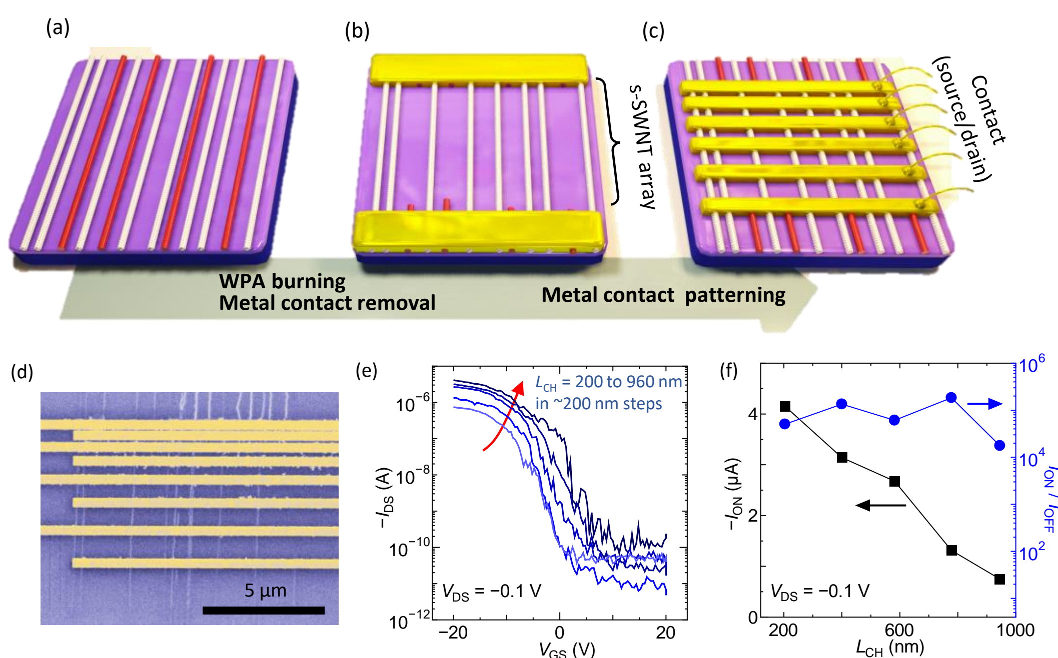

Figure 4.3 (a-c) Schematics for the fabrication of multiple transistors from the fabricated s-SWNT array. (a) Before and (b) after the m-SWNT removal procedure. (c) Schematic and (d) false-colored SEM image of the transistor array fabricated from the s-SWNT array. (e) Transfer characteristics of five transistors with different channel lengths. (f) On current I_{ON} (left axis), and on/off ratio I_{ON}/I_{OFF} (right axis), as a function of the channel length, L_{CH}. V_{DS} = −0.1 V. Adapted with permission from ref.[179]. Copyright 2017 American Chemical Society.

in Figures 4.4. Since the unpurified SWNT array was not subjected to any voltage application, the effect of the purification process on the SWNTs could be directly evaluated through the fabrication and characterization of transistors with the exact same dimensions on purified and unpurified arrays.

In Figure 4.4(c), transistors on the unpurified array (black curves) show typical characteristics of short circuits caused by m-SWNT impurities, while those on the purified array (red curves) reflect purely semiconducting behavior. Therefore, the purification process increased the on/off ratio from <10 to ~10^4, as shown in Figure 4.4(d). From the data with L_{CH} = 200 nm in Figure 4.4(e), the reduction in the on-state current induced by purification was ~70%, which is quite modest considering that m-SWNTs conduct more current than s-SWNTs.[181] In both types of transistors, the on-state current was increased with a reduction in the channel length because the SWNT arrays were uniform along the axis.

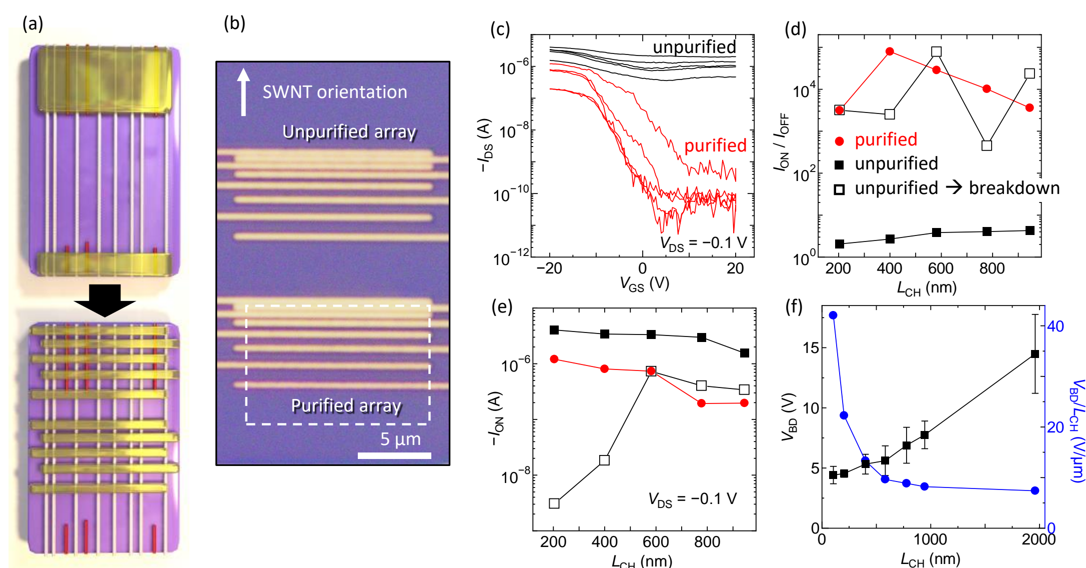

Figure 4.4 Comparison between transistors fabricated from purified and unpurified SWNT arrays. (a) Schematic for the preparation of purified and unpurified arrays originally from identical SWNTs. (b) Optical image of two transistor arrays fabricated from purified (bottom) and unpurified (top) SWNT arrays. (c) Transfer characteristics of the transistors fabricated from purified (red) and unpurified (black) arrays. (d) On/off ratio I_{ON}/I_{OFF} for the transistors on the purified array (red circles) as a function of the channel length L_{CH}. Plots for the transistors before and after electrical breakdown of the transistors fabricated from the unpurified array (black and open squares, respectively). (e) Similar set of plots for channel length L_{CH} vs. on current I_{ON}. (f) Channel length L_{CH} vs. breakdown voltage V_{BD}. Adapted with permission from ref.[179]. Copyright 2017 American Chemical Society.

Conventional electrical breakdown [116] was performed on individual transistors on unpurified arrays for comparison with those obtained via full-length WPA burning. All the transistors tested here were composed of the same set of SWNTs. The electrical breakdown method has shown its applicability in the fabrication of digital systems using CVD-grown SWNT arrays by combining design and processing,[119] even when the SWNT density exceeds 100 tubes/μm.[117] However, the method is quite sensitive to channel length and is expected to fail in ultrascaled devices.[121] A ramp voltage (V_{DS}) was applied to the transistors on the unpurified array until the on/off ratio reached 10^3, while s-SWNTs were turned off by gate. For the longer channel devices ($L_{CH} \geq$ 600 nm), on-state current retention was comparable for both the WPA burned devices and the electrical breakdown devices, as shown in Figure 4.4(e). On the other hand, the on-state current was significantly degraded when the channel was scaled further (L_{CH} $\leq$ 400 nm). Therefore, our fabrication procedure, where m-SWNTs are completely removed from long SWNT arrays and then source and drain contacts are defined on the semiconducting arrays, is more beneficial than conventional electrical breakdown for a reduction in device dimensions without sacrifice of the on-state current.

The large degradation of the on-state current by electrical breakdown can be explained in terms of heat dissipation and electrostatic problems at the gate. First, a higher electric field (V_{DS}/L_{CH}) is required to cut shorter SWNTs (Figure 4.4(f)) because axial heat sinking to metal contacts, rather than to the substrate below, becomes predominant for short-channel devices[122] (see also Figure 4.5(b) for calculated temperature profiles). This increases the off-state current in s-SWNTs significantly by the time the m-SWNTs are broken down. Second, gate control becomes weak as the channel is scaled due to so-called short-channel effects. The off-state current is increased because of this effect, even at the same voltage. These two effects reduce the difference in the breakdown voltage of s- and m-SWNTs (Figure 4.5(d)), which restricts the use of the electrical breakdown method in scaled devices. Note that the present devices were not optimized in terms of gate electrostatics, and have much room for reduction of the off-state current in s-SWNTs during the electrical breakdown process.

4.3.3 Thermal properties during electrical breakdown of short SWNTs

In order to investigate the reason why electrical breakdown failed in short-channel devices, analytical calculation [148] was conducted for temperature of SWNTs with various lengths. Thermal conductivity of the SWNT was assumed to be 1,000 W/mK and Joule heating was uniform and the same for all the case. Since the metal contacts on both sides of the SWNT remain almost at room temperature, heat flux to the contacts strongly affects the temperature profile along axis. As SWNT length become shorter, the highest temperature decreases (Figure 4.5(b)), which means higher field (voltage per certain length) is needed to break m-SWNTs.

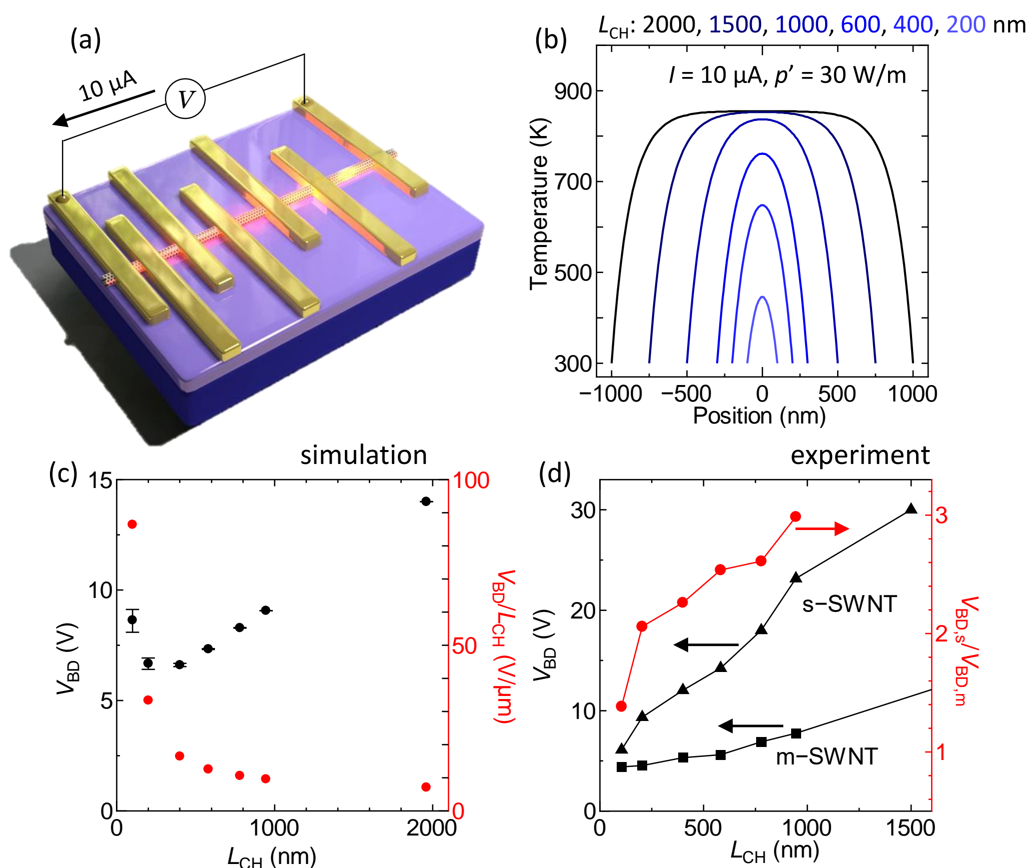

Figure 4.5 (a) Schematic for analyzed SWNT devices with various lengths heated by uniform Joule heating along the axis. (b) Analytical temperature profiles of SWNTs of various lengths. (c) Channel lengths vs simulated breakdown power V_{BD} (left axis) and equivalent electric field (V_{BD}/L_{CH}) (right axis). (d) Breakdown voltage V_{BD} vs channel lengths L_{CH} for s- and m-SWNTs (left axis). Red circles represent the V_{BD} ratio of s-SWNT to m-SWNT (right axis). Adapted with permission from ref.[179]. Copyright 2017 American Chemical Society.

A numerical simulation for the breakdown voltage (voltage needed to heat SWNTs up to 600°C) was also performed as shown in Figure 4.5(c). Here, electrical contact resistance (voltage drop at the contacts with metal) and temperature dependence [142] of thermal conductivity of SWNTs are taken into account, and other simulation details are described elsewhere.[127] The simulation result showed a similar trend to the experiment shown in Figure 4.4(f). Here, error bars here represent the change in breakdown voltage when the thermal conductivity of SWNTs increases/decreases by 10%.

Figure 4.5(d) shows the breakdown voltage V_{BD} of s- and m-SWNTs of various lengths. Although the s-SWNT was broken down at higher bias than m-SWNTs, the difference of V_{BD} ($V_{BD,s}/V_{BD,m}$, red circles on right axis) became small as channel lengths L_{CH} were reduced. This indicates the low selectivity of removal between s- and m-SWNTs for scaled devices.

4.3.4 Suppressed damage to s-SWNTs

It should be stressed that the purification process that involves the pre-formation of nanogaps caused little damage to the s-SWNTs. In a control experiment, the on-state conductance (at V_{DS} = −1 V) of the s-SWNTs was gradually decreased when a large V_{DS} bias (>5 V/μm) was applied, especially when the s-SWNTs were under the PMMA

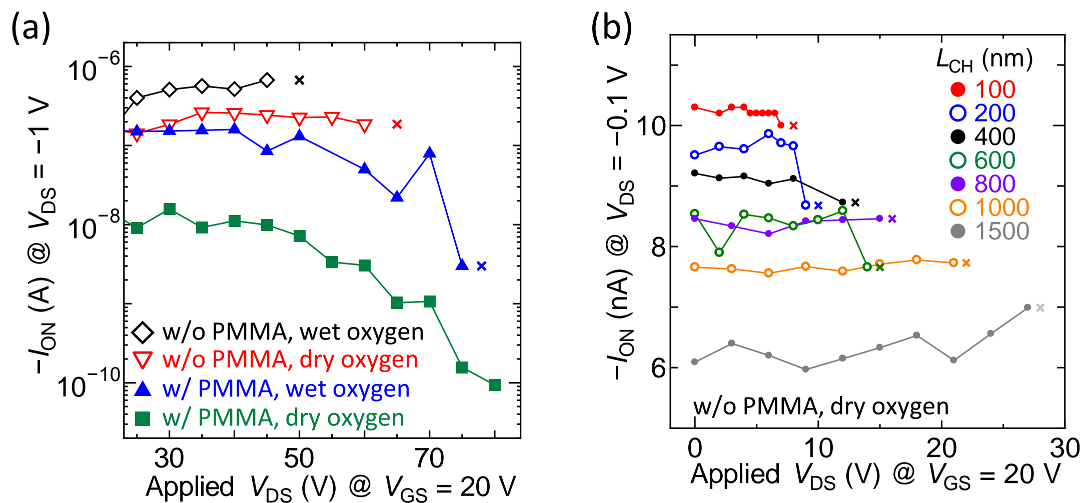

Figure 4.6 (a) Transition of on-state current in single s-SWNT transistors embedded under various conditions (with or without PMMA coating, gas environments). Crossed marks represent the breakdown of SWNTs during next voltage application. L_{CH} = 10 μm. (b) Similar data obtained in dry oxygen without PMMA coating for the transistors with different channel lengths. The current dropped before electrical breakdown for short channel lengths.

films. Figure 4.6(a) shows transition of on-state current of transistors with as-grown 10-μm-lomg s-SWNT channels in various conditions. Two types of damages to the s-SWNTs were observed here; (1) heat-induced damage which physically cuts the SWNTs when I_{DS} was too large (>1 μA in this experiment) and (2) high field-induced damage. Heat-induced damage suddenly appears as electrical breakdown (represented by crossed marks) without showing any degradation beforehand. On the other hand, the transistors showed gradual decrease in on-state conductance prior to the breakdown, especially when s-SWNTs were in the PMMA thin films and V_{DS} exceeded ~50 V (5 V/μm). This indicates that nanogaps formation in the designated region prior to the burning prevented s-SWNTs from the filed-induced degradation during the purification.

A similar experiment was conducted for the transistors with various channel lengths located on a single, identical s-SWNT in dry oxygen with no PMMA coating. As shown in Figure 4.6(b), on-state current showed deterioration just before electrical breakdown for the transistors with small L_{CH}, consistent with the result shown in Figure 4.4(e). This is probably because higher field was needed to break s-SWNTs for shorter-channel devices due to large heat dissipation to metal contacts. This indicates that the electric field rather than Joule heating was responsible for the gradual degradation of s-SWNT conductance.

In the first electrical breakdown process in the full-length removal of m-SWNTs, most of the SWNTs, which are embedded in Au contacts, were not subjected to a high electric field. In the subsequent burning process, the on-state current of the transistor defined by the top and bottom contacts did not decrease as shown by the blue and green curves in Figure 4.2(d). This is because the burning from pre-formed nanogaps can be triggered by the application of a low voltage (35 V), which is much lower than the electrical breakdown voltage (~70 V for 10-μm-long SWNTs by the extrapolation of Figure 4.4(f)). Therefore, the selectivity for the removal of s- or m-SWNTs is dominated by the initial electrical breakdown to form nanogaps, which is almost high enough for logic applications (>99.99%).[118] Furthermore, the voltage required to trigger the burning is independent of the SWNT length due to field localization within the nanogaps, and thus breakdown of the gate dielectric can be avoided even when the purification process is scaled up.

According to a basic heat transfer theory, when L_{CH} = 1.5 μm or more, the temperature profile along the tube axis is uniform in the middle (Figure 4.5(b)), and is not affected by heat dissipation to the metal contacts. Therefore, the selectivity of removal between s- and m-SWNTs is sufficiently high for devices with $L_{CH} \geq 1.5$ μm, which is clear from the almost constant breakdown field (V_{BD}/L_{CH}) shown in Figure 4.4(f). To further scale up the purification process and reduce the area ratio of unpurified to purified arrays, the distance between anodes and cathodes for the burning process should be increased while all SWNTs are kept connected to both metal contacts. Since the proposed mode for SWNT burning suggests a self-sustained burning without a limit of length,[127] the growth of long SWNTs is a key to further improve the process.

4.3.5 Applicable to high-density arrays?

When the sorting technique is applied to high-density SWNT arrays, deterioration of the selectivity caused by inter-tube interaction, *i.e.*, the influence of the burning SWNTs on other SWNTs in the vicinity, can be a concern. There are two possible ways of damage to intact s-SWNTs; voltage-induced tip-to-wall etching and wall-to-wall spreading of chemical reaction via PMMA. The author examined the minimum inter-SWNT spacing for which m-SWNTs burned from nanogaps and caused no damage to neighboring s-SWNTs, and the results are shown in Figure 4.7. With respect to the first type of damage, the experimental result shows that an s-SWNT 60-nm away from the tip of a broken m-SWNT did not burn down, even when 50 V was applied to burn the m-SWNT (Figure 4.7(a), bottom). In addition, the burning of the m-SWNT did not propagate to the s-SWNT when the minimum inter-SWNT distance was as small as 40 nm (Figure 4.7(a), top). This implies that this method can be applied to SWNT arrays with a density of 16 SWNTs/μm or more.

In contrast, when a nanogap was located close to the anode, an s-SWNT 120-nm away from the nanogap was burned away, even with application of a smaller voltage (40 V), as shown in Figure 4.7(b). This is because the difference in the electric potential between the m-SWNT tip and the s-SWNT wall was greater, as schematically shown in Figure 4.7(d). This implies that burning from site-controlled nanogaps near the

cathode is also beneficial to avoid unintentional damage to neighboring s-SWNTs, and is thus applicable to higher-density SWNT arrays.

There are two possible damages to s-SWNTs during the burning of m-SWNTs. Tip-to-wall damage is electrochemically induced[131] because of field enhancement between the tip of m-SWNTs and sidewall of adjacent s-SWNTs. On the other hand, wall-to-wall damage is caused by chemical reaction of the polymer mediating two SWNTs. Extreme case of this damage occurs when m-SWNTs and s-SWNTs are bundled.[128] Figure 4.7(b) shows the burning from nanogaps located near the anode, to which higher potential was given during the burning of m-SWNTs. Although only 40 V was applied to trigger the burning of the middle m-SWNT, an s-SWNT ~120 nm away from the tip (nanogap) of the m-SWNT was also burned.

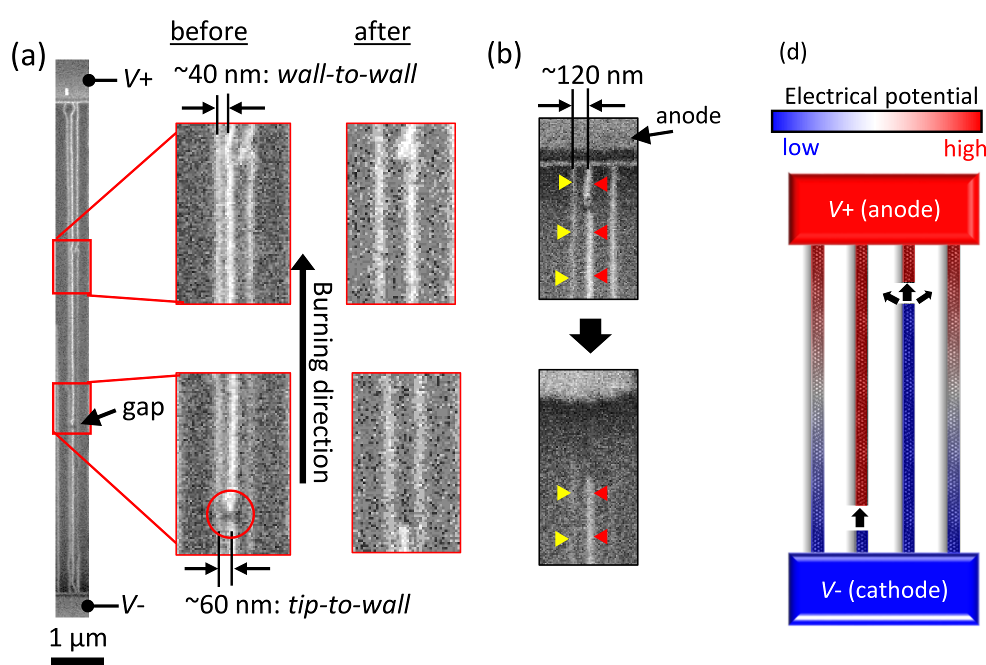

Figure 4.7 (a) SEM image of three parallel SWNTs after gap formation by electrical breakdown of the middle SWNT. Enlarged images of two regions before and after burning of the middle SWNT under WPA conditions by the application of 50 V are also shown. s-SWNTs were kept intact, though the minimum tip-to-wall and wall-to-wall distance in these SWNTs were 60 and 40 nm, respectively. (b) SEM images of s-SWNTs and an m-SWNT with a nanogap formed nearby the anode before (top) and after (bottom) the burning by the application of 40V. A neighboring s-SWNT was also burned. (c) Schematic of the electric potential for different gap positions (near anode or cathode). Adapted with permission from ref.[179]. Copyright 2017 American Chemical Society.

The values presented above (40, 60 nm) are not the lower limit of inter-tube spacing with which s-SWNTs remain unaffected. A straightforward way to investigate the lower limit is to prepare SWNT arrays with various inter-tube spacing down to <10 nm (desirable density is >100 SWNTs/μm). However, growth of such high-density SWNTs and maintaining the inter-tube distance without forming bundles is not easy because the SWNTs have to be transferred from crystalline quartz substrates for gate control unless a top gate configuration is available. Instead, a simple model is presented to describe the damage to s-SWNTs given by m-SWNT nanogaps based on field enhancement at the SWNT tips introduced in the last section. Upon the assumption that the burning from nanogaps is triggered by field emission and anode etching due to field enhancement at the SWNT tip, the author roughly estimated the upper limit of the density of SWNTs to which this purification method can be applied without sacrificing s-SWNTs. By ignoring the difference of field enhancement between tip-to-tip and tip-to-wall configurations for simplicity, the field enhancement factor γ at SWNT tips can be expressed in a similar manner to a previous study[131] about the field enhancement on substrates as below,

$$\gamma = c\left(1+\sqrt{\frac{2L_{\mathrm{cathode}}}{4r}}\right)\left(1+a\frac{2L_{\mathrm{cathode}}+s_{inter}}{s_{\mathrm{inter}}}-b\frac{s_{\mathrm{inter}}}{2L_{\mathrm{cathode}}+s_{inter}}\right), \tag{4.1}$$

where a, b, and c are constants and taken from the previous study,[131] L_{cathode} is the length of broken m-SWNTs connected to the cathode, s_{inter} is the inter-tube spacing, and r is a tube radius. Since the electric potential of unbroken s-SWNTs has a gradient along the axis, the voltage difference V_{inter} between the tip of anode m-SWNTs and the wall of the other side of s-SWNTs is written as $V_{\mathrm{inter}} = V_{\mathrm{DS}}L_{\mathrm{cathode}}/L_{\mathrm{CH}}$. If the threshold field at the SWNT tips for initiating the burning is constant ($F_{\mathrm{th}} = \gamma V_{\mathrm{inter}}/(2L_{\mathrm{cathode}}+s_{\mathrm{inter}})$) and can be estimated from the burning occurring at tip-to-tip, where typically ~30 V was necessary to burn m-SWNTs from 70-nm-nanogaps, the threshold voltage that causes the m-SWNT-induced burning of s-SWNTs ($V_{\mathrm{s\text{-}burn}}$) is obtained as below,

$$V_{\mathrm{s-burn}}(L_{\mathrm{cathode}}, s_{\mathrm{inter}}) = \frac{F_{\mathrm{th}}(2L_{\mathrm{cathode}}+s_{\mathrm{inter}})}{\gamma}\times\frac{L_{\mathrm{CH}}}{L_{\mathrm{cathode}}}. \tag{4.2}$$

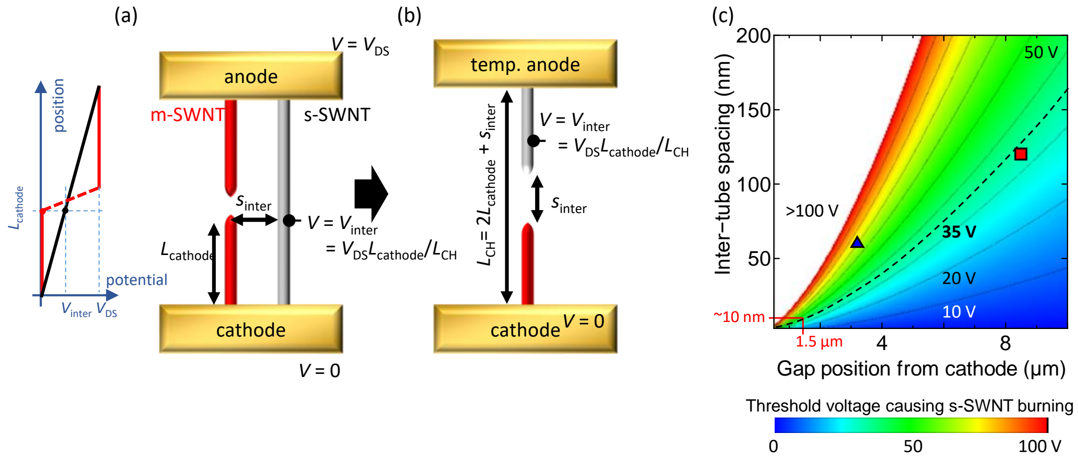

Figure 4.8 Schematics for (a) the configuration of SWNTs of interest, and (b) the simplified tip-to-tip configuration to estimate the damage to s-SWNTs induced by m-SWNT nanogaps with a separation of s_{inter}. Unbroken s-SWNT in (a) has a gradient along the axis, and an s-SWNT in (b) is assumed to have the same potential (=$V_{DS}L_{cathode}/L_{CH}$) as the point closest to the m-SWNT nanogap. (c) (d) Color contour plot of the calculated threshold voltage that unintentionally causes the burning of s-SWNTs, as a function of gap position (x-axis) and inter-tube spacing (y-axis). Two examples from Figure 4.7 are plotted in a blue triangle and a red square, respectively. Adapted with permission from ref.[179]. Copyright 2017 American Chemical Society.

Figure 4.8(c) shows a color contour plot of the voltage calculated by Equation 4.2 when the L_{CH} for the burning process is 10 μm (similar to Figure 4.2). The examples of the nanogaps shown in Figure 4.7(a) and (b) are plotted as a blue triangle ($V_{s\text{-}burn} \approx 67$ V $> V_{DS} = 50$ V) and a red square ($V_{s\text{-}burn} \approx 32$ V $< V_{DS} = 40$ V), respectively, which suggests this simple modeling is consistent with the experimental results. V_{DS} for triggering the m-SWNT burning has to be smaller than $V_{s\text{-}burn}$ to avoid the undesirable removal of s-SWNTs. Since the channel length for the first nanogap formation process can be reduced down to 1.5 μm while keeping the selectivity of breaking m-SWNTs high enough, the inter-tube spacing can be reduced to ~10 nm without sacrificing s-SWNTs under the application of V_{DS} = 35 V (a dashed line in Figure 4.8(d)). This implies the sorting method of s-SWNTs could effectively work for the SWNT arrays with density up to ~100 SWNTs/μm owing to the control of gap position. Note that it is assumed that ~70-nm-nanogaps are formed by the breakdown of 99.99% (within four standard deviations) m-SWNTs with V_{DS} = 20 V, and then the m-SWNTs are burned by the further application of V_{DS} = 35 V (as in Figure 4.2). Scaling up of the purification process (which corresponds to larger L_{CH} in Equation 4.2) is also beneficial in further

reducing the inter-tube spacing. Therefore, the sorting method in combination with selective growth of long and high-density s-SWNT arrays[57,182,183] opens the possibility of the practical use of SWNT transistors in large-scale and high-performance logic circuits.

4.3.6 On-state conductance per tube

Transistors with various channel lengths L_{CH} were also fabricated along single as-grown SWNTs as shown in Figure 4.9(a). Among the three SWNTs (one metallic and two semiconducting tubes), the transfer curves of the transistors on the best SWNT are shown in Figure 4.9(b), which indicate the contact resistance of $2R_c$ = 13 kΩ and on-state conductance of 18 μS at L_{CH} = 200 nm. On the other hand, other two SWNTs fabricated simultaneously had lower on-state conductance of 2.8 and 1.3 μS at the same dimension. This variation probably comes from imperfect fabrication process, such as quality of contact metals and residues on SWNTs. From this point of view, the average on-state conductance per tube (= 4.6 μS) after the burning of m-SWNTs (Figure 4.3(f)) is comparable to the unprocessed as-grown SWNTs.

Although the s-SWNT array sorted by full-length WPA burning of m-SWNTs has as large conductance as the unprocessed individual SWNTs, it is still much lower than the reported highest value with the similar dimension.[103] Since the SWNTs in this study were imaged with SEM many times for the record, the device performance might

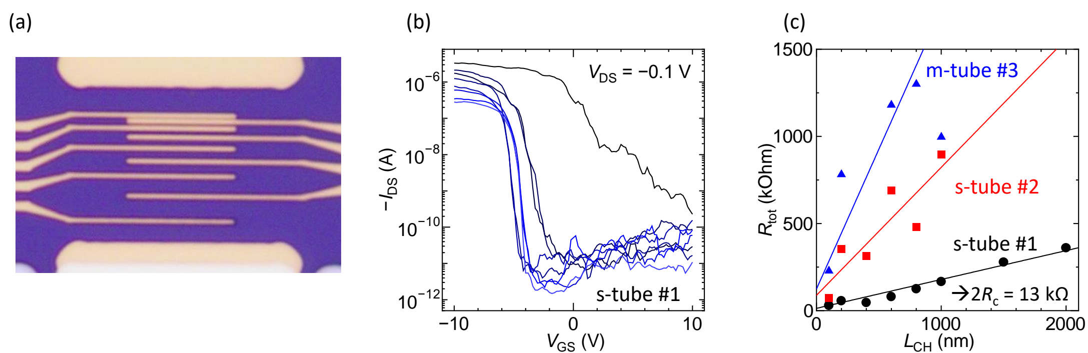

Figure 4.9 (a) Optical image of transistors built along an identical SWNT with various channel lengths. (b) Transfer curves of s-tube transistor (L_{CH} = 100, 200, 400, 600, 800, 1000, 1500, and 2000 nm). (c) Channel length L_{CH} vs on-state resistance R_{tot} for two s-SWNTs and an m-SWNT grown on the same chip. The best s-SWNT showed the contact resistance of $2R_c$ = 13 kΩ, though other SWNTs showed much higher resistance.

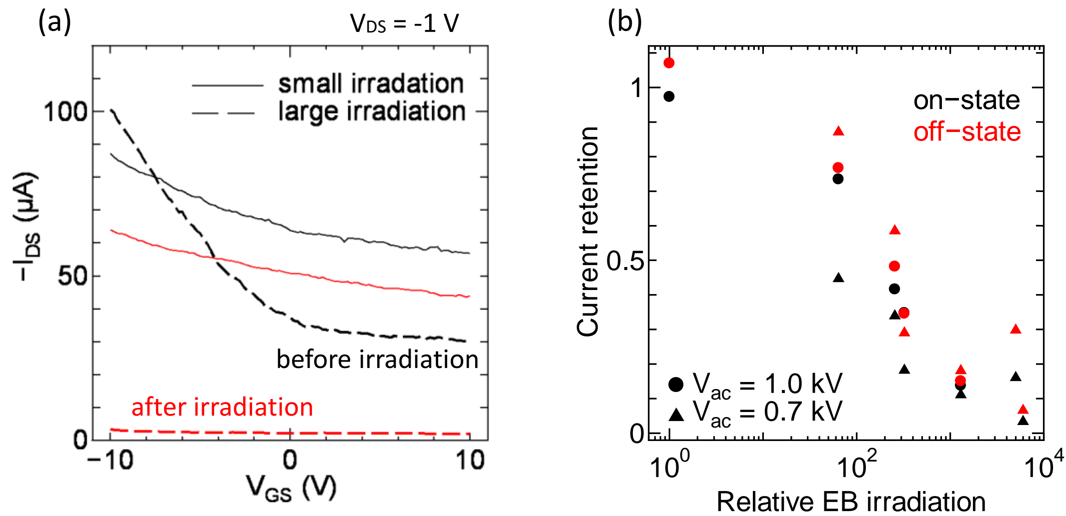

Figure 4.10 (a) Transfer curves of transistors before (black) and after (red) SEM imaging with small (solid line) and large (dashed line) does of electron beam. The transistors contained s- and m-SWNTs. (b) Current retention of on-state (black) and off-state (red) of transistors after different amount of electron beam irradiation. Relative EB irradiation (*x*-axis) is normalized by a dose of 1.06×10^{19} C/cm^2.

be affected by electron beam irradiation during SEM imaging. To assess this effect in our experiments, SWNT transistors were fabricated without any sorting processes (electrical breakdown or WPA burning), and transfer characteristics were measured. The SWNT transistors was imaged by SEM for various lengths of time and magnifications, and measured transfer characteristics again. This clearly shows that larger dose of EB irradiation resulted in smaller current both for on-state and off-state. Since the SWNT arrays shown in Figure 4.3 went through at least four times of 20 s irradiation with ×8000 magnification (corresponding to relative EB irradiation of 256 in Figure 4.10(b)), the conductance of the devices in the presented article was probably deteriorated by EB irradiation.

Chapter 5:

Conclusions

5.1 Conclusions

The thesis is concluded from three points of view; synthesis, purification, and fabrication of transistors. First, a novel isotope labeling method with digital coding was proposed to trace a variety of the growth processes of horizontally aligned individual SWNTs. By periodically switching the fraction of ^{13}C ethanol in four different levels, binary-like codes were embedded in SWNTs. The programmed sequence of the digital-coded isotope labels identify time-resolved growth evolution of individual long SWNTs (>100 μm), including the information about growth rate, incubation time, lifetime, and even pause time. The SWNTs usually started growing after certain times of incubation, and were elongated without changing the growth rate until abrupt termination. One exception of non-constant growth rate along an SWNT was spontaneous chirality change *via* an intramolecular junction. The growth under modulated conditions was also traced, such as temperature and the partial pressure of carbon feedstocks, resulting in the finding of unusual phenomena, such as the growth suspension induced by sudden increase of ethanol pressure.

In chapter 3, the water- and polymer-assisted burning of m-SWNTs towards the formation of s-SWNT arrays was presented. The addition of water vapor to the system significantly enhanced the oxidation rate of SWNTs, which led to self-sustained burning of the SWNTs. This phenomenon was studied by means of experiments and simulations. One-way burning from nanogaps formed at random location to the anode side resulted in the residual m-SWNT segments near one side. As a possible trigger of the one way burning, voltage-driven gap extension phenomena for SWNTs was found and studied. The gap extension clearly showed one-directionality and dependence on the applied voltage and humidity. The *I*-*V* characteristics of single gap devices in vacuum indicated FN tunneling features. Electrochemical oxidation and charge

transfer via field emission are thus possible driving forces of SWNT gap extension and therefore the one-way burning with the assistance of polymer coating and water vapor.

Based on the knowledge obtained in Chapter 3, fabrication of multiple transistors on a long purely s-SWNT array was demonstrated via the on-chip purification method. An s-SWNT array was obtained by selective burning of m-SWNTs in full length from as-grown aligned SWNTs with the assistance of water vapor and polymer coating. Since burning from site-controlled nanogaps was triggered by the application of a relatively low voltage, there was negligible damage to s-SWNTs through the sorting process. All the transistors fabricated along the purified array showed superb switching behavior and larger on-state currents than those processed by conventional electrical breakdown for short-channel devices. The simple modeling of field enhancement at SWNT tips implied the applicability to the arrays with ~100 SWNTs/μm density. Therefore, the sorting method satisfices three kinds of scaling, *i.e.* scaling to large circuits, short channel lengths, and small inter-SWNT spacing, hopefully leading to the upscaled integration of ultrascaled SWNT transistors for high-performance logic applications.

5.2 Prospects

The digital isotope labeling has just demonstrated the simple experiments to figure out hidden mechanisms in the growth process of SWNTs. Compatibility of this technique with other growth conditions will open a chance to restudy and improve the methods found in literatures. Since it was found tube chirality (n,m) does not uniquely determined the growth behavior of the SWNTs, there must be hidden but important factors that govern the nanotube growth. Therefore, other promising opportunities for future work include the quest for hidden parameters (*e.g.* catalysts) governing the SWNT growth, in conjunction with other characterization methods, such as TEM and nanoscale optical spectroscopy. These studies can provide detailed information on catalyst structure and tube/catalyst interfaces, and thus accelerate the understating on the growth process and in turn synthetic approaches.

In addition, the isotope technique can be used to probe the origin of the selectivity of SWNTs structures (chirality, length and so on). For example, by changing feedstock

composition with time during CVD and linking the growth initiating time and the tube characteristics, systematic studies can be performed significantly efficiently. Comparison of a variety of catalysts through the labeling method may accelerate the understanding on the growth mechanism.

If the controlled synthesis of SWNTs is further developed, the burning-based sorting methods should be applied to the grown SWNT arrays to produce high-density purely s-SWNT arrays over a large area. Once it is realized, the s-SWNT arrays can be excellent starting materials to build large-scale circuits of ultrasmall SWNT transistors.

Bibliography

[1] S. Iijima and T. Ichihashi, "Single-shell carbon nanotubes of 1-nm diameter," *Nature* **363**, 603 (1993).

[2] C. Qiu, Z. Zhang, M. Xiao, Y. Yang, D. Zhong, and L.-M. Peng, "Scaling carbon nanotube complementary transistors to 5-nm gate lengths," *Science* **355**, 271 (2017).

[3] Q. Cao, J. Tersoff, D. B. Farmer, Y. Zhu, and S. Han, "Carbon nanotube transistors scaled to a 40-nanometer footprint," *Science* **356**, 1369 (2017).

[4] M. M. Shulaker, G. Hills, R. S. Park, R. T. Howe, K. Saraswat, H.-S. P. Wong, and S. Mitra, "Three-dimensional integration of nanotechnologies for computing and data storage on a single chip," *Nature* **547**, 74 (2017).

[5] S. Iijima, "Helical microtubules of graphitic carbon," *Nature* **354**, 56 (1991).

[6] D. S. Bethune, C. H. Kiang, M. S. de Vries, G. Gorman, R. Savoy, J. Vazquez, and R. Beyers, "Cobalt-catalysed growth of carbon nanotubes with single-atomic-layer walls," *Nature* **363**, 605 (1993).

[7] T. Guo, P. Nikolaev, A. Thess, D. T. Colbert, and R. E. Smalley, "Catalytic growth of single-walled manotubes by laser vaporization," *Chem. Phys. Lett.* **243**, 49 (1995).

[8] Y. Murakami, S. Chiashi, Y. Miyauchi, M. Hu, M. Ogura, T. Okubo, and S. Maruyama, "Growth of vertically aligned single-walled carbon nanotube films on quartz substrates and their optical anisotropy," *Chem. Phys. Lett.* **385**, 298 (2004).

[9] C. Kocabas, S.-H. Hur, A. Gaur, M. A. Meitl, M. Shim, and J. A. Rogers, "Guided Growth of Large-Scale, Horizontally Aligned Arrays of Single-Walled Carbon Nanotubes and Their Use in Thin-Film Transistors," *Small* **1**, 1110 (2005).

[10] H. Ago, K. Nakamura, K. Ikeda, N. Uehara, N. Ishigami, and M. Tsuji, "Aligned growth of isolated single-walled carbon nanotubes programmed by atomic arrangement of substrate surface," *Chem. Phys. Lett.* **408**, 433 (2005).

[11] A. Ismach, L. Segev, E. Wachtel, and E. Joselevich, "Atomic-Step-Templated Formation of Single Wall Carbon Nanotube Patterns," *Angew. Chemie* **116**, 6266 (2004).

[12] H. Kataura, Y. Kumazawa, Y. Maniwa, I. Umezu, S. Suzuki, Y. Ohtsuka, and Y. Achiba, "Optical properties of single-wall carbon nanotubes," *Synth. Met.* **103**, 2555 (1999).

[13] D. Li, J. Zhang, Y. He, Y. Qin, Y. Wei, P. Liu, L. Zhang, J. Wang, Q. Li, S. Fan, and K. Jiang, "Scanning electron microscopy imaging of single-walled carbon nanotubes on substrates," *Nano Res.* **10**, 1804 (2017).

[14] Y. Homma, S. Suzuki, Y. Kobayashi, M. Nagase, and D. Takagi, "Mechanism of bright selective imaging of single-walled carbon nanotubes on insulators by scanning electron microscopy," *Appl. Phys. Lett.* **84**, 1750 (2004).

[15] R. Senga, T. Pichler, and K. Suenaga, "Electron spectroscopy of single quantum objects to directly correlate the local structure to their electronic transport and optical properties," *Nano Lett.* **16**, 3661 (2016).

[16] W. Bauhofer and J. Z. Kovacs, “A review and analysis of electrical percolation in carbon nanotube polymer composites,” *Compos. Sci. Technol.* **69**, 1486 (2009).

[17] A. Yu, P. Ramesh, X. Sun, E. Bekyarova, M. E. Itkis, and R. C. Haddon, “Enhanced thermal conductivity in a hybrid graphite nanoplatelet - Carbon nanotube filler for epoxy composites,” *Adv. Mater.* **20**, 4740 (2008).

[18] F. H. Gojny, M. H. G. Wichmann, U. Köpke, B. Fiedler, and K. Schulte, “Carbon nanotube-reinforced epoxy-composites: Enhanced stiffness and fracture toughness at low nanotube content,” *Compos. Sci. Technol.* **64**, 2363 (2004).

[19] L. Xiao, Z. Chen, C. Feng, L. Liu, Z.-Q. Bai, Y. Wang, L. Qian, Y. Zhang, Q. Li, K. Jiang, and S. Fan, “Flexible, Stretchable, Transparent Carbon Nanotube Thin Film Loudspeakers,” *Nano Lett.* **8**, 4539 (2008).

[20] N. Behabtu, C. C. Young, D. E. Tsentalovich, O. Kleinerman, X. Wang, A. W. K. Ma, E. A. Bengio, R. F. Ter Waarbeek, J. J. De Jong, R. E. Hoogerwerf, S. B. Fairchild, J. B. Ferguson, B. Maruyama, J. Kono, Y. Talmon, Y. Cohen, M. J. Otto, and M. Pasquali, “Strong, light, multifunctional fibers of carbon nanotubes with ultrahigh conductivity,” *Science* **339**, 182 (2013).

[21] B. J. Landi, M. J. Ganter, C. D. Cress, R. A. DiLeo, and R. P. Raffaelle, “Carbon nanotubes for lithium ion batteries,” *Energy Environ. Sci.* **2**, 638 (2009).

[22] D. N. Futaba, K. Hata, T. Yamada, T. Hiraoka, Y. Hayamizu, Y. Kakudate, O. Tanaike, H. Hatori, M. Yumura, and S. Iijima, “Shape-engineerable and highly densely packed single-walled carbon nanotubes and their application as super-capacitor electrodes,” *Nat. Mater.* **5**, 987 (2006).

[23] Y. Li, W. Zhou, H. Wang, L. Xie, Y. Liang, F. Wei, J.-C. Idrobo, S. J. Pennycook, and H. Dai, “An oxygen reduction electrocatalyst based on carbon nanotube–graphene complexes,” *Nat. Nanotechnol.* **7**, 394 (2012).

[24] G. Li, F. Wang, Q. Jiang, X. Gao, and P. Shen, “Carbon Nanotubes with Titanium Nitride as a Low-Cost Counter-Electrode Material for Dye-Sensitized Solar Cells,” *Angew. Chemie Int. Ed.* **49**, 3653 (2010).

[25] S. N. Habisreutinger, T. Leijtens, G. E. Eperon, S. D. Stranks, R. J. Nicholas, and H. J. Snaith, “Carbon nanotube/polymer composites as a highly stable hole collection layer in perovskite solar cells,” *Nano Lett.* **14**, 5561 (2014).

[26] I. Jeon, T. Chiba, C. Delacou, Y. Guo, A. Kaskela, O. Reynaud, E. I. Kauppinen, S. Maruyama, and Y. Matsuo, “Single-Walled Carbon Nanotube Film as Electrode in Indium-Free Planar Heterojunction Perovskite Solar Cells: Investigation of Electron-Blocking Layers and Dopants,” *Nano Lett.* **15**, 6665 (2015).

[27] K. Cui, A. S. Anisimov, T. Chiba, S. Fujii, H. Kataura, A. G. Nasibulin, S. Chiashi, E. I. Kauppinen, and S. Maruyama, “Air-stable high-efficiency solar cells with dry-transferred single-walled carbon nanotube films,” *J. Mater. Chem. A* **2**, 11311 (2014).

[28] R. M. Jain, R. Howden, K. Tvrdy, S. Shimizu, A. J. Hilmer, T. P. McNicholas, K. K. Gleason, and M. S. Strano, “Polymer-Free Near-Infrared Photovoltaics with Single Chirality (6,5) Semiconducting Carbon Nanotube Active Layers,” *Adv. Mater.* **24**, 4436 (2012).

[29] T. Mueller, M. Kinoshita, M. Steiner, V. Perebeinos, A. A. Bol, D. B. Farmer, and P.

Avouris, "Efficient narrow-band light emission from a single carbon nanotube p–n diode," *Nat. Nanotechnol.* **5**, 27 (2010).

[30] X. Ma, N. F. Hartmann, J. K. S. Baldwin, S. K. Doorn, and H. Htoon, "Room-temperature single-photon generation from solitary dopants of carbon nanotubes," *Nat. Nanotechnol.* **10**, 671 (2015).

[31] A. Ishii, T. Uda, and Y. K. Kato, "Room-Temperature Single-Photon Emission from Micrometer-Long Air-Suspended Carbon Nanotubes," *Phys. Rev. Appl.* **8**, 54039 (2017).

[32] S. Tans, A. Verschueren, and C. Dekker, "Room-temperature transistor based on a single carbon nanotube," *Nature* **672**, 669 (1998).

[33] Q. Cao, H. Kim, N. Pimparkar, J. P. Kulkarni, C. Wang, M. Shim, K. Roy, M. A. Alam, and J. A. Rogers, "Medium-scale carbon nanotube thin-film integrated circuits on flexible plastic substrates," *Nature* **454**, 495 (2008).

[34] J. H. Koo, S. Jeong, H. J. Shim, D. Son, J. Kim, D. C. Kim, S. Choi, J.-I. Hong, and D.-H. Kim, "Wearable Electrocardiogram Monitor Using Carbon Nanotube Electronics and Color-Tunable Organic Light-Emitting Diodes," *ACS Nano* **11**, 10032 (2017).

[35] L. Jiao, B. Fan, X. Xian, Z. Wu, J. Zhang, and Z. Liu, "Creation of nanostructures with poly(methyl methacrylate)-mediated nanotransfer printing," *J. Am. Chem. Soc.* **130**, 12612 (2008).

[36] N. Patil, A. Lin, E. R. Myers, K. Ryu, A. Badmaev, C. Zhou, H.-S. P. Wong, and S. Mitra, "Wafer-scale growth and transfer of aligned single-walled carbon nanotubes," *IEEE Trans. Nanotechnol.* **8**, 498 (2009).

[37] G. J. Brady, K. R. Jinkins, and M. S. Arnold, "Channel length scaling behavior in transistors based on individual versus dense arrays of carbon nanotubes," *J. Appl. Phys.* **122**, 124506 (2017).

[38] C. Kocabas, S. J. Kang, T. Ozel, M. Shim, and J. A. Rogers, "Improved Synthesis of Aligned Arrays of Single-Walled Carbon Nanotubes and Their Implementation in Thin Film Type Transistors," *J. Phys. Chem. C* **111**, 17879 (2007).

[39] A. Vijayaraghavan, S. Blatt, D. Weissenberger, M. Oron-Carl, F. Hennrich, D. Gerthsen, H. Hahn, and R. Krupke, "Ultra-Large-Scale Directed Assembly of Single-Walled Carbon Nanotube Devices," *Nano Lett.* **7**, 1556 (2007).

[40] Q. Cao, S. Han, G. S. Tulevski, Y. Zhu, D. D. Lu, and W. Haensch, "Arrays of single-walled carbon nanotubes with full surface coverage for high-performance electronics," *Nat. Nanotechnol.* **8**, 180 (2013).

[41] M. S. Arnold, A. a Green, J. F. Hulvat, S. I. Stupp, and M. C. Hersam, "Sorting carbon nanotubes by electronic structure using density differentiation," *Nat. Nanotechnol.* **1**, 60 (2006).

[42] X. Tu, S. Manohar, A. Jagota, and M. Zheng, "DNA sequence motifs for structure-specific recognition and separation of carbon nanotubes," *Nature* **460**, 250 (2009).

[43] H. Wang, J. Mei, P. Liu, K. Schmidt, G. Jiménez-Osés, S. Osuna, L. Fang, C. J. Tassone, A. P. Zoombelt, A. N. Sokolov, K. N. Houk, M. F. Toney, and Z. Bao, "Scalable and selective dispersion of semiconducting arc-discharged carbon

nanotubes by dithiafulvalene/thiophene copolymers for thin film transistors," *ACS Nano* **7**, 2659 (2013).

[44] H. Liu, D. Nishide, T. Tanaka, and H. Kataura, "Large-scale single-chirality separation of single-wall carbon nanotubes by simple gel chromatography," *Nat. Commun.* **2**, 309 (2011).

[45] J. Payne, A. Lin, J. Zhang, H. Wong, and S. Mitra, "Digital VLSI logic technology using carbon nanotube FETs: Frequently asked questions," *Proc. 46th Annu. Des. Autom. Conf.*, 304 (2009).

[46] A. Javey, J. Guo, Q. Wang, M. Lundstrom, and H. Dai, "Ballistic carbon nanotube field-effect transistors," *Nature* **424**, 654 (2003).

[47] A. D. Franklin and Z. Chen, "Length scaling of carbon nanotube transistors," *Nat. Nanotechnol.* **5**, 858 (2010).

[48] Q. Cao, S.-J. Han, J. Tersoff, A. D. Franklin, Y. Zhu, Z. Zhang, G. S. Tulevski, J. Tang, and W. Haensch, "End-bonded contacts for carbon nanotube transistors with low, size-independent resistance," *Science* **350**, 68 (2015).

[49] J. Chen, C. Klinke, A. Afzali, and P. Avouris, "Self-aligned carbon nanotube transistors with charge transfer doping," *Appl. Phys. Lett.* **86**, 1 (2005).

[50] C. M. Aguirre, P. L. Levesque, M. Paillet, F. Lapointe, B. C. St-Antoine, P. Desjardins, and R. Martel, "The Role of the Oxygen/Water Redox Couple in Suppressing Electron Conduction in Field-Effect Transistors," *Adv. Mater.* **21**, 3087 (2009).

[51] L. Suriyasena Liyanage, X. Xu, G. Pitner, Z. Bao, and H.-S. P. Wong, "VLSI-Compatible Carbon Nanotube Doping Technique with Low Work-Function Metal Oxides," *Nano Lett.* **14**, 1884 (2014).

[52] Z. Zhang, X. Liang, S. Wang, K. Yao, Y. Hu, Y. Zhu, Q. Chen, W. Zhou, Y. Li, Y. Yao, J. Zhang, and L.-M. Peng, "Doping-free fabrication of carbon nanotube based ballistic CMOS devices and circuits," *Nano Lett.* **7**, 3603 (2007).

[53] N. Patil, Jie Deng, S. Mitra, and H.-S. P. Wong, "Circuit-Level Performance Benchmarking and Scalability Analysis of Carbon Nanotube Transistor Circuits," *IEEE Trans. Nanotechnol.* **8**, 37 (2009).

[54] A. D. Franklin, "Electronics: The road to carbon nanotube transistors," *Nature* **498**, 443 (2013).

[55] C. Kocabas, M. Shim, and J. A. Rogers, "Spatially Selective Guided Growth of High-Coverage Arrays and Random Networks of Single-Walled Carbon Nanotubes and Their Integration into Electronic Devices," *J. Am. Chem. Soc.* **128**, 4540 (2006).

[56] M. M. Shulaker, J. Van Rethy, T. F. Wu, L. Suriyasena Liyanage, H. Wei, Z. Li, E. Pop, G. Gielen, H.-S. P. Wong, and S. Mitra, "Carbon Nanotube Circuit Integration up to Sub-20 nm Channel Lengths," *ACS Nano* **8**, 3434 (2014).

[57] Y. Hu, L. Kang, Q. Zhao, H. Zhong, S. Zhang, L. Yang, Z. Wang, J. Lin, Q. Li, Z. Zhang, L.-M. Peng, Z. Liu, and J. Zhang, "Growth of high-density horizontally aligned SWNT arrays using Trojan catalysts," *Nat. Commun.* **6**, 6099 (2015).

[58] F. Yang, X. Wang, J. Si, X. Zhao, K. Qi, C. Jin, Z. Zhang, M. Li, D. Zhang, J. Yang,

Z. Zhang, Z. Xu, L.-M. Peng, X. Bai, and Y. Li, “Water-Assisted Preparation of High-Purity Semiconducting (14,4) Carbon Nanotubes,” *ACS Nano* **11**, 186 (2017).

[59] S. Zhang, L. Kang, X. Wang, L. Tong, L. Yang, Z. Wang, K. Qi, S. Deng, Q. Li, X. Bai, F. Ding, and J. Zhang, “Arrays of horizontal carbon nanotubes of controlled chirality grown using designed catalysts,” *Nature* **543**, 234 (2017).

[60] J. An, Z. Zhan, S. V. Hari Krishna, and L. Zheng, “Growth condition mediated catalyst effects on the density and length of horizontally aligned single-walled carbon nanotube arrays,” *Chem. Eng. J.* **237**, 16 (2014).

[61] T. Inoue, D. Hasegawa, S. Chiashi, and S. Maruyama, “Chirality analysis of horizontally aligned single-walled carbon nanotubes: decoupling populations and lengths,” *J. Mater. Chem. A* **3**, 15119 (2015).

[62] J. W. G. Wilder, L. C. Venema, A. G. Rinzler, R. E. Smalley, and C. Dekker, “Electronic structure of atomically resolved carbon nanotubes,” *Nature* **391**, 59 (1998).

[63] S. M. Bachilo, M. S. Strano, C. Kittrell, R. H. Hauge, R. E. Smalley, and R. B. Weisman, “Structure-assigned optical spectra of single-walled carbon nanotubes,” *Science* **298**, 2361 (2002).

[64] M. Y. Sfeir, F. Wang, L. Huang, C. C. Chuang, J. Hone, P. O’Brien S, T. F. Heinz, and L. E. Brus, “Probing electronic transitions in individual carbon nanotubes by Rayleigh scattering,” *Science* **306**, 1540 (2004).

[65] K. Liu, X. Hong, Q. Zhou, C. Jin, J. Li, W. Zhou, J. Liu, E. Wang, A. Zettl, and F. Wang, “High-throughput optical imaging and spectroscopy of individual carbon nanotubes in devices,” *Nat. Nanotechnol.* **8**, 917 (2013).

[66] S. Chiashi, K. Kono, D. Matsumoto, J. Shitaba, N. Homma, A. Beniya, T. Yamamoto, and Y. Homma, “Adsorption effects on radial breathing mode of single-walled carbon nanotubes,” *Phys. Rev. B* **91**, 155415 (2015).

[67] Y. Piao, J. R. Simpson, J. K. Streit, G. Ao, M. Zheng, J. A. Fagan, and A. R. Hight Walker, “Intensity Ratio of Resonant Raman Modes for (n,m) Enriched Semiconducting Carbon Nanotubes,” *ACS Nano* **10**, 5252 (2016).

[68] H. Telg, J. G. Duque, M. Staiger, X. Tu, F. Hennrich, M. M. Kappes, M. Zheng, J. Maultzsch, C. Thomsen, and S. K. Doorn, “Chiral index dependence of the G^+ and G^- Raman modes in semiconducting carbon nanotubes,” *ACS Nano* **6**, 904 (2012).

[69] F. Ding, A. R. Harutyunyan, and B. I. Yakobson, “Dislocation theory of chirality-controlled nanotube growth,” *Proc. Natl. Acad. Sci.* **106**, 2506 (2009).

[70] R. Rao, D. Liptak, T. Cherukuri, B. I. Yakobson, and B. Maruyama, “In situ evidence for chirality-dependent growth rates of individual carbon nanotubes,” *Nat. Mater.* **11**, 213 (2012).

[71] S. Hofmann, R. Sharma, C. Ducati, G. Du, C. Mattevi, C. Cepek, M. Cantoro, S. Pisana, A. Parvez, F. Cervantes-Sodi, A. C. Ferrari, R. Dunin-Borkowski, S. Lizzit, L. Petaccia, A. Goldoni, and J. Robertson, “In situ observations of catalyst dynamics during surface-bound carbon nanotube nucleation,” *Nano Lett.* **7**, 602 (2007).

[72] M.-F. C. Fiawoo, A.-M. Bonnot, H. Amara, C. Bichara, J. Thibault-Pénisson, and A. Loiseau, “Evidence of Correlation between Catalyst Particles and the Single-Wall

Carbon Nanotube Diameter: A First Step towards Chirality Control," *Phys. Rev. Lett.* **108**, 195503 (2012).

[73] L. Zhang, M. He, T. W. Hansen, J. Kling, H. Jiang, E. I. Kauppinen, A. Loiseau, and J. B. Wagner, "Growth Termination and Multiple Nucleation of Single-Wall Carbon Nanotubes Evidenced by in Situ Transmission Electron Microscopy," *ACS Nano* **11**, 4483 (2017).

[74] I. Wako, T. Chokan, D. Takagi, S. Chiashi, and Y. Homma, "Direct observation of single-walled carbon nanotube growth processes on SiO_2 substrate by in situ scanning electron microscopy," *Chem. Phys. Lett.* **449**, 309 (2007).

[75] L. Liu and S. Fan, "Isotope labeling of carbon nanotubes and formation of ^{12}C-^{13}C nanotube junctions," *J. Am. Chem. Soc.* **123**, 11502 (2001).

[76] H. Ago, N. Ishigami, N. Yoshihara, K. Imamoto, S. Akita, K. Ikeda, M. Tsuji, T. Ikuta, and K. Takahashi, "Visualization of Horizontally-Aligned Single-Walled Carbon Nanotube Growth with $^{13}C/^{12}C$ Isotopes," *J. Phys. Chem. C* **112**, 1735 (2008).

[77] X. Li, W. Cai, L. Colombo, and R. S. Ruoff, "Evolution of Graphene Growth on Ni and Cu by Carbon Isotope Labeling," *Nano Lett.* **9**, 4268 (2009).

[78] E. Whiteway, W. Yang, V. Yu, and M. Hilke, "Time evolution of the growth of single graphene crystals and high resolution isotope labeling," *Carbon* **111**, 173 (2017).

[79] L. Sun, L. Lin, J. Zhang, H. Wang, H. Peng, and Z. Liu, "Visualizing fast growth of large single-crystalline graphene by tunable isotopic carbon source," *Nano Res.* **10**, 355 (2017).

[80] L. Ding, D. Yuan, and J. Liu, "Growth of High-Density Parallel Arrays of Long Single-Walled Carbon Nanotubes on Quartz Substrates," *J. Am. Chem. Soc.* **130**, 5428 (2008).

[81] R. Zhang, Y. Zhang, Q. Zhang, H. Xie, W. Qian, and F. Wei, "Growth of Half-Meter Long Carbon Nanotubes Based on Schulz–Flory Distribution," *ACS Nano* **7**, 6156 (2013).

[82] E. Einarsson, Y. Murakami, M. Kadowaki, and S. Maruyama, "Growth dynamics of vertically aligned single-walled carbon nanotubes from in situ measurements," *Carbon* **46**, 923 (2008).

[83] D. N. Futaba, K. Hata, T. Yamada, K. Mizuno, M. Yumura, and S. Iijima, "Kinetics of Water-Assisted Single-Walled Carbon Nanotube Synthesis Revealed by a Time-Evolution Analysis," *Phys. Rev. Lett.* **95**, 56104 (2005).

[84] M. Lin, J. P. Ying Tan, C. Boothroyd, K. P. Loh, E. S. Tok, and Y.-L. Foo, "Direct Observation of Single-Walled Carbon Nanotube Growth at the Atomistic Scale," *Nano Lett.* **6**, 449 (2006).

[85] B. Liu, J. Liu, X. Tu, J. Zhang, M. Zheng, and C. Zhou, "Chirality-Dependent Vapor-Phase Epitaxial Growth and Termination of Single-Wall Carbon Nanotubes," *Nano Lett.* **13**, 4416 (2013).

[86] K. Hasegawa and S. Noda, "Millimeter-tall single-walled carbon nanotubes rapidly grown with and without water," *ACS Nano* **5**, 975 (2011).

[87] M. Picher, E. Anglaret, R. Arenal, and V. Jourdain, "Self-Deactivation of Single-Walled Carbon Nanotube Growth Studied by in Situ Raman Measurements," *Nano Lett.* **9**, 542 (2009).

[88] M. Stadermann, S. P. Sherlock, J. In, F. Fornasiero, H. G. Park, A. B. Artyukhin, Y. Wang, J. J. De Yoreo, C. P. Grigoropoulos, O. Bakajin, A. A. Chernov, and A. Noy, "Mechanism and Kinetics of Growth Termination in Controlled Chemical Vapor Deposition Growth of Multiwall Carbon Nanotube Arrays," *Nano Lett.* **9**, 738 (2009).

[89] M. He, Y. Magnin, H. Amara, H. Jiang, H. Cui, F. Fossard, A. Castan, E. Kauppinen, A. Loiseau, and C. Bichara, "Linking growth mode to lengths of single-walled carbon nanotubes," *Carbon* **113**, 231 (2017).

[90] G. Eres, C. M. Rouleau, M. Yoon, A. A. Puretzky, J. J. Jackson, and D. B. Geohegan, "Model for Self-Assembly of Carbon Nanotubes from Acetylene Based on Real-Time Studies of Vertically Aligned Growth Kinetics," *J. Phys. Chem. C* **113**, 15484 (2009).

[91] A. Li-Pook-Than, J. Lefebvre, and P. Finnie, "Phases of Carbon Nanotube Growth and Population Evolution from in Situ Raman Spectroscopy during Chemical Vapor Deposition," *J. Phys. Chem. C* **114**, 11018 (2010).

[92] Q. Yuan, Z. Xu, B. I. Yakobson, and F. Ding, "Efficient Defect Healing in Catalytic Carbon Nanotube Growth," *Phys. Rev. Lett.* **108**, 245505 (2012).

[93] B. Chandra, J. Bhattacharjee, M. Purewal, Y. Son, Y. Wu, M. Huang, H. Yan, T. F. Heinz, P. Kim, J. B. Neaton, and J. Hone, "Molecular-Scale Quantum Dots from Carbon Nanotube Heterojunctions," *Nano Lett.* **9**, 1544 (2009).

[94] D. Y. Joh, L. H. Herman, S.-Y. Ju, J. Kinder, M. A. Segal, J. N. Johnson, G. K. L. Chan, and J. Park, "On-Chip Rayleigh Imaging and Spectroscopy of Carbon Nanotubes," *Nano Lett.* **11**, 1 (2011).

[95] L. Kang, S. Zhang, Q. Li, and J. Zhang, "Growth of Horizontal Semiconducting SWNT Arrays with Density Higher than 100 tubes/µm using Ethanol/Methane Chemical Vapor Deposition," *J. Am. Chem. Soc.* **138**, 6727 (2016).

[96] M. Picher, E. Anglaret, and V. Jourdain, "High temperature activation and deactivation of single-walled carbon nanotube growth investigated by in situ Raman measurements," *Diam. Relat. Mater.* **19**, 581 (2010).

[97] T. Inoue, D. Hasegawa, S. Badar, S. Aikawa, S. Chiashi, and S. Maruyama, "Effect of Gas Pressure on the Density of Horizontally Aligned Single-Walled Carbon Nanotubes Grown on Quartz Substrates," *J. Phys. Chem. C* **117**, 11804 (2013).

[98] Y. Yao, Q. Li, J. Zhang, R. Liu, L. Jiao, Y. T. Zhu, and Z. Liu, "Temperature-mediated growth of single-walled carbon-nanotube intramolecular junctions," *Nat. Mater.* **6**, 293 (2007).

[99] C. T. Wirth, C. Zhang, G. Zhong, S. Hofmann, and J. Robertson, "Diffusion- and Reaction-Limited Growth of Carbon Nanotube Forests," *ACS Nano* **3**, 3560 (2009).

[100] F. Rao, Y. Zhou, T. Li, and Y. Wang, "Synthesis of radially aligned single-walled carbon nanotubes on a SiO_2/Si substrate by introducing sodium chloride," *Carbon* **47**, 2548 (2009).

[101] R. Krupke, F. Hennrich, H. v. Löhneysen, and M. M. Kappes, "Separation of Metallic from Semiconducting Single-Walled Carbon Nanotubes," *Science* **301**, 344 (2003).

[102] C. Y. Khripin, J. A. Fagan, and M. Zheng, “Spontaneous Partition of Carbon Nanotubes in Polymer-Modified Aqueous Phases,” *J. Am. Chem. Soc.* **135**, 6822 (2013).

[103] G. J. Brady, A. J. Way, N. S. Safron, H. T. Evensen, P. Gopalan, and M. S. Arnold, “Quasi-ballistic carbon nanotube array transistors with current density exceeding Si and GaAs,” *Sci. Adv.* **2**, e1601240 (2016).

[104] Y. Joo, G. J. Brady, M. S. Arnold, and P. Gopalan, “Dose-Controlled, Floating Evaporative Self-assembly and Alignment of Semiconducting Carbon Nanotubes from Organic Solvents,” *Langmuir* **30**, 3460 (2014).

[105] Q. Cao, S.-J. Han, and G. S. Tulevski, “Fringing-field dielectrophoretic assembly of ultrahigh-density semiconducting nanotube arrays with a self-limited pitch,” *Nat. Commun.* **5**, 5071 (2014).

[106] X. He, W. Gao, L. Xie, B. Li, Q. Zhang, S. Lei, J. M. Robinson, E. H. Hároz, S. K. Doorn, W. Wang, R. Vajtai, P. M. Ajayan, W. W. Adams, R. H. Hauge, and J. Kono, “Wafer-scale monodomain films of spontaneously aligned single-walled carbon nanotubes,” *Nat. Nanotechnol.* **11**, 633 (2016).

[107] W. Zhou, S. Zhan, L. Ding, and J. Liu, “General Rules for Selective Growth of Enriched Semiconducting Single Walled Carbon Nanotubes with Water Vapor as in Situ Etchant,” *J. Am. Chem. Soc.* **134**, 14019 (2012).

[108] F. Yang, X. Wang, D. Zhang, J. Yang, D. Luo, Z. Xu, J. Wei, J.-Q. Wang, Z. Xu, F. Peng, X. Li, R. Li, Y. Li, M. Li, X. Bai, F. Ding, and Y. Li, “Chirality-specific growth of single-walled carbon nanotubes on solid alloy catalysts,” *Nature* **510**, 522 (2014).

[109] G. Zhang, P. Qi, X. Wang, Y. Lu, X. Li, R. Tu, S. Bangsaruntip, D. Mann, L. Zhang, and H. Dai, “Selective Etching of Metallic Carbon Nanotubes by Gas-Phase Reaction,” *Science* **314**, 974 (2006).

[110] P. Li and J. Zhang, “Sorting out semiconducting single-walled carbon nanotube arrays by preferential destruction of metallic tubes using water,” *J. Mater. Chem.* **21**, 11815 (2011).

[111] J. Yang, Y. Liu, D. Zhang, X. Wang, R. Li, and Y. Li, “Radial deformation of single-walled carbon nanotubes on quartz substrates and the resultant anomalous diameter-dependent reaction selectivity,” *Nano Res.* **8**, 3054 (2015).

[112] M. Yudasaka, M. Zhang, and S. Iijima, “Diameter-selective removal of single-wall carbon nanotubes through light-assisted oxidation,” *Chem. Phys. Lett.* **374**, 132 (2003).

[113] H. C. Shim, J.-W. Song, Y. K. Kwak, S. Kim, and C.-S. Han, “Preferential elimination of metallic single-walled carbon nanotubes using microwave irradiation,” *Nanotechnology* **20**, 65707 (2009).

[114] G. Hong, M. Zhou, R. Zhang, S. Hou, W. Choi, Y. S. Woo, J.-Y. Choi, Z. Liu, and J. Zhang, “Separation of Metallic and Semiconducting Single-Walled Carbon Nanotube Arrays by ‘Scotch Tape,’” *Angew. Chemie Int. Ed.* **50**, 6819 (2011).

[115] Y. Hu, Y. Chen, P. Li, and J. Zhang, “Sorting out Semiconducting Single-Walled Carbon Nanotube Arrays by Washing off Metallic Tubes Using SDS Aqueous

Solution," *Small* **9**, 1306 (2013).

[116] P. G. Collins, M. S. Arnold, and P. Avouris, "Engineering Carbon Nanotubes and Nanotube Circuits Using Electrical Breakdown," *Science* **292**, 706 (2001).

[117] M. M. Shulaker, G. Pitner, G. Hills, M. Giachino, H.-S. P. Wong, and S. Mitra, "High-performance carbon nanotube field-effect transistors," in *2014 IEEE Int. Electron Devices Meet.* **4**, 33.6.1 (2014).

[118] M. M. Shulaker, J. Van Rethy, G. Hills, H. Wei, H.-Y. Chen, G. Gielen, H.-S. P. Wong, and S. Mitra, "Sensor-to-Digital Interface Built Entirely With Carbon Nanotube FETs," *IEEE J. Solid-State Circuits* **49**, 190 (2014).

[119] M. M. Shulaker, G. Hills, N. Patil, H. Wei, H.-Y. Chen, H.-S. P. Wong, and S. Mitra, "Carbon nanotube computer," *Nature* **501**, 526 (2013).

[120] N. Patil, A. Lin, J. Zhang, H. Wei, K. Anderson, H.-S. Philip Wong, and S. Mitra, "Scalable Carbon Nanotube Computational and Storage Circuits Immune to Metallic and Mispositioned Carbon Nanotubes," *IEEE Trans. Nanotechnol.* **10**, 744 (2011).

[121] M. M. Shulaker, J. Van Rethy, T. F. Wu, L. Suriyasena Liyanage, H. Wei, Z. Li, E. Pop, G. Gielen, H.-S. P. Wong, and S. Mitra, "Carbon Nanotube Circuit Integration up to Sub-20 nm Channel Lengths," *ACS Nano* **8**, 3434 (2014).

[122] E. Pop, "The role of electrical and thermal contact resistance for Joule breakdown of single-wall carbon nanotubes," *Nanotechnology* **19**, 295202 (2008).

[123] S. H. Jin, S. N. Dunham, J. Song, X. Xie, J. Kim, C. Lu, A. Islam, F. Du, J. Kim, et al., "Using nanoscale thermocapillary flows to create arrays of purely semiconducting single-walled carbon nanotubes," *Nat. Nanotechnol.* **8**, 347 (2013).

[124] M. M. Shulaker, G. Hills, T. F. Wu, Z. Bao, H.-S. P. Wong, and S. Mitra, "Efficient metallic carbon nanotube removal for highly-scaled technologies," in *2015 IEEE Int. Electron Devices Meet.*, 32.4.1, IEEE (2015).

[125] X. Xie, S. H. Jin, M. a Wahab, A. E. Islam, C. Zhang, F. Du, E. Seabron, T. Lu, S. N. Dunham, et al., "Microwave purification of large-area horizontally aligned arrays of single-walled carbon nanotubes," *Nat. Commun.* **5**, 5332 (2014).

[126] F. Du, J. R. Felts, X. Xie, J. Song, Y. Li, M. R. Rosenberger, A. E. Islam, S. H. Jin, S. N. Dunham, C. Zhang, W. L. Wilson, Y. Huang, W. P. King, and J. A. Rogers, "Laser-Induced Nanoscale Thermocapillary Flow for Purification of Aligned Arrays of Single-Walled Carbon Nanotubes," *ACS Nano* **8**, 12641 (2014).

[127] K. Otsuka, T. Inoue, Y. Shimomura, S. Chiashi, and S. Maruyama, "Water-assisted self-sustained burning of metallic single-walled carbon nanotubes for scalable transistor fabrication," *Nano Res.* **10**, 3248 (2017).

[128] K. Otsuka, T. Inoue, S. Chiashi, and S. Maruyama, "Selective removal of metallic single-walled carbon nanotubes in full length by organic film-assisted electrical breakdown," *Nanoscale* **6**, 8831 (2014).

[129] A. D. Liao, R. Alizadegan, Z.-Y. Ong, S. Dutta, F. Xiong, K. J. Hsia, and E. Pop, "Thermal dissipation and variability in electrical breakdown of carbon nanotube devices," *Phys. Rev. B* **82**, 205406 (2010).

[130] X. Xie, K. L. Grosse, J. Song, C. Lu, S. Dunham, F. Du, A. E. Islam, Y. Li, Y.

Zhang, E. Pop, Y. Huang, W. P. King, and J. A. Rogers, “Quantitative Thermal Imaging of Single-Walled Carbon Nanotube Devices by Scanning Joule Expansion Microscopy,” *ACS Nano* **6**, 10267 (2012).

[131] K. Otsuka, T. Inoue, Y. Shimomura, S. Chiashi, and S. Maruyama, “Field emission and anode etching during formation of length-controlled nanogaps in electrical breakdown of horizontally aligned single-walled carbon nanotubes,” *Nanoscale* **8**, 16363 (2016).

[132] Y. Homma, S. Chiashi, T. Yamamoto, K. Kono, D. Matsumoto, J. Shitaba, and S. Sato, “Photoluminescence Measurements and Molecular Dynamics Simulations of Water Adsorption on the Hydrophobic Surface of a Carbon Nanotube in Water Vapor,” *Phys. Rev. Lett.* **110**, 157402 (2013).

[133] Q. Cao, M. Xia, C. Kocabas, M. Shim, J. A. Rogers, and S. V. Rotkin, “Gate capacitance coupling of singled-walled carbon nanotube thin-film transistors,” *Appl. Phys. Lett.* **90**, 23516 (2007).

[134] M. A. Wahab and M. A. Alam, “Implications of Electrical Crosstalk for High Density Aligned Array of Single-Wall Carbon Nanotubes,” *IEEE Trans. Electron Devices* **61**, 4273 (2014).

[135] S. Deng, J. Tang, L. Kang, Y. Hu, F. Yao, Q. Zhao, S. Zhang, K. Liu, and J. Zhang, “High-Throughput Determination of Statistical Structure Information for Horizontal Carbon Nanotube Arrays by Optical Imaging,” *Adv. Mater.* **28**, 2018 (2016).

[136] K. Matsui, H. Tsuji, and A. Makino, “A further study of the effects of water vapor concentration on the rate of combustion of an artificial graphite in humid air flow,” *Combust. Flame* **63**, 415 (1986).

[137] G. A. Jensen, “The Kinetics of Gasification of Carbon Contained in Coal Minerals at Atmospheric Pressure,” *Ind. Eng. Chem. Process Des. Dev.* **14**, 308 (1975).

[138] Z.-Y. Ong and E. Pop, “Molecular dynamics simulation of thermal boundary conductance between carbon nanotubes and SiO_2,” *Phys. Rev. B* **81**, 155408 (2010).

[139] S. Chiashi, T. Hanashima, R. Mitobe, K. Nagatsu, T. Yamamoto, and Y. Homma, “Water Encapsulation Control in Individual Single-Walled Carbon Nanotubes by Laser Irradiation,” *J. Phys. Chem. Lett.* **5**, 408 (2014).

[140] W. Kim, A. Javey, O. Vermesh, Q. Wang, Y. Li, and H. Dai, “Hysteresis Caused by Water Molecules in Carbon Nanotube Field-Effect Transistors,” *Nano Lett.* **3**, 193 (2003).

[141] W. Choi, S. Hong, J. T. Abrahamson, J.-H. Han, C. Song, N. Nair, S. Baik, and M. S. Strano, “Chemically driven carbon-nanotube-guided thermopower waves,” *Nat. Mater.* **9**, 423 (2010).

[142] E. Pop, D. Mann, Q. Wang, K. Goodson, and H. Dai, “Thermal Conductance of an Individual Single-Wall Carbon Nanotube above Room Temperature,” *Nano Lett.* **6**, 96 (2006).

[143] S. Hida, T. Hori, T. Shiga, J. Elliott, and J. Shiomi, “Thermal resistance and phonon scattering at the interface between carbon nanotube and amorphous polyethylene,” *Int. J. Heat Mass Transf.* **67**, 1024 (2013).

[144] T. Hirata, T. Kashiwagi, and J. E. Brown, “Thermal and oxidative degradation of

poly(methyl methacrylate): weight loss," *Macromolecules* **18**, 1410 (1985).

[145] S. Maruyama, "A molecular dynamics simulation of heat conduction in finite length SWNTs," *Phys. B Condens. Matter* **323**, 193 (2002).

[146] P. Qi, A. Javey, M. Rolandi, Q. Wang, E. Yenilmez, and H. Dai, "Miniature organic transistors with carbon nanotubes as quasi-one-dimensional electrodes," *J. Am. Chem. Soc.* **126**, 11774 (2004).

[147] F. Xiong, A. D. Liao, D. Estrada, and E. Pop, "Low-Power Switching of Phase-Change Materials with Carbon Nanotube Electrodes," *Science* **332**, 568 (2011).

[148] E. Pop, D. A. Mann, K. E. Goodson, and H. Dai, "Electrical and thermal transport in metallic single-wall carbon nanotubes on insulating substrates," *J. Appl. Phys.* **101**, 93710 (2007).

[149] K. A. S. Araujo, A. P. M. Barboza, T. F. D. Fernandes, N. Shadmi, E. Joselevich, M. S. C. Mazzoni, and B. R. A. Neves, "Charge transfer between carbon nanotubes on surfaces," *Nanoscale* **7**, 16175 (2015).

[150] A. Javey, J. Guo, M. Paulsson, Q. Wang, D. Mann, M. Lundstrom, and H. Dai, "High-Field Quasiballistic Transport in Short Carbon Nanotubes," *Phys. Rev. Lett.* **92**, 106804 (2004).

[151] S. Suzuki, C. Bower, Y. Watanabe, and O. Zhou, "Work functions and valence band states of pristine and Cs-intercalated single-walled carbon nanotube bundles," *Appl. Phys. Lett.* **76**, 4007 (2000).

[152] J.-M. Bonard, K. Dean, B. Coll, and C. Klinke, "Field Emission of Individual Carbon Nanotubes in the Scanning Electron Microscope," *Phys. Rev. Lett.* **89**, 197602 (2002).

[153] A. Wadhawan, R. E. Stallcup, K. F. Stephens, J. M. Perez, and I. A. Akwani, "Effects of O2, Ar, and H2 gases on the field-emission properties of single-walled and multiwalled carbon nanotubes," *Appl. Phys. Lett.* **79**, 1867 (2001).

[154] K. A. Dean, P. von Allmen, and B. R. Chalamala, "Three behavioral states observed in field emission from single-walled carbon nanotubes," *J. Vac. Sci. Technol. B Microelectron. Nanom. Struct.* **17**, 1959 (1999).

[155] I. Brodie and C. A. Spindt, "Vacuum Microelectronics," in *Adv. Electron. Electron Phys.* **7**, 1 (1992).

[156] C. J. Edgcombe and U. Valdrè, "Microscopy and computational modelling to elucidate the enhancement factor for field electron emitters," *J. Microsc.* **203**, 188 (2001).

[157] R. C. Smith, D. C. Cox, and S. R. P. Silva, "Electron field emission from a single carbon nanotube: Effects of anode location," *Appl. Phys. Lett.* **87**, 103112 (2005).

[158] A. Maiti, J. Andzelm, N. Tanpipat, and P. von Allmen, "Effect of Adsorbates on Field Emission from Carbon Nanotubes," *Phys. Rev. Lett.* **87**, 155502 (2001).

[159] D. Wei, Y. Liu, L. Cao, H. Zhang, L. Huang, G. Yu, H. Kajiura, and Y. Li, "Selective Electrochemical Etching of Single-Walled Carbon Nanotubes," *Adv. Funct. Mater.* **19**, 3618 (2009).

[160] T. D. Yuzvinsky, A. M. Fennimore, W. Mickelson, C. Esquivias, and A. Zettl, "Precision cutting of nanotubes with a low-energy electron beam," *Appl. Phys. Lett.* **86**, 53109 (2005).

[161] B. Rajabifar, S. Kim, K. Slinker, G. J. Ehlert, A. J. Hart, and M. R. Maschmann, "Three-dimensional machining of carbon nanotube forests using water-assisted scanning electron microscope processing," *Appl. Phys. Lett.* **107**, 143102 (2015).

[162] Y. Shiratori, K. Furuichi, S. Noda, H. Sugime, Y. Tsuji, Z. Zhang, S. Maruyama, and Y. Yamaguchi, "Field Emission Properties of Single-Walled Carbon Nanotubes with a Variety of Emitter Morphologies," *Jpn. J. Appl. Phys.* **47**, 4780 (2008).

[163] R. Y. Zhang, Y. Wei, L. A. Nagahara, I. Amlani, and R. K. Tsui, "The contrast mechanism in low voltage scanning electron microscopy of single-walled carbon nanotubes," *Nanotechnology* **17**, 272 (2006).

[164] S. Shekhar, M. Erementchouk, M. N. Leuenberger, and S. I. Khondaker, "Correlated electrical breakdown in arrays of high density aligned carbon nanotubes," *Appl. Phys. Lett.* **98**, 243121 (2011).

[165] M. Ieong, B. Doris, J. Kedzierski, K. Rim, and M. Yang, "Silicon Device Scaling to the Sub-10-nm Regime," *Science* **306**, 2057 (2004).

[166] A. Javey, H. Kim, M. Brink, Q. Wang, A. Ural, J. Guo, P. McIntyre, P. McEuen, M. Lundstrom, and H. Dai, "High-κ dielectrics for advanced carbon-nanotube transistors and logic gates," *Nat. Mater.* **1**, 241 (2002).

[167] E. S. Snow, J. P. Novak, P. M. Campbell, and D. Park, "Random networks of carbon nanotubes as an electronic material," *Appl. Phys. Lett.* **82**, 2145 (2003).

[168] S. J. Kang, C. Kocabas, T. Ozel, M. Shim, N. Pimparkar, M. A. Alam, S. V. Rotkin, and J. A. Rogers, "High-performance electronics using dense, perfectly aligned arrays of single-walled carbon nanotubes," *Nat. Nanotechnol.* **2**, 230 (2007).

[169] S. W. Hong, T. Banks, and J. A. Rogers, "Improved Density in Aligned Arrays of Single-Walled Carbon Nanotubes by Sequential Chemical Vapor Deposition on Quartz," *Adv. Mater.* **22**, 1826 (2010).

[170] W. Zhou, L. Ding, S. Yang, and J. Liu, "Synthesis of High-Density, Large-Diameter, and Aligned Single-Walled Carbon Nanotubes by Multiple-Cycle Growth Methods," *ACS Nano* **5**, 3849 (2011).

[171] M. M. Shulaker, H. Wei, N. Patil, J. Provine, H. Chen, H.-S. P. Wong, and S. Mitra, "Linear Increases in Carbon Nanotube Density Through Multiple Transfer Technique," *Nano Lett.* **11**, 1881 (2011).

[172] W. J. Yu, S. H. Chae, Q. A. Vu, and Y. H. Lee, "Sorting centimetre-long single-walled carbon nanotubes," *Sci. Rep.* **6**, 30836 (2016).

[173] J. Si, D. Zhong, H. Xu, M. Xiao, C. Yu, Z. Zhang, and L. Peng, "Scalable Preparation of High-Density Semiconducting Carbon Nanotube Arrays for High-Performance Field-Effect Transistors," *ACS Nano* **12**, 627 (2018).

[174] G. Yu, A. Cao, and C. M. Lieber, "Large-area blown bubble films of aligned nanowires and carbon nanotubes," *Nat. Nanotechnol.* **2**, 372 (2007).

[175] D. Sun, M. Y. Timmermans, Y. Tian, A. G. Nasibulin, E. I. Kauppinen, S.

Kishimoto, T. Mizutani, and Y. Ohno, “Flexible high-performance carbon nanotube integrated circuits,” *Nat. Nanotechnol.* **6**, 156 (2011).

[176] M. Ha, Y. Xia, A. A. Green, W. Zhang, M. J. Renn, C. H. Kim, M. C. Hersam, and C. D. Frisbie, “Printed, Sub-3V Digital Circuits on Plastic from Aqueous Carbon Nanotube Inks,” *ACS Nano* **4**, 4388 (2010).

[177] Y. Yang, L. Ding, J. Han, Z. Zhang, and L.-M. Peng, “High-Performance Complementary Transistors and Medium-Scale Integrated Circuits Based on Carbon Nanotube Thin Films,” *ACS Nano* **11**, 4124 (2017).

[178] S. Maruyama, R. Kojima, Y. Miyauchi, S. Chiashi, and M. Kohno, “Low-temperature synthesis of high-purity single-walled carbon nanotubes from alcohol,” *Chem. Phys. Lett.* **360**, 229 (2002).

[179] K. Otsuka, T. Inoue, E. Maeda, R. Kometani, S. Chiashi, and S. Maruyama, “On-Chip Sorting of Long Semiconducting Carbon Nanotubes for Multiple Transistors along an Identical Array,” *ACS Nano* **11**, 11497 (2017).

[180] A. D. Franklin, M. Luisier, S.-J. Han, G. Tulevski, C. M. Breslin, L. Gignac, M. S. Lundstrom, and W. Haensch, “Sub-10 nm Carbon Nanotube Transistor,” *Nano Lett.* **12**, 758 (2012).

[181] A. E. Islam, F. Du, X. Ho, S. Hun Jin, S. N. Dunham, and J. A. Rogers, “Effect of variations in diameter and density on the statistics of aligned array carbon-nanotube field effect transistors,” *J. Appl. Phys.* **111**, 54511 (2012).

[182] J. Li, K. Liu, S. Liang, W. Zhou, M. Pierce, F. Wang, L.-M. Peng, and J. Liu, “Growth of High-Density-Aligned and Semiconducting-Enriched Single-Walled Carbon Nanotubes: Decoupling the Conflict between Density and Selectivity,” *ACS Nano* **8**, 554 (2014).

[183] L. Ding, W. Zhou, T. P. McNicholas, J. Wang, H. Chu, Y. Li, and J. Liu, “Direct observation of the strong interaction between carbon nanotubes and quartz substrate,” *Nano Res.* **2**, 903 (2009).

[184] P. Araujo, S. Doorn, S. Kilina, S. Tretiak, E. Einarsson, S. Maruyama, H. Chacham, M. Pimenta, and A. Jorio, “Third and Fourth Optical Transitions in Semiconducting Carbon Nanotubes,” *Phys. Rev. Lett.* **98**, 67401 (2007).

Appendix

A1 (*n*,*m*) assignment for isotope labeled SWNTs

For the SWNTs grown from ^{12}C ethanol, relationship between diameter d_t and RBM frequency ω_{RBM} was roughly given by $\omega_{RBM} = 217.8/d_t + 21.7$. On the other hand for the SWNTs synthesized from ^{12}C and ^{13}C ethanol (in Chapter 2), the relationship $\omega_{RBM} = 217.8/d_t + 20.2$ gives better assignment for pure ^{12}C nanotube parts, though the substrates and the transfer process of SWNTs were the same for both SWNT samples. Another difference is that the SWNTs with ^{13}C labels has less near-zigzag SWNTs. Growth condition was same except for ^{13}C ethanol introduction, but subtle difference of sample preparation and growth condition could affect the chiral-angle selectivity and even the relationship between RBM frequency and tube diameter. Since the SWNTs belong to different families and therefore had different level of resonance with incident laser, intensity of G-band and RBM was much different, making the assignment of (*n*,*m*) possible for similar RBM frequency. In Figure A.1(a), red lines show the chirality assignment used in Figure 2.9 and 2.12. For the SWNTs whose chiralities have other candidates, measured data (open circles) are connected to the other (*n*,*m*) with black dashed lines. Filled circles in gray represent the resonance of the same SWNTs with other wavelengths (only G-band), though not all SWNTs were

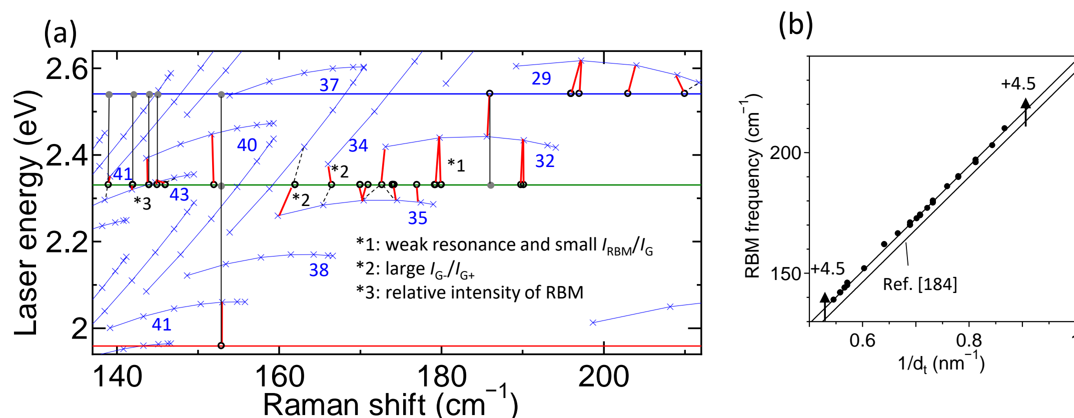

Figure A.1 (a) (*n*,*m*) assignment for the SWNTs shown in Chapter 2. (b) RBM frequency ω_{RBM} *versus* the inverse of diameter $1/d_t$. The relation $\omega_{RBM} = 217.8/d_t + 20.2$ (shifted by +4.5 cm^{-1} from the literature[184]) gives better assignment this sample. Only the spectra whose G-peak appears at >1588 cm^{-1} are plotted (*i.e.* not including ^{13}C-mixed parts). Redness of the plots represents the G-band intensity.

measured with multiple excitation wavelengths. Relationship between the (inverse of) diameter and RBM frequency for the present samples is shown in Figure A.1(b).

A2 Influence of ^{13}C ethanol on growth behavior

Since ^{13}C-enriched ethanol (Cambridge Isotope Laboratories, Inc., ethanol (1,2-$^{13}C_2$, 99%) (<6% H_2O) may contain more impurities (such as isopropanol and water) than normal ethanol, introduction of ^{13}C ethanol could affect the growth by inducing nucleation or termination, and by changing the growth rate. Figures A.2(a) and (b) compare the introduction of ^{13}C ethanol and the timing for nucleation (bottom) and termination (middle) of the SWNT growth for 12 min CVD and 24 min CVD,

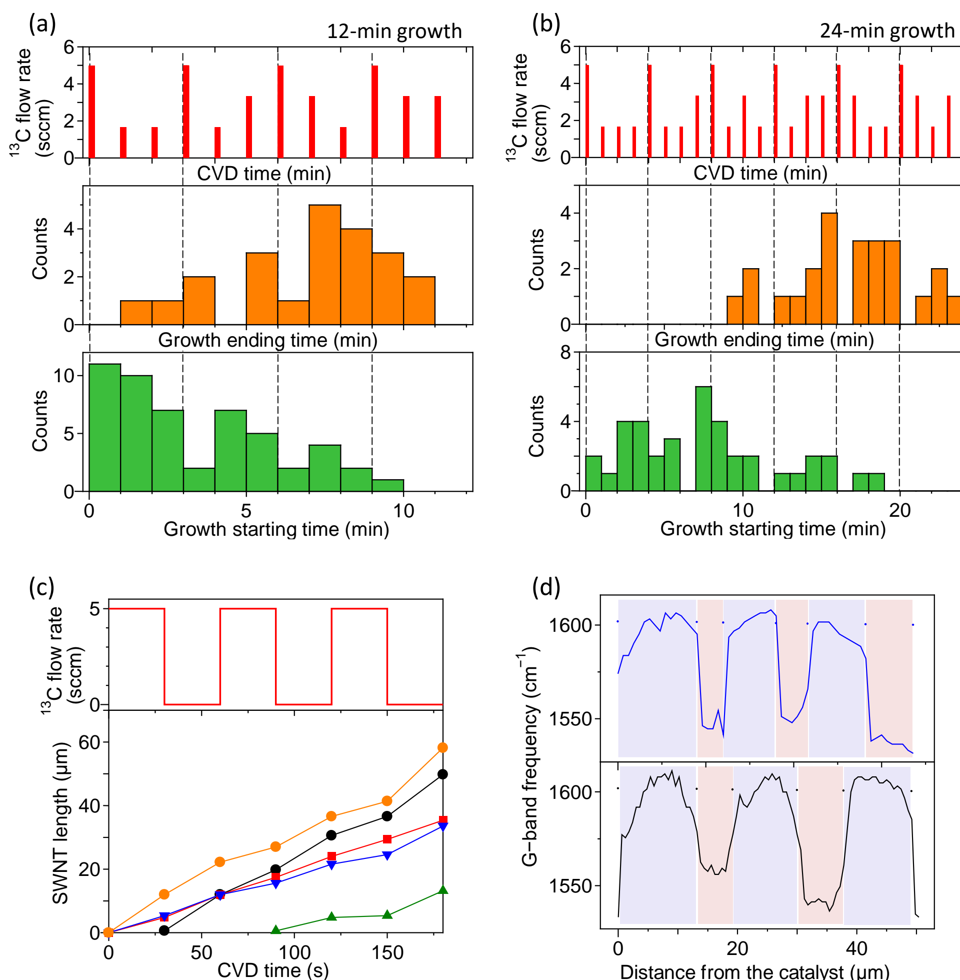

Figure A.2 (a,b) Introduction of ^{13}C ethanol (top panel) and distribution of incubation time (bottom panel) for the 12 min CVD growth (a) and 24 min CVD growth (b). (c) Time evolution of flow rate of ^{13}C ethanol (top) and the SWNTs lengths (bottom). Growth time was 3 min. (d) G-band peak position along the axis of two SWNTs (blue and black plots in (c)).

respectively. Judging from two sets of data, introduction of ^{13}C was unlikely to influence the nucleation and termination of the SWNT growth.

However, when the ^{12}C and ^{13}C ethanol was introduced in order as shown in the top panel of Figure A.2(a), the growth rate was faster with ^{12}C ethanol supply than that with ^{13}C ethanol. The difference is probability caused by impurities in ^{13}C ethanol, though the detailed information is missing. Digital isotope coding reduced the cost and such a negative effect arising from the isotope ethanol. It should be stressed that the Raman spectra in Figure A.2(d) were obtained from SWNTs on quartz substrates and therefore upshifted.[183] Digital coding of isotope labels is tolerant to such shifts of spectra and also cover long-time CVD by increasing digit number (*e.g.* 2-bit and 3-bit for Figure A.2(a) and (b), respectively), compared to analog isotope labeling in which the fraction of ^{13}C was gradually changed with time.[78]

A3 Ununiformity of RBM peaks along the tube

Raman spectrum is sensitive to the environment, and RBM frequency changes depending on physical adsorbates (other SWNTs, water, substrates, and etc.).[66] Even under the seemingly same environment (on thermal oxide of Si), RBM spectra can be upshifted and broadened, while G-band was relatively uniform along the axis of tube A1, as shown in Figure A.3(a). RBM spectrum even disappeared, though it was usually accompanied by a weak G-band signal. Since RBM frequencies of overall parts are the same, the chirality is very likely to be identical.

Some SWNTs had much more fluctuated RBM as shown in Figure A.3(b). Unlike the SWNTs shown in Figure 2.13, shifts of RBM frequency and change in growth rate (fast on tip side and slow on root side) is not linked. RBM spectra of pure ^{12}C SWNT parts with various RBM frequencies are shown in Figure A.3(c). In addition, full width at half maximum (FWHM) and intensity of RBM is plotted against the frequency. This clearly shows that higher frequency RBM has broader and weaker peaks. Since RBM with lowest frequency and sharpest is considered to be less affected by environments and has small variation, the lowest frequency was used for (n,m) assignment and estimation of the diameter.

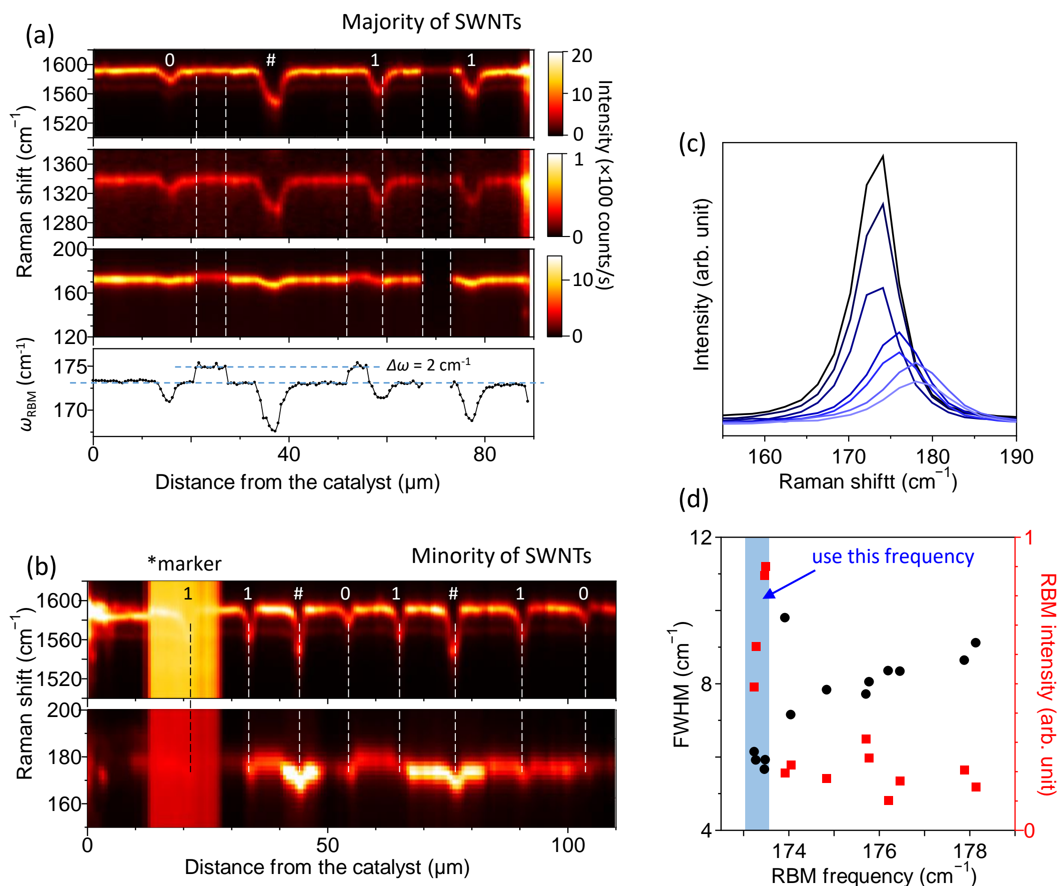

Figure A.3 (a) Typical Raman spectra (G, D and RBM) and RBM frequency along an isotope-labeled SWNT (tube A1). RBM signals were locally weakened and upshifted. (b) Unusual Raman spectra, in which RBM frequency and intensity fluctuated several times along the axis. (c) RBM spectra obtained from the same SWNT in (b). (d) Full width at half maximum (FWHM) and peak intensity of RBM plotted against RBM frequency.

List of publications

First Author Publications

1. **K. Otsuka**, T. Inoue, S. Chiashi, S. Maruyama, "Selective removal of metallic single-walled carbon nanotube in full length by organic film-assisted electrical breakdown", *Nanoscale* **6** 8831, 2014. DOI: 10.1039/C4NR01690D

2. J. Li,‡ **K. Otsuka**,‡ X. Zhang, J. Liu, "Selective Synthesis of Large Diameter, Highly Conductive and High Density Single-Walled Carbon Nanotubes by Thiophene-Assisted Chemical Vapor Deposition Method on Transparent Substrates", *Nanoscale* **8**, 14156, 2016. (‡ equal contribution) DOI: 10.1039/C6NR03642B

3. **K. Otsuka**, T. Inoue, Y. Shimomura, S. Chiashi, S. Maruyama, "Field emission and anode etching during formation of length-controlled nanogaps in electrical breakdown of horizontally aligned single-walled carbon nanotubes", *Nanoscale* **8** 16363, 2016. DOI: 10.1039/C6NR05449H

4. **K. Otsuka**, T. Inoue, Y. Shimomura, S. Chiashi, S. Maruyama, "Water-assisted self-sustained burning of metallic single-walled carbon nanotubes for scalable transistor fabrication", *Nano Research* **10**, 3248, 2017. DOI: 10.1007/s12274-017-1648-6

5. **K. Otsuka**, T. Inoue, E. Maeda, R. Kometani, S. Chiashi, S. Maruyama, "On-Chip Sorting of Long Semiconducting Carbon Nanotubes for Multiple Transistors along an Identical Array", *ACS Nano* **11**,11497, 2017. DOI:10.1021/acsnano.7b06282

6. **K. Otsuka**, S. Yamamoto, T. Inoue, B. Koyano, H. Ukai, R. Yoshikawa, R. Xiang, S. Chiashi, S. Maruyama, "Digital isotope coding to trace growth process of individual single-walled carbon nanotubes", *submitted*.

Co-Author Publications

1. G. Németh, D. Datz, H. M. Tóháti, Á. Pekker1, **K. Otsuka**, T. Inoue, S. Maruyama, K. Kamarás, "Nanoscale characterization of individual horizontally aligned single-walled carbon nanotubes", *Physica Status Solidi B*, 1700433, 2017.
2. M. Liu, R. Xiang, Y. Lee, **K. Otsuka**, Y. L. Ho, T. Inoue, S. Chiashi, J. J. Delaunay, S. Maruyama, "Fabrication, Characterization, and High Temperature Surface Enhanced Raman Spectroscopic Performance of SiO_2 Coated Silver Particles", *Nanoscale*, *accepted*, 2018. DOI: 10.1039/C7NR08631H

International Conferences

1. **K. Otsuka**, T. Inoue, S. Chiashi, S. Maruyama, (7P-7-13) "Removal of Metallic Single-Walled Carbon Nanotubes using Molecular Glass Thin Films," 26th International Microprocesses and Nanotechnology Conference, Hokkaido, Japan, November 2013. (Poster)

2. **K. Otsuka**, T. Inoue, S. Chiashi, S. Maruyama, (CT23/S5)"Full-length selective removal of metallic single-walled carbon nanotubes by organic film-assisted electrical breakdown," NT14: Fifteenth International Conference on the Science and Application of Nanotubes, Los Angeles, USA, June 2014. (Oral)

3. **K. Otsuka**, Y. Shimomura, T. Inoue, S. Chiashi, S. Maruyama, (CNTFA P-19) "Full-length re-burning of anode single-walled carbon nanotubes after nanogap formation by electrical breakdown," Third Carbon Nanotube Thin Film Electronics and Applications Satellite, Nagoya, Japan, June 2015. (Poster)

4. **K. Otsuka**, Y. Shimomura, T. Inoue, S. Chiashi, S. Maruyama, (P432) "Electrical burning of metallic single-walled carbon nanotubes in full length assisted by water vapor exposure and polymer film coating," NT15:The Sixteenth International Conference on the Science and Application of Nanotubes, Nagoya, Japan, July 2015. (Poster)

5. **K. Otsuka**, T. Inoue, S. Chiashi, S. Maruyama, (A40) "One-way burning of single-walled carbon nanotubes from site-controlled nanogaps for full-length removal of metallic nanotubes, " NT16: The Seventeenth International Conference on the Science and Application of Nanotubes and Low-Dimensional Materials, Vienna, Austria, August 2016. (Poster)

6. **K. Otsuka**, T. Inoue, S. Chiashi, S. Maruyama, (S3-21) "Voltage-driven physical gap extension of single-walled carbon nanotubes after electrical breakdown," Forth Carbon Nanotube Thin Film Electronics and Applications Satellite, Vienna, Austria, August 2016. (Oral)

7. **K. Otsuka**, T. Inoue, S. Chiashi, S. Maruyama, (A31.00005) “Selective burning of metallic single-walled carbon nanotubes for integration of transistors,” APS March Meeting 2017, New Orleans, USA, March 2017. (Oral)

8. **K. Otsuka**, S. Yamamoto, T. Inoue, R. Xiang, S. Chiashi, S. Maruyama, “Tracing growth process of horizontal arrays of single walled carbon nanotubes by digital isotope coding,” International Winterschool on Electronic Properties of Novel Materials (IWEPNM) 2018, Kirchberg in Tirol, Austria, March 2018. (Accepted)

List of Abbreviations

AFM: atomic force microscopy

CNT: carbon nanotube

CVD: chemical vapor deposition

DPA: dry polymer-assisted

FET: field-effect transistor

IMJ: intramolecular junction

MWNT: multi-walled carbon nanotube

PL: photoluminescence

PMMA: poly(methyl methacrylate)

RBM: radial breathing mode

sccm: standard cubic centimeters per minute

SEM: scanning electron microscopy

STM: scanning tunnel microscopy

SWNT: single-walled carbon nanotube

s-SWNT: semiconducting single-walled carbon nanotubes

m-SWNT: metallic single-walled carbon nanotubes

TEM: transmission electron microscopy

WPA: water- and polymer-assisted